THESIS

PREDICTIVE MODELING AND TESTING OF A DIESEL DERIVED SOLID OXIDE FUEL CELL TAIL GAS SPARK-IGNITION ENGINE

Submitted by

Matthew Countie

Department of Mechanical Engineering

In partial fulfillment of the requirements

For the Degree of Master of Science

Colorado State University

Fort Collins, Colorado

Summer 2020

Master's Committee:

Advisor: Daniel Olsen

Bret Windom
Daniel Baker

ABSTRACT

PREDICTIVE MODELING AND TESTING OF A DIESEL DERIVED SOLID OXIDE FUEL CELL TAIL GAS SPARK-IGNITION ENGINE

Solid oxide fuel cell systems are being developed with total system efficiency targets over 70%. One approach is to provide excess fuel to the solid oxide fuel cell and develop an engine to provide power for mechanical and electrical equipment using exhaust gas from the fuel cell anode (tailgas). This tailgas contains hydrogen, carbon monoxide, methane, water, and carbon dioxide. Compared to natural gas the tailgas fuel has suppressed flame speeds, an extremely small lower heating value, and a low air-fuel ratio due to the precense of large ammounts of oxidation priducts. A predictive model created in GT-Power was used to design an engine that can produce 14kW on tailgas fuel with a brake efficiency η>30%. The model base is an existing Kohler diesel engine. The diesel engine was modeled in GT-Power and validated to within 1% at the anticipated operating point. Using custom combustion models developed from testing several different tailgas blends in a CFR engine, several different engine conversions were modeled to explore different pathways to 30% brake efficiency. Design variations include Miller cycles, turbocharging, compression ratio, and fuel pre-treatment to increase reactivity. Once design parameters were established, an operation envelope was created to identify knock limits and maximum brake efficiency timing. These models helped guide the development of a physical prototype engine that was built and installed at the CSU Powerhouse Energy Campus. The prototype engine ran with simulated anode tailgas up to a maximum power level of 7.42 kW and a maximum brake efficiency of 27.34%, achieveing 53% of the load target, and 91% of the efficiency target. The timings identified by GT-Power to be the point of maximum brake

efficiency and knock initiation were tested at four different speeds on the prototype engine. After data collection, using the experimental power, engine speed, and ignition timing as initial conditions, the model is rerun. The accuracy of the models' prediction capability is tested by using these initial conditions to generate additional model output to compare with measured data. At low speeds and advanced ignition timings, the model matched well, within 10% on almost all metrics, but at retarded timings and high engine speeds, the model began to deviate in most parameters, especially overpredicting exhaust temperature and pressure. The discrepancies between model results and experimental data are discussed in detail. Model and experimental data matched well at advanced timings and low speeds, but deviated signifigantly at retarded timings and high speeds.

ACKNOWLEDGMENTS

I would like to thank Dr. Olsen for giving me the opportunity to work in his research group for the past two years and his support throughout the whole project. The Powerhouse staff Kirk, Mark, and James who gave me the support and tools I needed during commissioning and testing of the prototype engine. Shane Garland for his support over the whole project, developing the fuel supply system and bailing me out whenever the electronics didn't cooperate with me. Isaac Frampton from Kohler Power Systems for his assistance obtaining the data needed for modeling, and for flying out to CSU to assist in the commissioning of the prototype engine. Justin Fulton from Eden Innovations for developing and manufacturing a custom gas mixing system for the engine on very short notice. Alex Balu and Geet Padhi for their work in testing different fuel gas mixtures and developing several different GT-Power combustion models, which my modeling heavily relied on. Finally, my parents John and Tracy for their endless support and encouragement throughout my entire pursuit of mechanical engineering.

TABLE OF CONTENTS

LIST OF TABLES

LIST OF FIGURES

LIST OF ACRONYMS

Fuel Cell Anode Gas	Tailgas
Solid Oxide Fuel Cell	SOFC
Anode Tailgas	ATG
Balance of Plant	BOP
Internal Combustion Engine	ICE
Coefficient of Variation	COV
Brake Specific Fuel Consumption	BSFC
Normal Spark Angle	NSA
Top Dead Center	TDC
Bottom Dead Center	BDC
Intake Valve Closing	IVC
Before Top Dead Center	BTDC
After Top Dead Center	ATDC
Exhaust Valve Opening	EVO
Spark Ignition	SI
Compression-Ignition	CI
Direct Injection	DI

Turbo Energy Limited	TEL
Cooperative Fuels Research	CFR
Three Pressure Analysis	TPA
Ishikawajima-Harima Industries	IHI
Indicated Mean Effective Pressure	IMEP
Pumping Mean Effective Pressure	PMEP
Maximum Brake Torque Timing	MBTT
Maximum Brake Efficiency Timing	MBET
Total Hydrocarbons	THC
Oxides of Nitrogen	NOx
Fourier-Transform Infrared Spectrospecy	FTIR
Brake Specific Emissions	BSE
Brake Specific Carbon Monoxide	BSCO
Pressure Ratio	PR
Manifold Absolute Pressure	MAP
Intake Manifold Temperature	IMT
Exhaust Gas Temperature	EGT
Crank Angle Degrees	CAD

After Bottom Dead Center	ABDC
Before Bottom Dead Center	BBDC
Air Fuel Ratio	AFR

CHAPTER 1: INTRODUCTION AND BACKGROUND

1.1: MOTIVATION AND OVERVIEW

The electrical grid in the United States consists of large centralized power generation stations traditionally running Rankine steam cycles, or more recently combined gas turbine cycles. While convenient for logistics, these centralized locations often require power to be transmitted over long distances, leading to transmission losses. The nature of the Rankine cycle and the large scale of these centralized stations do not respond quickly to changes in demand. To combat this utility companies employ “peaking” stations, typically gas turbine generators. These gas turbines are quick to react but are often much lower in thermal efficiency than a traditional Rankine cycle plant. A modern ultra-supercritical power plant approaches 50% thermal efficiency [1], and a gas turbine generator is around 30%. Distributed generation aims to solve these issues through small scale generation dispersed over a wide geographic area; this allows for real-time reaction to changes in load. Distributed generation also provides more opportunities for the utilization of waste heat. Traditional distributed generation equipment includes renewables such as solar and wind, alongside traditional diesel and natural gas gensets. These gensets can provide power when renewable resources are offline, but the efficiency of these gensets is much lower than conventional power stations, typically in a range between 30% and 45%, with increasing efficiency as rated power increases [2].

To make distributed generation more economically feasible, the thermal efficiency of these gensets must be increased to reduce the cost per kWh of electricity generated. Solid oxide fuel cells (SOFCs) offer an advantage over diesel and natural gas gensets by directly converting the fuel stream to electricity, thereby eliminating most mechanical and combustion losses. A

SOFC takes in a low carbon number hydrocarbon fuel, usually methane, and internally reforms it to hydrogen and carbon, which then can be oxidized by the fuel cell to create electricity. Alone these fuel cells typically have thermal efficiencies around 60% [3]. But these efficiencies are typically on very advanced and thus expensive systems. Due to the nature of the internal reforming, high fuel utilization leads to a buildup of carbon on the fuel cell elements (coke), reducing efficiency. This coke must be cleaned from the elements causing downtime and increased maintenance costs, so SOFCs must be run at lower fuel utilization to reduce this coking problem. This lower utilization leads to hydrogen and carbon monoxide being present in high concentrations in the SOFC anode exhaust stream, incurring a loss on system efficiency. This loss in efficiency is acceptable for many fuel cells because it leads to a decrease in capital costs for the fuel cell elements.

Since this exhaust stream still contains significant amounts of calorific gases, it is possible to use this anode tail-gas (ATG) as a fuel for an internal combustion engine that can recover this energy. Since this fuel consists of both unoxidized fuel (H2, CO, and CH4), alongside a significant amount of oxidation products (H2O and CO2), the ATG is extremely energy dilute limiting engine power. An engine in this configuration would be used to produce electrical power for the SOFC control system and to power the plant mechanical equipment such as the fuel cell pressurizer. The goal of this project is to develop a spark-ignition piston internal combustion engine which can provide 14 kW of power using the ATG fuel. This engine will provide electrical and mechanical power for the SOFC system to raise the balance of plant (BOP) efficiency over 70%. By using a lower utlilization fuel cell in tandem with an engine for high efficiency capital and operating costs can be reduced, leading to an affordable generation system. Many challenges exist with fuel as dilute as ATG; several different fuel streams have

been researched, which offer similar gas compositions to ATG and will provide guidance for the design process. An overview of the proposed system can be seen in Figure 1. To reduce experimental time and costs, a predictive model for this engine was developed in GT-Power using custom combustion models to predict performance and knock limits. This model was used to adapt a commercial diesel engine developed by Kohler Power Systems to spark ignition, and then to explore several different efficiency improvement methods to optimize the prototype for use on ATG fuel. These findings informed the design process of the physical prototype, which was built and delivered to the CSU Engines and Energy Conversion Lab for testing and model verification.

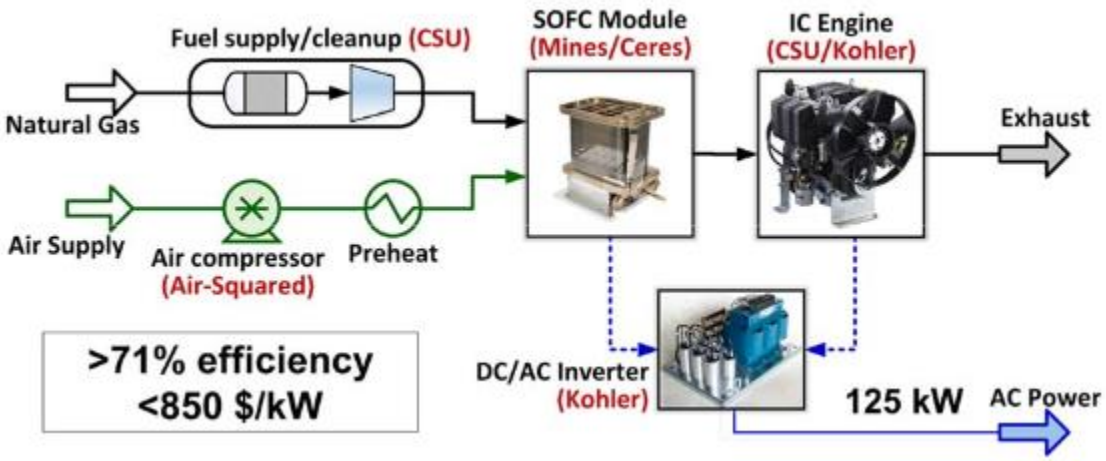

Figure 1. Hybrid SOFC/ICE Schematic [4]

1.2: LITERATURE REVIEW

1.2.1 DILUTE FUELS

Dilute fuels have been in use since the invention of the ICE. During the 19th century, the lack of technology for dispersing and metering liquid fuels forced engineers to use gaseous fuels. During the infancy of the ICE, the most common fuel in use was “producer gas,” a mixture of

flammable and inert gases including carbon monoxide, hydrogen, methane, carbon dioxide, and nitrogen, produced from the gasification of solid fuels through pyrolysis. The exact ratio of these gases varied with the type of gasifier and feedstocks used. However, every process used air as the oxidizer resulting in a fuel highly diluted with nitrogen.

With the invention of the carburetor and the discovery of more energy-dense liquid fuels, producer gas fell out of favor for gasoline. Throughout the 20th-century, research into dilute fuel engines continued, notably directly following WWII in continental Europe, where the lack of oil infrastructure led to the brief rise of cars converted to be powered by producer gas made from the pyrolysis of wood in onboard gasifiers. Similar to these pyrolysis generated fuels are fuels produced via anaerobic digestion of organic matter. The most common production method is from capped landfills. The digestion of waste in the landfill leads to a gas that consists of methane and carbon dioxide, with a small amount of volatile organic compounds[5]. Purpose-built digesters are also available, which can make gas from a wide variety of organic feedstocks. The most popular digester feedstock is sewage, which is digested to make a gas similar to composition to landfill gas but also containing siloxanes, which pose a unique challenge to engine design due to the abrasive nature of silicon combustion products[5].

1.2.2: DILUTE FUEL APPLICATIONS

Dilute fuel engines are in operation across the United States in many applications, the most common one being landfill gas burning gensets. Landfill gas composition varies depending on landfill composition, climate conditions, and landfill stage, a typical composition is a 50/50 mix by volume of carbon dioxide and methane [5]. The addition of carbon dioxide lowers the heating value of the fuel, causing a drop in the rating of the engine due to lower volumetric efficiency because of the carbon dioxide displacing air that could be used for combustion.

Engines in landfill gas service are modified with higher flow rate fuel systems to combat this. In addition to this, many household products that end up in landfills such as soaps and shampoos contain siloxane compounds, which can be present in landfill gas. As these compounds enter the fuel stream and the engine, they combust to produce silica oxide [5]. Silica oxide is extraordinarily abrasive and significantly degrades engine reliability. To combat siloxane contamination, engines in landfill gas service are "hardened" with different exhaust valve and ring materials to better resist wear, alongside an increased maintenance schedule. Engines in landfill gas service are beneficial to the environment by reducing methane emissions from landfills. These methane emissions would otherwise go unutilized and released to the atmosphere. Methane has a global warming potential of 30X that of carbon dioxide [6]. Through the combustion of landfill gas, its overall global warming potential can be lowered by a factor of 26[6] while also producing useful energy.

Digester gas engines are similar to landfill gas engines and share many of the same modifications for service. The gas is produced via the same anaerobic process, so gas content is similar to landfill gas. Depending on the feedstock, digester gas may contain significant amounts of hydrogen sulfide and siloxanes. Hydrogen sulfide reacts with the water in the fuel stream and exhaust to produce sulfuric acid that erodes engine components [7]. Hydrogen sulfide is found mostly in digesters that are using sewage and manures as feedstock. Engines in this kind of service must be maintained often to prevent breakdowns. The energy content of digester gas largely depends on the feedstock used in the digester. High energy feedstocks such as baking wastes, food waste, and grease all generate high-quality gases with few contaminants and high energy content, while sewage and manures produce lower quality gases [8].

Producer gas engines operate on a different type of gas than the anaerobically generated gases before. Producer gas is made through the pyrolysis of organic materials to produce a gas with a high hydrogen and carbon monoxide content, alongside oxidation products such as carbon dioxide and water. Producer gas gasifiers can run on a wide range of feedstocks, which are combustible, but the content of the gas changes with the feedstock. High-quality feedstocks such as wood and charcoal, produce the most energetic gases. While low-quality feedstocks such as grasses produce low energy gases[9], also the feedstocks for producer gas gasifiers must be pre-processed by drying the feedstock to remove water, which would otherwise dilute the fuel stream. Depending on the feedstock producer gas can contain large amounts of dust, tar, and acids, which significantly degrades engine reliability. Thus necessitating fuel pre-treatments to remove these contaminants [9]. Producer gas engines are typically converted spark ignition running on pure wood gas, or low compression diesel engines running in a dual fuel configuration. Because producer gas is partially combusted with atmospheric air to produce the gas, it contains a lower energy content than landfill gas or digester gas due to nitrogen and combustion products. An engine running on producer gas is typically derated by 30% of its rated power output. Using forced induction can mitigate this effect to an extent. Engines in producer gas service generally are found in developing countries where hydrocarbon fuel supplies may be unreliable. This flexibility makes the duel fuel option very popular because it allows for the use of diesel fuel at full rated load if needed, and operation on producer gas when fuel is not available [9].

1.2.3 FUEL COMPOSITION EFFECTS ON COMBUSTION

Since dilute fuels come from a variety of feedstocks, the composition of the fuel can vary. This composition variation can have a detrimental effect on engine performance and knock

characteristics, which is especially of concern to commercial engine manufacturers. Gupta et al., 2019 [10] explored the impact that varying composition of biogas can have on performance and knock. In this work, the Wobbe index of the fuel was varied. Wobbe index is a parameter that quantifies the fuels' energy flow rate through a fixed orifice under given inlet conditions and is defined as the ratio of the fuels' lower heating value to the square root of its specific gravity[10].

$$WI = LHV * \left(\frac{\rho_{air}}{\rho_{gas}}\right)^{0.5} \quad (1)$$

Methane and Carbon Dioxide are blended by volume and injected into the intake manifold of a TV1 Kirloskar engine operating at 1500 RPM. The volume percentage of CO2 is varied from 0% to 50%. Some of the results are shown in Figure 2. Figure 2 shows that with increasing CO2 percentage, the coefficient of variation (COV) of IMEP increased at low engine loads due to the lower flame speeds of high CO2% mixtures. By increasing CO2 percentage, the maximum knock limited load was also raised due to the increasing methane number of the fuel as CO2 percentage increased [10].

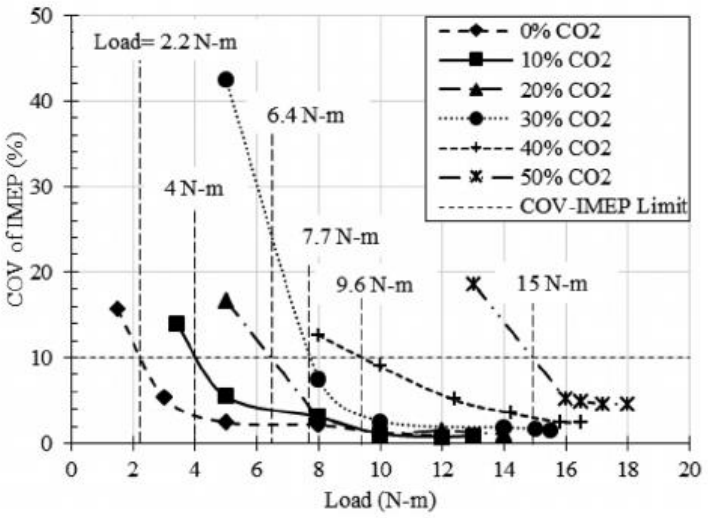

Figure 2: COV of IMEP vs. Load for Varying Gas Mixtures [10]

The effect on brake efficiency at load was also explored in this study (Figure 3). For a given load that increasing CO2 percentage decreased brake efficiency. Even though pumping losses decrease with increasing CO2 percentage due to the throttle having to be open more, the degradation in the combustion process is dominant over this effect. For all mixtures, brake efficiency increased with increasing load due to increasing combustion rate and stability and lower pumping losses.

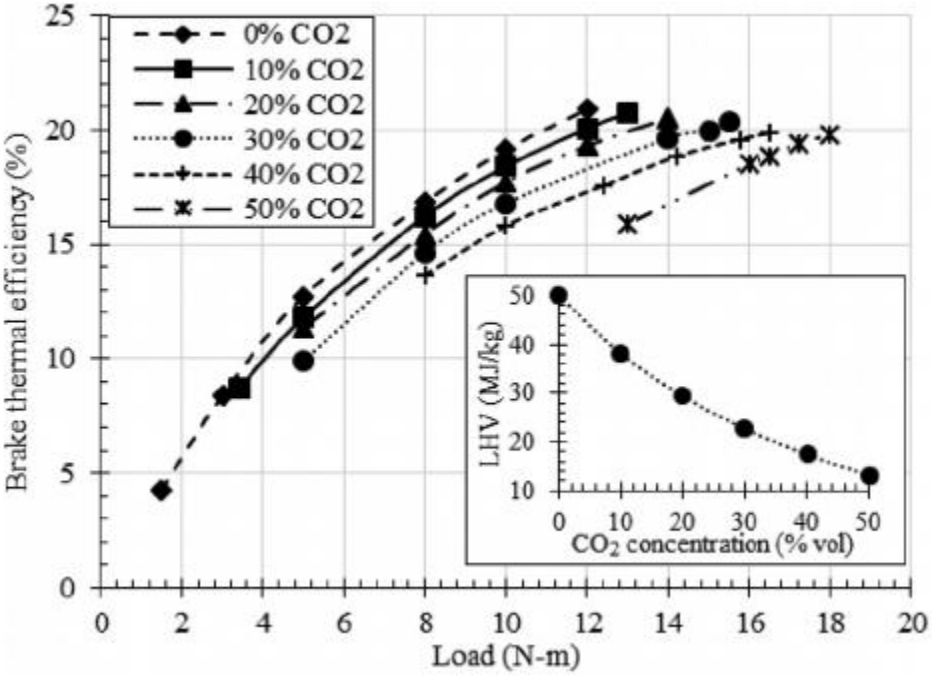

Figure 3: Brake Efficiency vs. Load for Varying Gas Compositions [10]

A study performed by Papagiannakis et al., 2013 [11] modeled the effect of spark timing and compression ratio on a wood gas-fueled spark-ignition engine. The main components of the fuel being tested were hydrogen (~20%), carbon monoxide (~20%), methane (~0.5%), with the balance made up of carbon dioxide and nitrogen. A combustion model was produced, which used a two-zone method to determine combustion characteristics. This model was verified against

experimental data obtained from a J320GS engine fueled by a wood gasifier running in a lean-burn configuration. [11] This model found that an increase in the compression ratio increased the burn rate of the fuel. Leading an increase in the compression temperatures, which improves the combustion quality during the initial stages [11]. The effect of the compression ratio was examined on brake specific fuel consumption (BSFC). As seen in Figure 4, increasing the compression ratio was found to reduce the BSFC of the engine. This effect was observed both at full and part load conditions. BSFC was reduced at full load conditions due to the increase in combustion temperatures and due to the reduction of pumping losses.

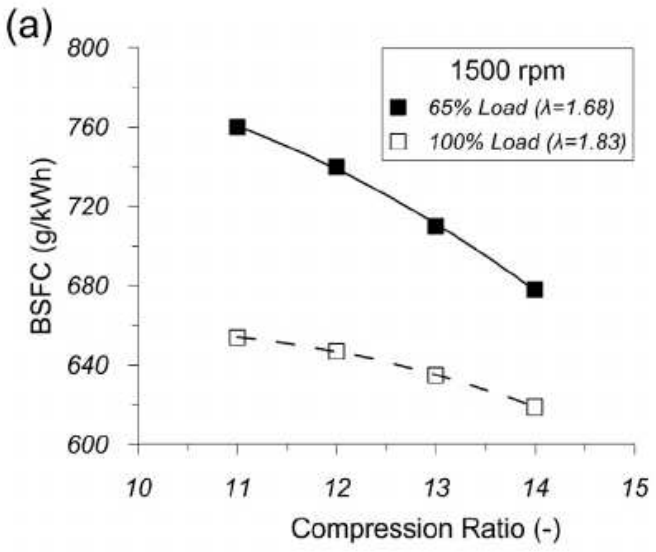

Figure 4: Calculated BSFC at 65% and 100% load and 1500 RPM [11]

Spark timing was also examined by advancing the spark timing from the normal spark angle (NSA). Advancing the spark angle from the NSA resulted in BSFC reduction in the full load case, but an increase in BSFC in the part-load case [11]. This trend was especially prominent in the 13:1 CR cases. At 100% load, the spark advance while improving BSFC as a trend did little to improve the overall BSFC, and at 65% load, the BSFC change was more prominent (Figure 5).

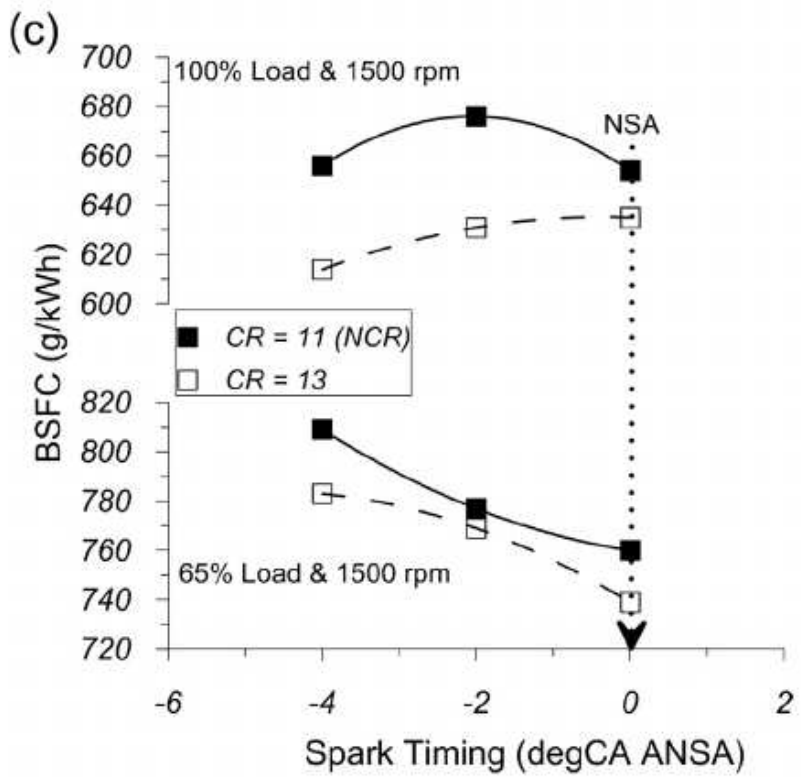

Figure5. Effect of Spark Advance on BSFC for different CR and Loads [11]

1.2.4: BRAKE EFFICIENCY IMPROVEMENT METHODS

Maximizing the brake thermal efficiency of the developed ATG engine is the primary goal of this project. To achieve BOP efficiency >70% the developed engine must have a brake efficiency of >30%. There are several different ways to improve the brake efficiency of an ICE. Traditionally the most effective method has been through increasing the compression ratio; it can also be done through advancing the ignition timing, providing the engine with forced induction, or converting the engine to an over-expanded or "Miller" cycle.

The principle limit to how far these methods can be applied is detonation. Knock is the uncontrolled combustion of the in-cylinder charge, which has not already been consumed by the normal flame front. Knock occurs due to the compression of the end gas due to the expansion of

the burned gases. If this compression raises the pressure and temperature of the end gas rapidly enough, then knock will occur [12]. Knock is extremely harmful due to the rapid rise in in-cylinder pressure from uncontrolled combustion. This rapid rise causes pressure waves to travel through the charge within the cylinder, which leads to the characteristic “knock” or “ping” noise while detonation is occurring. These pressure waves disturb the cool boundary layer gas near the cylinder walls and piston. Which, in many cases, leads to overheating and eventually failure [13]. As such, it is necessary to limit the end gas pressure and temperature below the level where knock will occur. The main parameter which dictates in-cylinder pressures is the compression ratio, which is defined as the ratio of the starting volume of the cylinder V1 over the clearance volume V2 [14]. During the compression stroke, cylinder pressure rises approximately according to isentropic compression shown in Equation 2, where P1 is the cylinder pressure at intake valve closing (IVC), and k is the ratio of specific heats of the working fluid.

$$r = \frac{V_1}{V_2} \qquad (2)$$

$$P_2 = P_1 r^k \qquad (3)$$

Since r is an exponential term, final compression pressures mostly depend on the r term. But P1 also affects final compression pressures by raising the starting pressure; as is the case during forced induction operations such as turbocharging and is why many turbocharged engines have reduced compression ratios compared to their naturally aspirated counterparts [12].

For an ideal Otto cycle as the compression ratio increases, the brake efficiency of the cycle increases according to Equation 4. This relationship can be seen in Figure 6, where brake efficiency increases with increasing compression ratio. As such, it is necessary to select the highest compression ratio possible for an engine without being limited by detonation. In a real

engine, this may not always be the case due to effects not captured in the ideal Otto cycle. These effects include irreversible losses from compression, heat transfer occurring during compression, and quenching losses during combustion due to the increased surface to volume ratio that comes with having a lower clearance volume.

$$\eta = 1 - \left(\frac{1}{r}\right)^{k-1} \qquad (4)$$

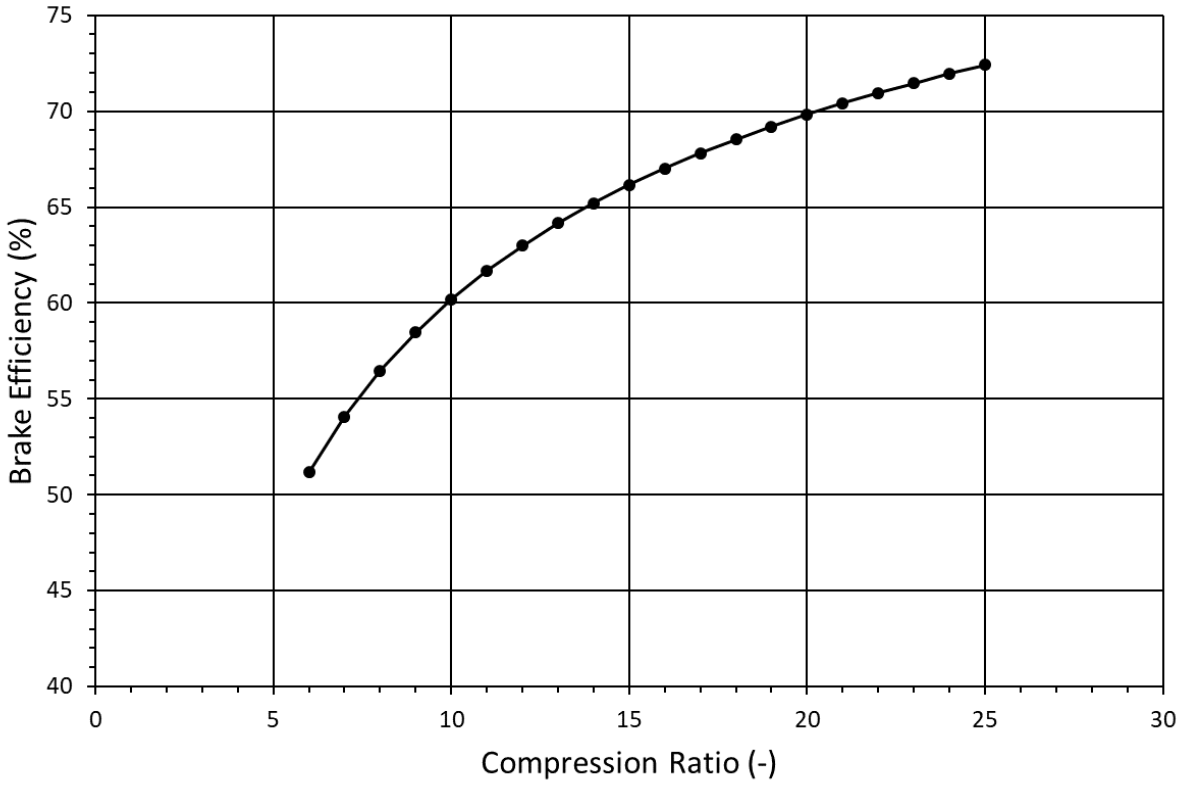

Figure 6: Ideal Otto cycle brake efficiency as a function of compression ratio

Turbocharging is another common method of increasing engine efficiency and power output. An exhaust gas turbine drives a compressor increasing air-flow rate through the engine, allowing more fuel to be burned for a given displacement [12]. This turbine recovers waste exhaust energy, which would otherwise go out of the tailpipe. The resulting increase in power

density elevates engine efficiency. Proper sizing of a turbocharger to the application is imperative for maximum efficiency. Too large or small of a turbocharger will result in the turbomachinery operating in an inefficient zone of the map, increasing losses. If sized to small, the turbocharger becomes a bottleneck for flow, dramatically increasing exhaust backpressure. Turbochargers can significantly increase the risk of knock occurring due to increasing the P1 term in Equation 2, resulting in higher peak compression pressures. Compressor heating also occurs while using a turbocharger; which without the use of an external heat exchanger between the compressor and intake also known as an "intercooler," can result in elevated charge air temperatures that significantly increases the likelihood of knock, and reduces charge density, lowering maximum efficiency [12].

Ignition timing is an essential variable for the efficient operation of an ICE. The ignition timing is defined as the degrees before top dead center (°BTDC) that the spark plug is fired, and combustion is started [12]. This timing determines where maximum cylinder pressure occurs in the cycle. Optimally the spark is fired so that peak pressure occurs at approximately 18° after top dead center (ATDC). This location allows for the high pressure to do maximum work on the crankshaft. If the spark is fired too early, detonation can occur due to peak pressure occurring earlier in the cycle; possibly even before the piston has reached TDC. Delayed ignition timing is also detrimental to the efficiency of an engine. If ignition happens too late in the cycle and peak pressure occurs after 18°ATDC, then the maximum work may not be extracted from the charge. Combustion is still occurring as the piston is expanding, increasing the heat transfer losses to the cylinder walls and reducing post-combustion piston expansion. If ignition timing is sufficiently delayed, then the charge may still be burning at the time of exhaust valve opening (EVO).

Causing drastically increased exhaust valve temperatures and lead to burning the valve itself, resulting in a loss of compression and, eventually, engine failure [12].

The last major method to adjust engine efficiency is to change the cam timing so that that the signifigant valve events occur at different times in the cycle. By changing where these events happen, the effective compression ratio of the engine can be changed. By delaying IVC then inducted charge is pushed back into the intake manifold, reducing the volume enclosed at IVC and thus the compression ratio. By advancing IVC, less charge is inducted into the cylinder, creating a vacuum through the rest of the intake stroke, allowing the expansion stroke to still retain the full expansion as mechanically set by the stroke, creating an "over-expanded" cycle [12]. Theoretically, more work can be extracted from the Miller cycle due to this over-expansion of the charge. These techniques can lead to increased pumping losses, though due to the inducted charge being pushed back into the intake manifold or irreversible losses from the expansion and contraction of the charge under vacuum. The Miller cycle is defined by the ratio of the expansion ratio to the compression ratio. When this quantity λ is greater than one, the cycle is defined as a Miller cycle. The ideal Miller cycle efficiency is defined according to Equations 5 and 6 [13], where P_{IVC} & V_{IVC} are the pressure and volume at IVC, respectively, and Qin is the heat addition per cycle.

$$\lambda = \frac{r_e}{r_c} \qquad (5)$$

$$\eta = 1 - (\lambda r)^{1-k} - \frac{\lambda^{1-k} - \lambda(1-k) - k}{(k-1)} * \frac{P_{IVC} V_{IVC}}{Q_{in}} \qquad (6)$$

In addition to increased pumping losses, the Miller cycle also lowers the power density of the engine. Due to less charge mass in the cylinder at IVC and thus less mass flow through the

engine. This drop-in power density is counteracted through the use of turbocharging to increase the cylinder pressure at IVC [13].

Engine operation factors also impact engine efficiency. Speed and load are the two factors that affect the efficiency the most. These two factors affect the interaction of friction and heat loss, which directly impact engine efficiency. By increasing engine speed, the frictional losses in the engine increase due to bearings, valvetrain, oil pumping, and other losses. But conversely, as engine speed increases, heat transfer losses decrease. This effect is due to the charge being exposed to the cylinder for a shorter amount of time, less heat is transferred to the coolant early in the combustion process, and more work can be extracted for the charge [13]. Load affects efficiency in much the same way for SI engines as the load increases the throttle opens, which decreases pumping losses [12]. But as the load increases, maximum cylinder pressure increases, which increases the load on the main bearings and increases frictional losses. In compression ignition (CI) engines with no throttle, increasing load only increases frictional losses due to pumping losses being constant for a given engine speed [12].

1.3 SPECIFIC AIMS OF RESEARCH

The overall aim of this research is to develop a low cost, high-efficiency SOFC with a system efficiency exceeding 70%. Recovery of fuel-cell waste exhaust energy is needed to reach this efficiency target. An internal combustion engine was developed, which has a brake efficiency greater than 30% while producing 14kW. As part of this study, a variety of efficiency improvement methods are investigated. To facilitate development time and reduce the cost, a predictive model will be built in GT-Power. This model will be based on an existing diesel engine and will be verified against performance data to provide an accurate base for the predictive model. Several efficiency improvement methods will be investigated with the

predictive model to guide physical prototype development. A physical prototype will be developed in partnership with Kohler Power Systems, and delivered to the CSU powerhouse for physical testing, and experimental verification of the GT-Power predictive model.

CHAPTER 2: GT-POWER MODELING

2.1: GT-POWER MODELING SOFTWARE

The modeling for this project uses the engine simulation software GT-Power, which is a subprogram of the commercial thermal systems simulation tool GT-Suite. GT-Power simulations use a one-dimensional solution of the unsteady Navier-Stokes equations for continuity, energy, and momentum. The system is broken up into control volumes, and the variables are solved for each boundary. For engine simulations where crank resolved solutions and wave dynamics are important, an explicit method of time integration is used in the Navier-Stokes equation.

A graphical interface is used to construct an engine model in GT-Power by placing blocks which represent engine components such as cylinders, valves, turbocharger, crank-train, pipes, etc. The user outlines conditions that are to be tested through manipulation of the parameters of these blocks. After running the simulation, a tool called GT-Post is used to output performance characteristics such as brake power, brake efficiency, cylinder pressure, heat release, and turbocharger performance. An example of this block type model is shown below in Figure 7.

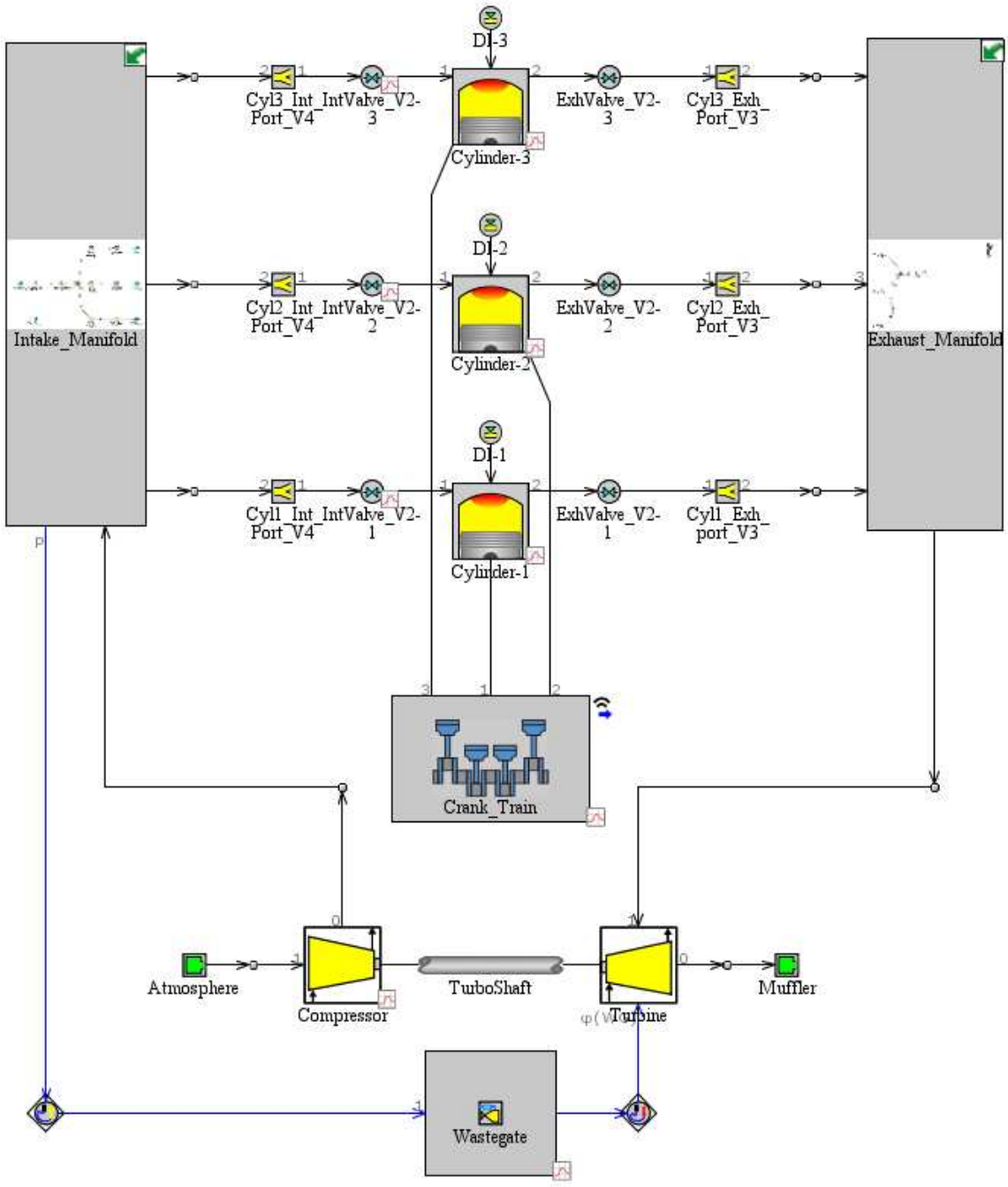

Figure 7: GT-Power Flow map

2.1.1: DATA NEEDED TO BUILD AN ENGINE MODEL

Detailed geometric and operating engine data must be obtained for the engine to build an accurate engine model, including:

- Crank-train Geometry: bore, stroke, TDC clearance, compression ratio, connecting rod length, firing order, piston bowl geometry, piston area, rod bearing geometry, and 2 or 4 stroke
- Block Geometry: number of cylinders, inline or vee configuration, main bearing geometry, and water jacket geometry
- Head Geometry: combustion chamber geometry, valve locations, head area, injector location (DI), spark plug location (SI), intake, and exhaust port geometry
- Intake and Exhaust Valves: valve diameter, valve type (Na filled or solid), valve lift vs. cam angle, flow coefficients vs. lift, swirl coefficients vs. lift, tumble coefficients vs. lift, valve lash, follower type, OHV SOHC or DOHC configuration, and cam bearing geometry
- Fuel Injector Data (DI Only): injection start, injection duration, and injected mass per cycle
- Intake and Exhaust Geometry: geometry of all components including manifolds, pipes, muffler, etc. This data can be provided in the form of 3D models and converted for use in GT-Power with provided tools
- Turbocharger Data: compressor diameter, turbine diameter, wastegate diameter compressor map, and turbine map

- Performance Data: torque vs. RPM, BSFC vs. RPM, boost pressure vs. RPM, exhaust pressure upstream of turbocharger vs. RPM, cylinder pressure traces, and heat release vs. crank angle
- Operating Conditions: **a**mbient conditions during performance data testing, oil temperature, oil viscosity, and thermostat temperature

2.1.2: GT-POWER COMBUSTION MODELING

Accurate combustion modeling is an essential part of creating an accurate engine system model. The combustion model must accurately recreate in-cylinder conditions such as pressure rise, maximum pressure, and heat release. For both compression ignition (CI) and spark ignition (SI), GT-Power divides the combustion chamber into a burned and unburned zone. During calculations, GT-Power transfers mixture from the unburned to the burned zone. The rate of this transfer is dependent on the burn rate.

GT-Power has multiple ways of calculating this burn rate. If in-cylinder data such as pressure traces and heat release rates are available, a non-predictive model can be used. This model imposes a burn rate that is calculated from a Wiebe function, which is itself calculated from in-cylinder pressure data. The Wiebe function produced for the diesel engine model is presented in Figure 8.

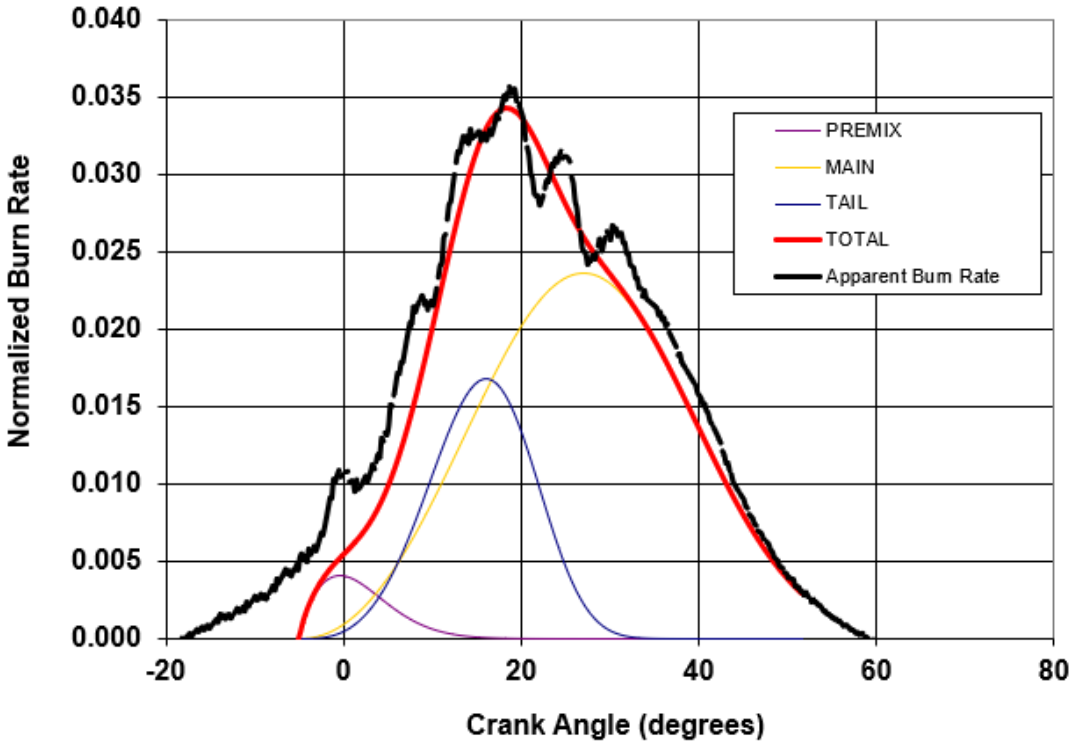

Figure 8: Finalized Wiebe Function for the CI Model. The black line is the Kohler data, and the red line is the GT-Power total burn rate

A Wiebe function was utilized for the initial diesel engine modeling as it is the simplest to employ and most accurate if quality data is provided. If no data is available, then a predictive combustion model can be utilized. This model predicts a burn rate based upon in-cylinder conditions such as wall temperature, pressure, equivalence ratio, and chemical composition of the fuel. This method is to be employed when no direct data is available, and the study being performed influences the burn rate in the cylinder (e.g., spark timing, compression ratio, IVC, etc.). Since the ATG fuel model meets these criteria a predictive model EngCylCombSITurb is employed in the modeling of the ATG fuel. The predictive combustion model relies on chemical kinetics to track normal combustion reactions and knock pre-cursor reactions. GT-Power accepts a Chemkin chemical mechanism file that can track a different number of species, reactions, and

reaction rates. In Geet Padhi's work, *Modelling and Simulation of Combustion of Dilute Syngas Fuels in a CFR Engine* [15], three different chemical mechanisms were identified. They were the San Diego, GRI, and Galway Syngas mechanisms.

Extensive modeling was done in Padhi's work to compare known knocking cases in the CFR engine to these mechanisms to determine which one could most accurately predict knock, nnd normal combustion efficiency. The Galway syngas mechanism was the most accurate in predicting knock, though this mechanism has a shortcoming of not having methane reactions. Due to methane making up such a small percentage of the fuel mass, these reactions are most likely not important to knock. Hydrogen was added to the model fuel at an equal amount of energy to preserve performance prediction. Since hydrogen is much less knock resistant than methane, knock predictions are more conservative than with the methane added.

2.2: INITIAL DIESEL ENGINE MODELING

The modeling process began with the construction of the base diesel engine model. This engine is the commercially available Kohler KDW993T, a three-cylinder inline, indirect injection diesel engine, initially offered in the Polaris MRZR. The characteristics of the 993T are outlined in Table 1 and Figure 9. This diesel model was tuned using data provided by Kohler for power, torque, and BSFC over a range of speeds with the engine in a configuration, including the alternator, fan, and a full exhaust. A view of the unmodified engine is provided in Figure 10.

Table 1. KDW993T Engine Characteristics

Displacement	0.993L
Configuration	Inline 3 Cylinder
Compression Ratio	21:1
Injection	Unit pump injector with swirl pre-chamber
Forced Induction	Turbocharger with internal wastegate
Power	41.9 kW at 4500 RPM
Torque	96.5 N*m at 3800 RPM
Minimum BSFC	238.6 g/kWh at 2600 RPM
Maximum Speed	4600 RPM

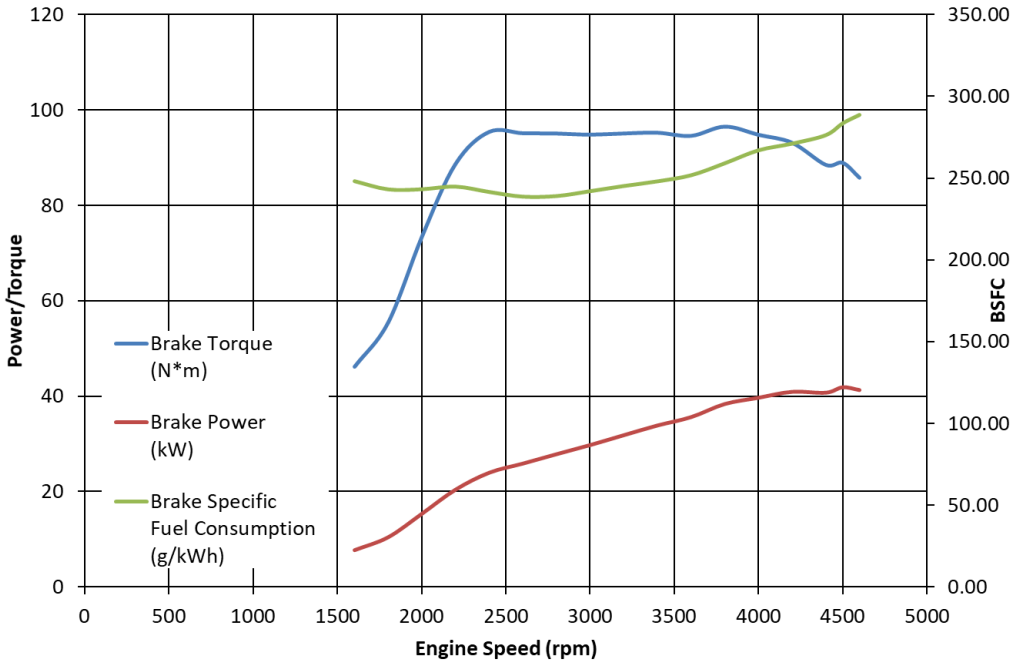

Figure 9: KDW993T Performance Curves

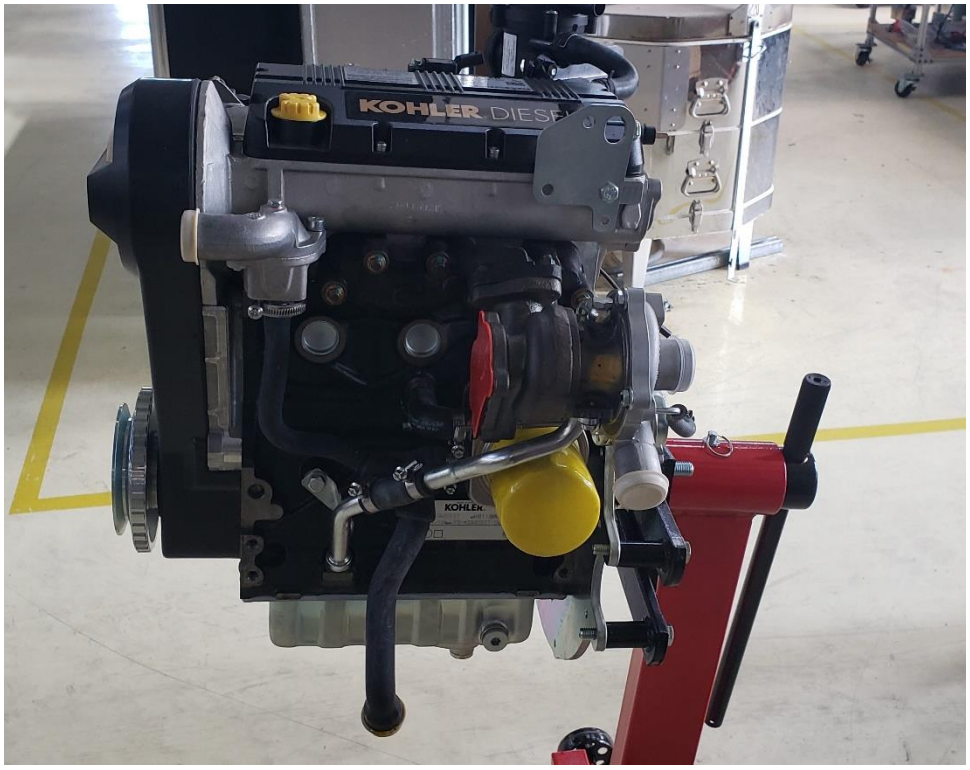

Figure 10. Unmodified KDW993T

The KDW993T was chosen because it offers a robust starting point for a spark ignition engine. The Kohler team in Italy provided in-cylinder pressure data for the 993T, presented in Figure 11. From Figure 11, it is seen that combustion peak pressures have a magnitude of 120 Bar. These combustion pressures are much higher than typical SI engine pressures and will allow the engine to withstand more aggressive combustion settings and potential knock encounters during experimental testing. The 993Ts also offers a mechanically robust starting point. The engine comes with oil-cooled piston, which will reduce the likelihood of piston failure due to knock events. A high rated speed ensures high bearing life at the low engine speeds planned for the prototype, and a skirted block strengthens block rigidity and improves engine life.

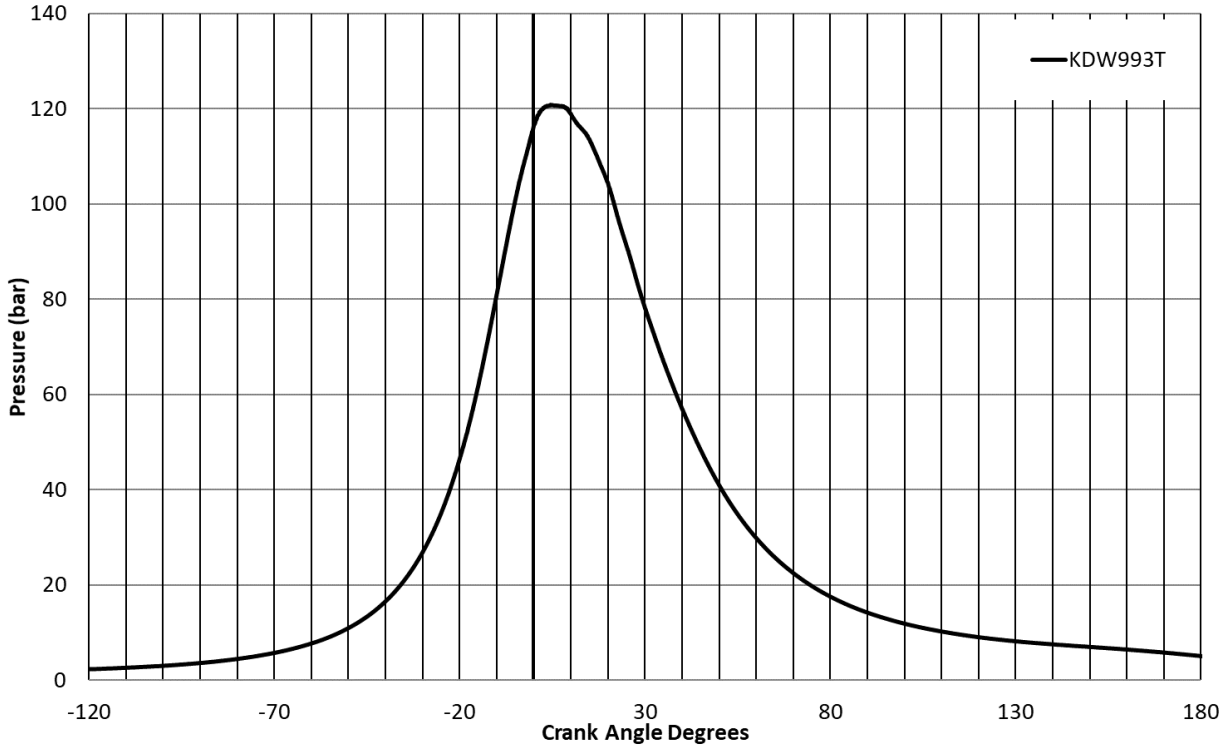

Figure 11: KDW993T Pressure Trace at 2600 RPM

2.2.1: DATA PROCESSING

To be used in GT-Power, this data must be processed into a form that GT-Power can use. The data given by Kohler not only contained performance metrics, but 3D models of all parts relevant to the gas flow, including the intake manifold, cylinder head, piston, and exhaust manifold. These parts must be converted into a 1D form that GT-Power can use. To do this, GT-Power includes a tool called GEM3D. GEM3D works by letting the user edit 3D models down to interior flow paths. These paths are discretized into sections based on basic elements such as pipes, cones, and curves. These elements are converted into the GT-Power equivalent represented in 3D space, so the user can check their work to ensure that the new GT-Power model is an accurate representation of the original. Using this method GT-Power parts were created for the intake and exhaust manifold, as well as the intake and exhaust ports.

Alongside these 3D models, data was provided for the flow characteristics for the head and valves. This data was collected on a flow bench to quantify the flow, swirl, and tumble coefficients for the valves. Since this data was taken with the intake and exhaust ports attached to their respective valves, it also encompasses the losses within the ports. To avoid doubling the pressure and friction losses within the ports, the GT-Power calculated losses are set to zero, and all losses are achieved at the valves. The cam profile was provided by Kohler and uploaded into the GT-Power model; the stock valve profiles are presented in Figure 12. These profiles will be manipulated later on during efficiency optimization.

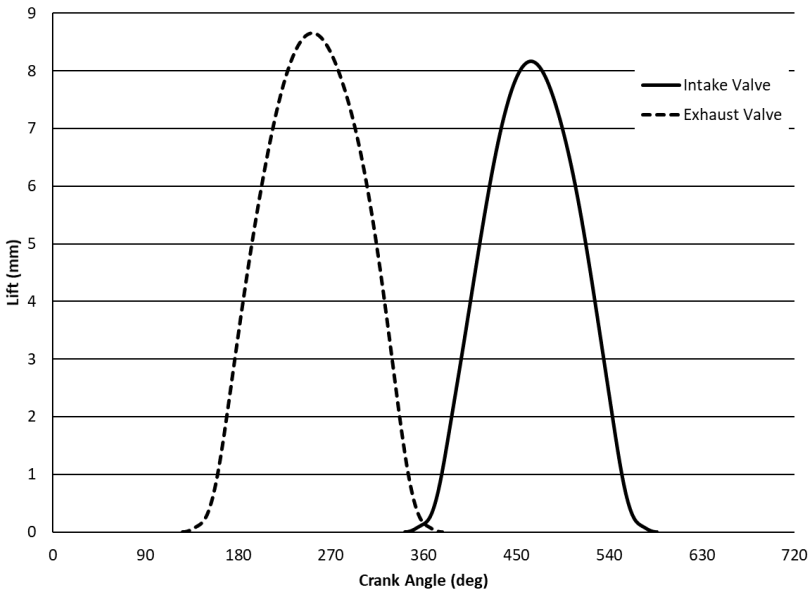

Figure 12: KDW993T Stock Valve Profiles

2.2.2: UNDERLAYING MODEL CONSTRUCTION

To predict performance under different engine speeds an effort must be made to build accurate underlying models for the engine system model. The most critical of these models being the frictional and heat transfer loss models. Templates are provided in GT-Power for different levels of available information ranging from direct measured losses to predictive models. Since

frictional and heat transfer losses are highly dependent on load conditions for the engine to predict these losses under different combustion conditions, predictive models are used for both the heat transfer and frictional losses.

The frictional loss model is a template provided within GT-Power, which is based on work by Sandoval and Heywood [16]. This model uses the engine bearing geometry, cam follower type, oil viscosity, and temperature to predict frictional losses within the engine. These losses are separated into rotating, reciprocating, and accessories losses, which will be of use during simulations to simulate friction-reducing coatings on the pistons. Since frictional losses change dramatically with different in-cylinder pressures, it was crucial to get this part correct to ensure accurate results of the simulations. An error in the frictional modeling could have drastic effects on the prediction of the brake efficiency, especially at higher speeds where friction represents a higher proportion of losses.

The overall heat transfer model is split into multiple components. For general parts outside of the block such as the intake and exhaust manifolds, piping, a general loss model is used based upon the parts' surface area, material, temperature of the surroundings, and temperature of the gas flowing through the part, allowing for the convection losses to be calculated. Each part is coupled to the part adjacent to it to calculate the conduction losses. Exhaust parts have an emissivity input to calculate radiation losses, to reduce computation times an assumption that radiation losses from the intake manifold parts to the surroundings were negligible is made. Parts within the block, such as the in-cylinder heat transfer and head heat transfer, are incorporated into a predictive model provided by GT-Power. This predictive model is the improved Woschni model [17]. The in-cylinder heat transfer model is the most crucial of the models because it determines how much heat of combustion is rejected to the coolant and

exhaust, which affects the overall thermal efficiency. To ensure this model is as accurate as possible, Kohler provided a KDW1003 engine, a non-turbocharged version of the 993T that shares the same block and head design. This engine was disassembled at CSU to take direct measurement of the water jacket and head coolant passages. These measurements were used to specify the heat transfer boundary conditions.

The combustion object for the diesel model is a Wiebe function and is non-predictive to Validate the heat transfer and friction models. To help generate this Wiebe function, Kohler provided traces of the in-cylinder pressure and heat release. Using an excel program included in GT-Suite the Wiebe heat release is overlaid onto the normalized burn rate, the Wiebe parameters are then adjusted to get a fit that closely matches the experimental data. With the Wiebe function in place, the engine is then verified to match the experimental data; this is first done without the turbocharger model to remove variability introduced by a modeled turbo and instead uses end-environments to provide specified intake and exhaust pressures. These pressures are from data provided by Kohler taken just downstream of the compressor and upstream of the turbine.

Validation was performed at an engine speed of 2600 RPM at full load, critical engine metrics (Power, BSFC, η, and Cylinder Pmax) were to be matched within 1% of experimental data. A speed of 2600 RPM was chosen as the validation speed because that is where the engine will most likely operate during the gasification phase, and a mid-range RPM will provide a window on either side of the validation speed where the model will be most accurate. To adjust the critical metrics to match the experimental data a sweep of intake and exhaust friction multipliers was used to fine-tune the aspiration efficiency of the engine. Care was taken to ensure these multipliers do not exceed +-10% of the default. The point of this adjustment is to account for friction in the flow which may of been lost due to simplification when converting intake and

exhaust parts to 1D. In-cylinder pressure and torque output were adjusted by sweeping injection timing and duration. Once these parameters are validated at the operating point, a simulated power run was performed from 1600 to 4600 RPM at full load to compare the critical metrics over the whole operating range of the 993T and ensure no parameters diverged. The single point verification is seen in Table 2.

Table 2: GT-Power Model Final Verification

Parameter	Kohler Data	GT-Power Model	Percent Difference
Engine Speed (RPM)	2600	2600	0.00
Torque (N*m)	95.10	95.69	0.62
Power (kW)	25.89	26.05	0.62
BSFC (g/kWh)	238.63	237.17	0.61
Brake Efficiency (%)	35.41	35.30	0.32
Maximum Cylinder Pressure (Bar)	120.84	120.67	0.14

Once satisfactory comparisons of these metrics were achieved, the turbocharger model was integrated into the diesel model. The 993T turbo has a wastegate, so a PID controller was added to the model to control wastegate diameter to target boost pressure for a given engine speed. The compressor, and turbines models were built using maps provided by Turbo Energy Limited (TEL), the OEM manufacturer of the turbocharger. The model was then simulated from 1600 to 4600 RPM while sweeping the turbine efficiency multiplier to match turbine inlet pressure to the data provided by Kohler while maintaining the critical engine metrics matches through fine-tuning of the earlier parameters. Care was taken not to adjust this parameter more than +-5%, or else the turbine performance would not be reflective of actual performance. The whole system was then swept from 1600 to 4600 RPM for final validation. The results of this sweep can be seen below in Figure 13. The engine model performed well for low and Mid-range speeds where the gasified engine is anticipated to operate, at high engine speeds n>3600 RPM

the GT-Power model starts to over predict the power output. This over-prediction could not be addressed without sacrificing accuracy at low engine speeds.

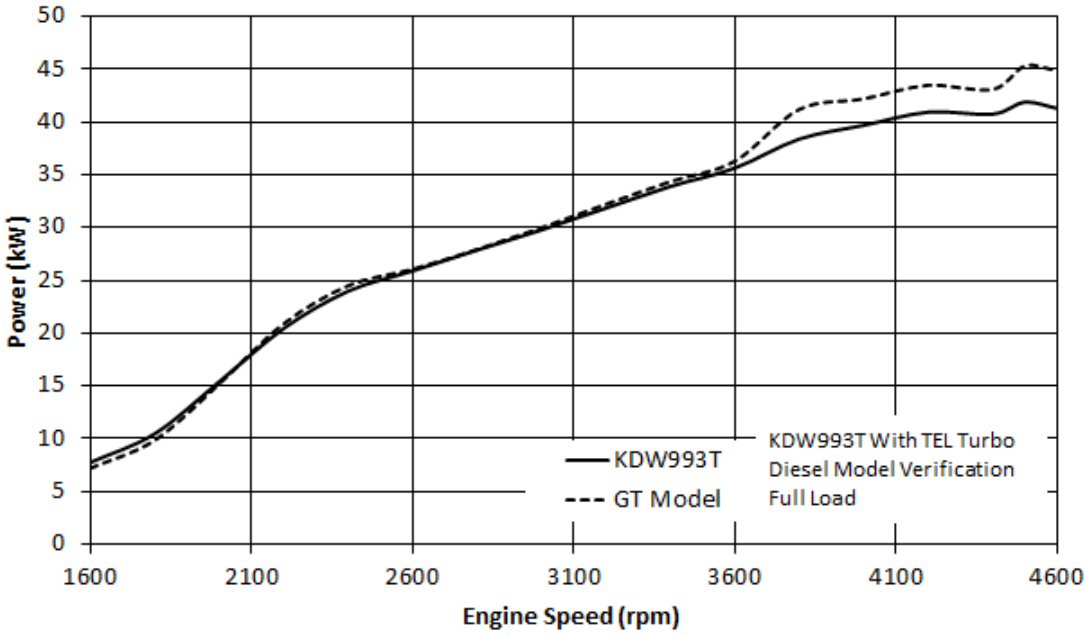

Figure 13: Brake power of the final validated diesel model including turbocharger model

After consultation with Kohler, it was decided that high-speed operation was not desirable for this application due to the decreased bearing life at high speeds, so the emphasis was placed on the low-speed accuracy of the model, and this deviation at high speed was deemed acceptable.

Peak cylinder pressures were also checked against data provided by Kohler at the CI configurations' most efficient operating speed of 2600 rpm. These results can are seen in Figure 14. Combustion modeling was not as crucial for the diesel model. Still, peak pressures are influenced by the heat transfer modeling and provide a good indication on whether the heat transfer modeling is correct. It can be seen in Figure 14 that the GT-Power model follows the relative magnitude of the pressure well, but the phasing is advanced somewhat. This could be

due to the heat transfer modeling being too aggressive. Since heat transfer losses would be higher in the modeling than in the actual engine it was deemed acceptable since the brake efficiency would be under-predicted by the model.

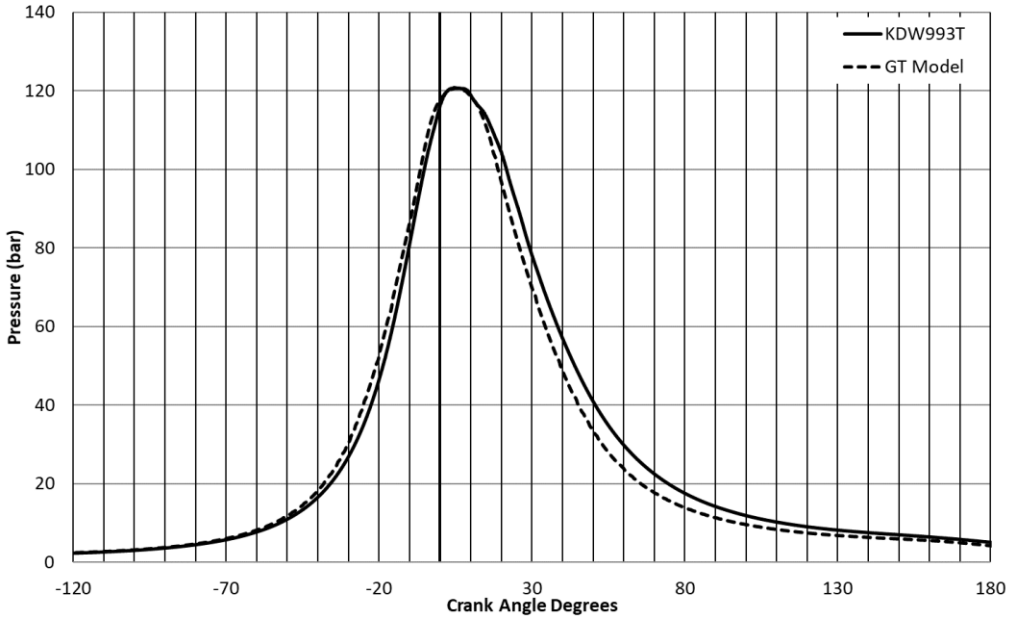

Figure 14: Diesel Model Pressure Trace Comparison

The peak pressures were also checked at every speed across the anticipated operating range in Figure 15. These pressures line up well through the mid-range but started to deviate at higher engine speeds, much like the engine power. Since high-speed operation is not anticipated, this deviation was deemed acceptable. Pressure data was not available for slower engine speeds.

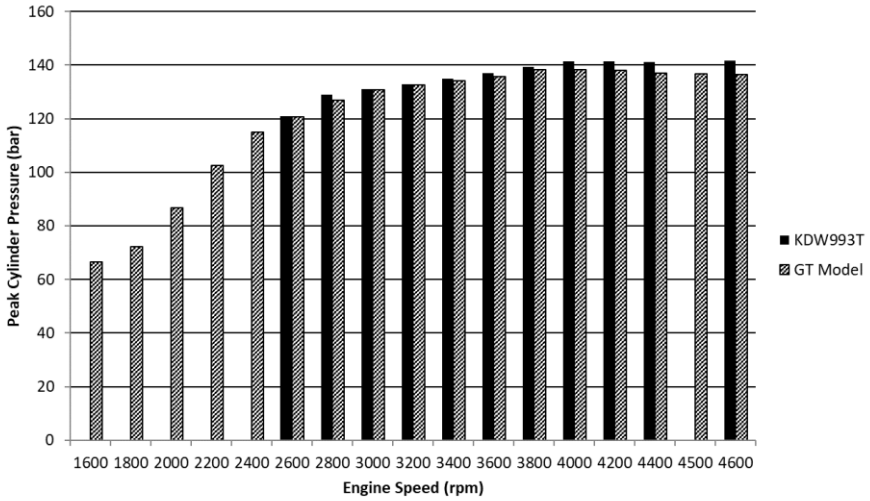

Figure 15: Peak Pressure Comparison Across Operating Range

2.3: GASIFICATION PROCESS

After the diesel engine model validation, the next step was to model the gasified engine in a configuration for use with natural gas. This process started by removing the diesel injection system and replacing it with port fuel injection system using natural gas. Second, the diesel Weibe combustion model was replaced with a SI Wiebe function. This function was generated through earlier modeling and validation of a Kohler CH1000 engine; this function was integrated with the standard GT-Power knock model for natural gas based on methane number of the fuel. To better define engine operation, the turbocharger was removed from the system model and replaced with a "simulated" turbocharger, which provides specified intake pressure and temperature to the intake manifold.

The natural gas model was used as the basis of the ATG conversion, to achieve this natural gas was swapped for ATG. To improve combustion quality and increase fuel energy density two fuel pretreatments were identified. These consist of condensing the water out of the raw ATG at different dewpoints, one at 40°C and one at 90°C. The composition and energy

densities of these fuels can be seen in Table 3. Two different ATG models were developed one for each of the treated fuel blends. The focus of modeling efforts and engine development will be on the 40°C fuel based upon recent research by Alex Balu. Due to the increase in lower heating value, lower water content, and larger AFR. The 90°C fuel was simulated at conditions that the 40°C fuel model identifies as optimal for efficiency. Due to the very low stoichiometric AFR of both fuel blends being evaluated a very high fuel flow rate is required. It was found early on in the conversion process that the port fuel injector models in GT-Power are not equipped to handle these large flow rates and this resulted in long simulation times. To remedy this calculation issue a simulated carburetor was created which supplies a homogeneous air/fuel mix to the intake manifold at a specified pressure and temperature. This change is reflected in the physical engine with the switch from port fuel injection to a gas carburetor upstream of the turbocharger, promoting better mixing of the fuel/air charge.

Table 3: Fuel Blend Compositions for Raw ATG and Selected Fuel Pretreatments

Fuel Pretreatment	Water	Carbon Dioxide	Carbon Monoxide	Hydrogen	Methane	LHV (MJ/kg)	AFR
Raw Tailgas	38.40	54.10	5.96	1.55	0.28	2.60	0.73
90°C Dewpoint	16.73	72.80	8.01	2.08	0.38	3.52	0.98
40°C Dewpoint	1.63	86.00	9.47	2.46	0.44	4.15	1.15

2.3.1: ANODE TAILGAS COMBUSTION MODELING

The significant change from natural gas operation to ATG operation was the inclusion of a predictive combustion model based on chemical kinetics and combustion data acquired from a cooperative fuels research (CFR) engine [15]. This model differs from a Wiebe function model in that it predicts a burn rate based on the composition of the in-cylinder charge rather than

prescribing a burn rate. Chemical kinetics predict the knock behavior of the ATG fuel. To develop this model combustion data is collected from the CFR engine, including in-cylinder pressure, dynamic intake pressure, and exhaust dynamic pressure. These three pressures combine with a 3D model of the CFR engine combustion chamber in GT-power to perform a "Three Pressure Analysis" (TPA) [15]. The TPA can calculate a burn rate from these three pressures. Using the burn rates from the prescribed conditions, GT-Power predicts the burn rate at different conditions. A more in-depth look at the construction of the predictive combustion model can be found elsewhere [15].

The developed combustion model was translated to the KDW993T by changing the engine geometry models while keeping all combustion parameters the same as in the CFR model, providing a predictive model of the KDW993T produced from a different engine geometry. This strategy is potentially risky due to using another engines geometry during the calculation of combustion characteristics and may need to be tweaked later on. To study the effect of compression ratio on combustion quality and efficiency, the model geometry must be flexible. It consists of a flat cylinder head with a bowl combustion chamber in the piston. The depth of this bowl is changed to adjust the clearance volume of the chamber. The spark location is to one side of the combustion chamber in the position of the former pre-chamber—validation against experimental data collected is performed in Chapter 4 to confirm this theory.

Difficulties arose integrating the combustion model into the 993T model. GT-Power has two different ways of modeling fuel. One is as an independent mix of gases "fluidmixture" in which the full chemical kinetics is captured, and knock modeling is enabled. The other is "fluidmixturecombined" where a "Pseudo species" is made combining the properties of each constituent interpolated from the mass fraction. The pseudo species method is used in natural gas

applications where a large number of hydrocarbons exist. During combustion modeling testing in Padhi's work, it was discovered that GT-Power would capture the water and carbon dioxide, which are part of the fuel, as part of the air [15]. Leading to incorrect reporting of parameters such as mass fraction burned, inducted fuel mass, and the air-fuel ratio [15]. To remedy this issue GT-Power support recommended modeling the fuel as a fluidmixturecombined. Fixing the reporting issues but introduced a new problem. Due to all species being modeled as a single entity, the chemical kinetics could no longer identify species such as hydrogen and carbon monoxide, and the knock reactions could not take place [15]. To capture both knock and accurate data reporting, both types of fuel models were run. Fluidmixture would be run first to establish the knock window. Then fluidmixturecombined would be run to report engine parameters such as torque, BSFC, and brake efficiency. These results would then be combined to provide the full operating envelope of the conditions being tested.

2.4 PREDICTIVE MODELING

Once initial gasification was complete and the difficulties with combustion modeling resolved, the modeling efforts were focused on improving the brake efficiency of the engine. To achieve the goal of 30% significant improvements would have to be made. During the running of initial models, it was discovered that due to the reduced mass flow through the engine, the stock TEL turbocharger was operating in the stall region and not producing any boost. To normalize results a model was constructed which supplied a high intake pressure 3 bar to a throttle valve. This valve was actuated by a PID controller, which targeted a constant power level of 14kW, the target for the developed prototype. This model would allow all further results to be comparable without turbocharger interference. The original diesel model was constructed with data that was obtained with a radiator fan, alternator, and diesel fuel pump. These parts were deemed

unnecessary for the developed prototype and were removed. The predictive friction model is split into reciprocating, rotating, and accessory friction. To simulate the removal of the accessories the accessory friction multiplier was set to 0, and is the case for all models unless stated otherwise.

2.4.1 MILLER CYCLE SIMULATIONS

The first method investigated to improve efficiency was Miller cycle valve timings. By delaying the IVC until later in the compression stroke, the effective compression ratio of the engine can be lowered. The effective compression ratio is the volume of the cylinder at TDC over the volume of the cylinder at IVC (rather than BDC as in the geometric compression ratio). In this configuration, the compression ratio will be less than the expansion ratio of the engine. The greater expansion ratio allows for an over-expanded cycle, theoretically extracting more work form the cylinder charge. To test the efficiency gains of this method the geometric compression ratio of the engine was kept unchanged from the stock value of 21:1. New intake valve profiles were created from stock to +60 CAD. The dynamic compression ratios of these valve profiles and IVC locations are presented in Table 4. As the delay in IVC increases, the dynamic compression ratio of the engine goes down; this has an effect of increasing the knock margin of the operating condition, as well as lowering in-cylinder mass at IVC. These two factors will change the location of knock initiation timing, as well as MBET. To account for this effect, the simulation was performed by setting the desired engine speed and power and sweeping ignition timing from 40 to 10°BTDC. The ignition sweep was repeated for selected speeds.

Table 4: Tested Miller Cycle Ratios

IVC Reference	IVC (°BTDC)	Dynamic CR	Miller Ratio λ
0 (Stock)	134	18.75:1	0.954
30	104	14.89:1	1.201
45	89	12.39:1	1.444
60	74	9.69:1	1.846

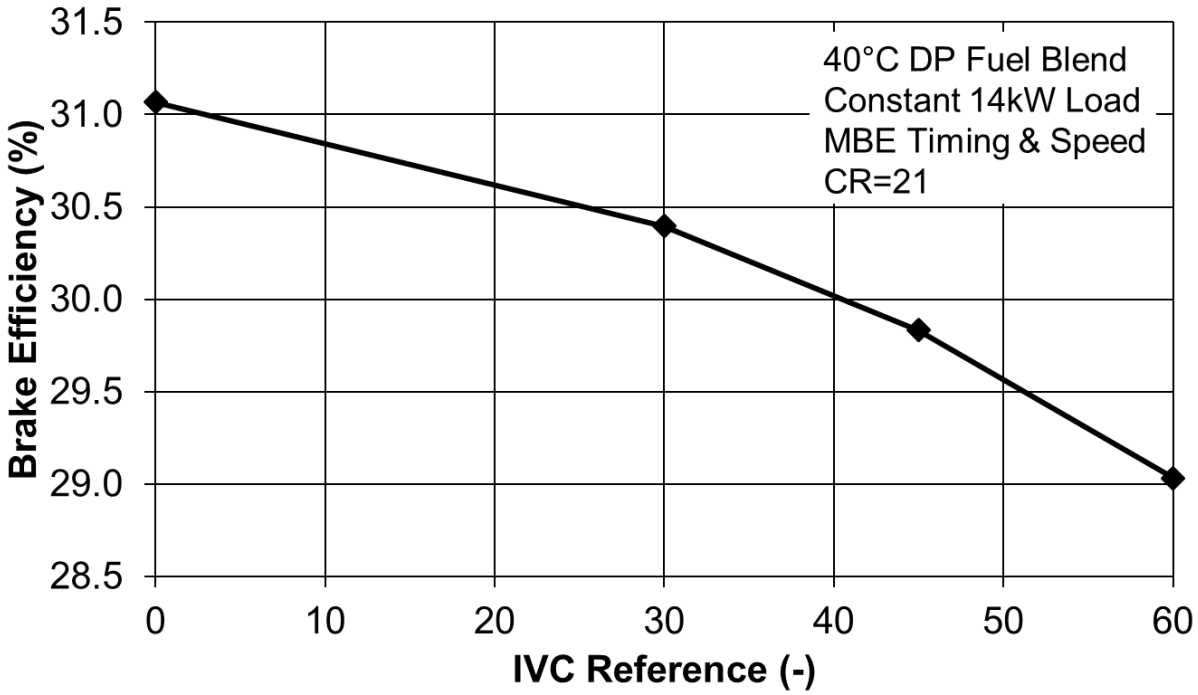

Figure 16: Brake Efficiency for Different Miller Cycle Timings

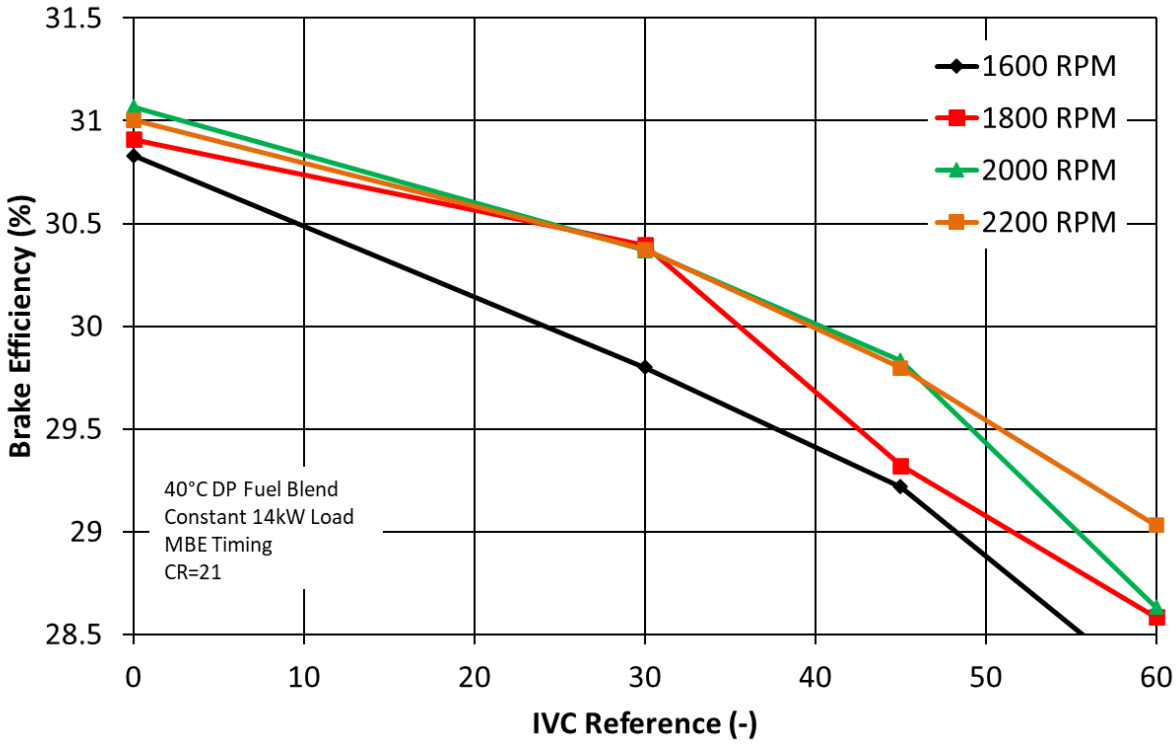

Figure 17: Brake Efficiency for Miller Cycle Timings at Selected Speeds

In Figures 16 and 17, the sweep of Miller cycle valve timing can be seen. The primary trend identified in this sweep is that the Miller cycle valve timings had no benefit to brake efficiency. A possible cause of this is that as IVC is delayed, more mass is pumped back into the intake manifold, increasing pumping losses. Due to the simulation running at a constant power level, the mass flow rate through the engine is relatively constant. Equation 7 shows that with constant power and LHV, the fuel mass flow will be a function of brake efficiency. So the trapped mass in the cylinder must increase with decreasing efficiency. This effect can be observed in Figure 18, where the trapped mass per cycle increases with decreasing efficiency at a constant speed.

$$\dot{W}_{brake} = LHV_{fuel} * \dot{m}_{fuel} * \eta_{brake} \quad (7)$$

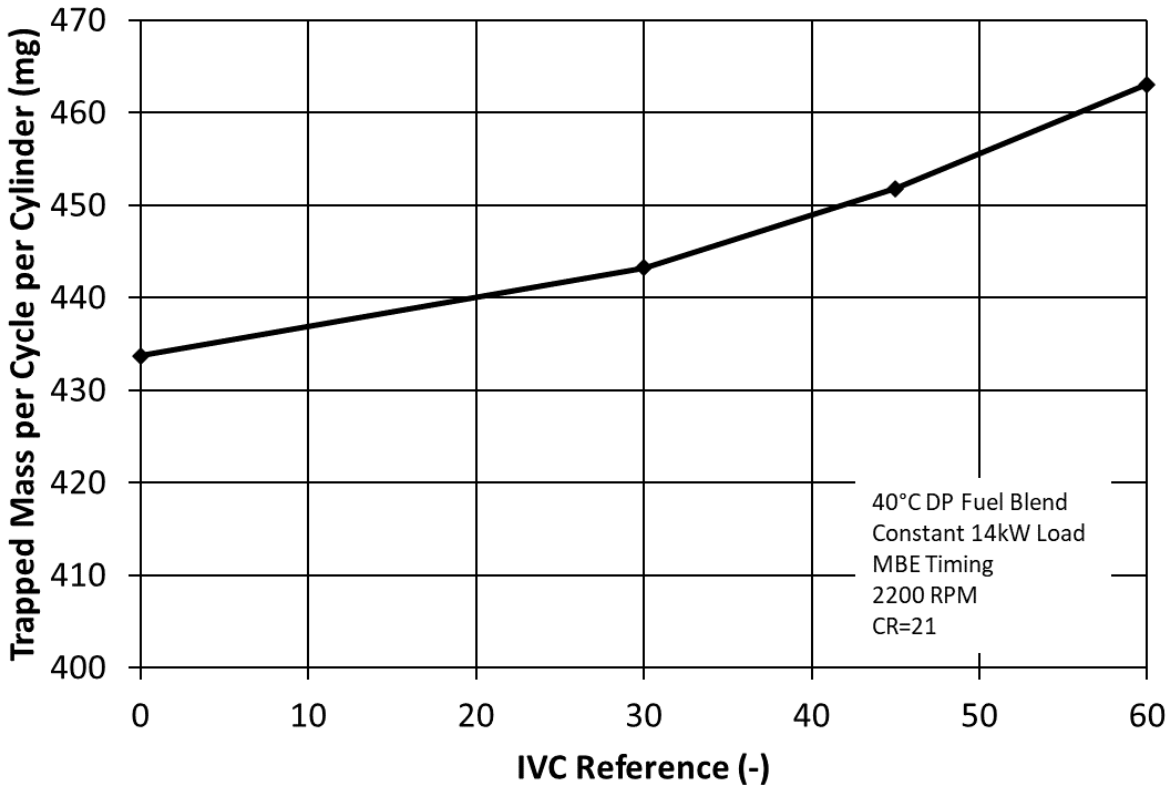

Figure 18: Trapped Mass for Miller Cycle Valve Timings at Constant Speed and Power

Since the volume of the cylinder will be less at later IVC timings, the cylinder pressure must be higher. This further increases pumping losses due to the engine pumping back against a higher intake pressure for longer. This loss can be seen with the exponential decline in efficiency as the IVC event becomes later in Figure 17. In Figure 19, PMEP is plotted for each Miller cycle timing as the IVC event is delayed; the PMEP of the engine increases. PMEP is a loss and decreases brake efficiency.

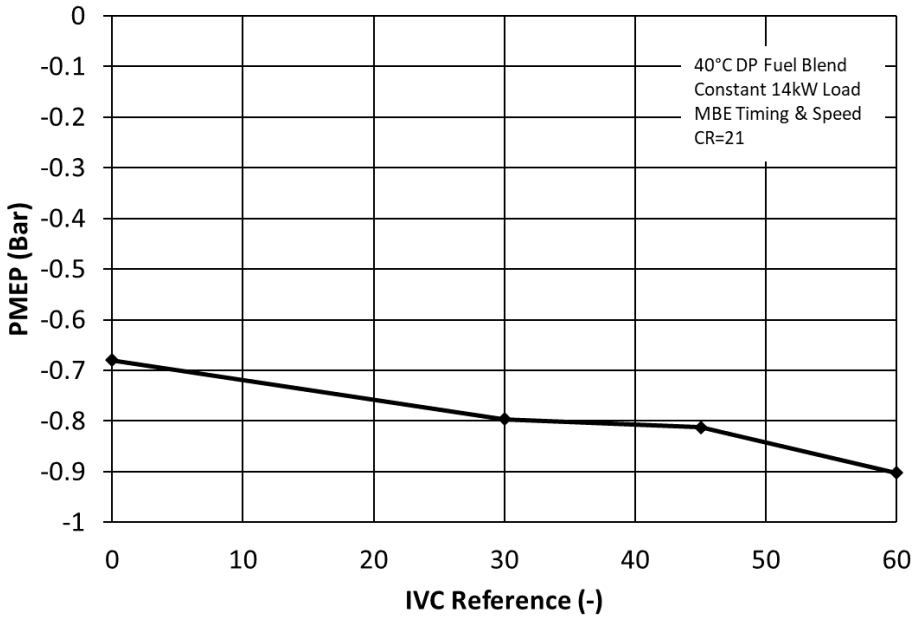

Figure 19: PMEP for Different Miller Cycle Timings

2.4.2 COMPRESSION RATIO SIMULATIONS

The next significant variable to tune for the engine was the compression ratio. Since the compression ratio significantly impacts the combustion quality of the fuel, the ignition timing significant variable. Higher compression ratios will greatly decrease the knock free window. To capture this the ignition timing was swept from 40 to 10°BTDC with the fluidmixture model to identify the knock limits. The sweep was repeated from the knock limit to 10°BTDC with the *fluidmixturecombined* model to identify MBET. These sweeps were repeated for four selected operating speeds to identify any differences in efficiency at different speeds. The change in the compression ratio was achieved by enlarging the clearance volume at TDC. This change in volume was done by increasing the depth of the piston bowl for the desired compression ratio. The results of these sweeps are shown in Figure 20. The plot for the most efficient speed 2000RPM is presented in more detail in Figure 21.

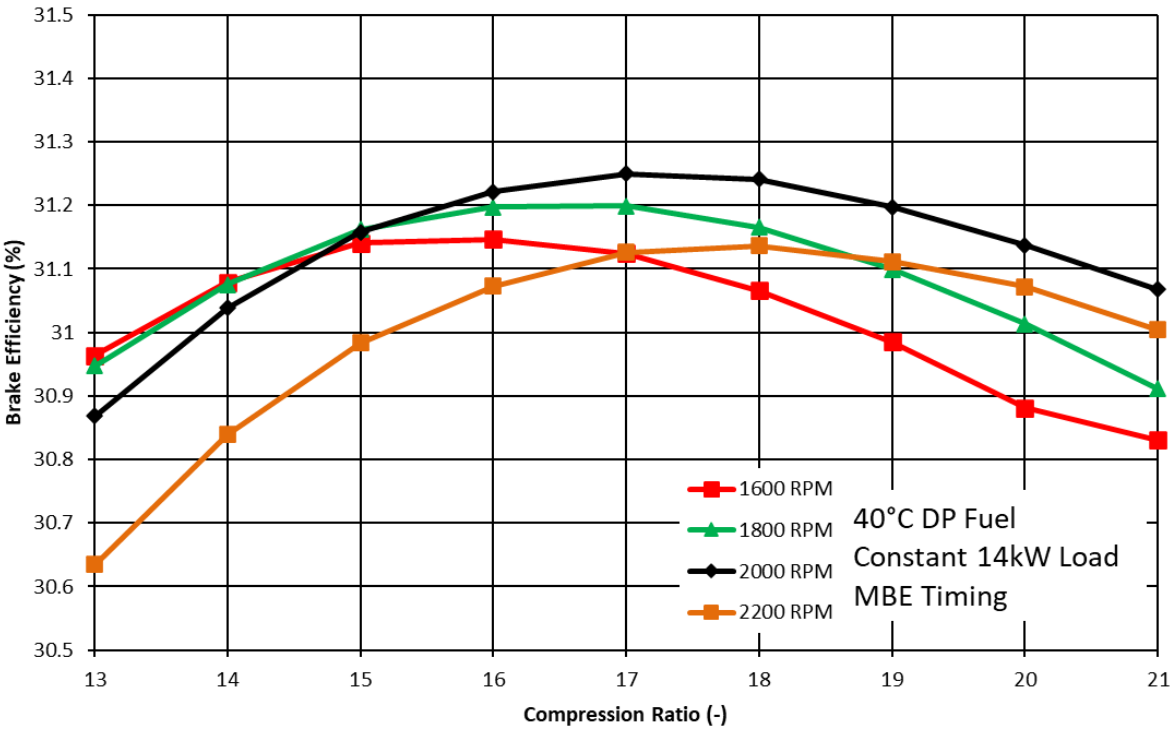

Figure 20: Brake Efficiency vs. Compression Ratio for All Tested Speeds

It is interesting to note from these sweeps that there is a peak in brake efficiency at a compression ratio of 17:1 for every speed except 2200, where 18:1 is the most efficient—going against conventional wisdom, where higher compression ratios result in higher efficiencies.

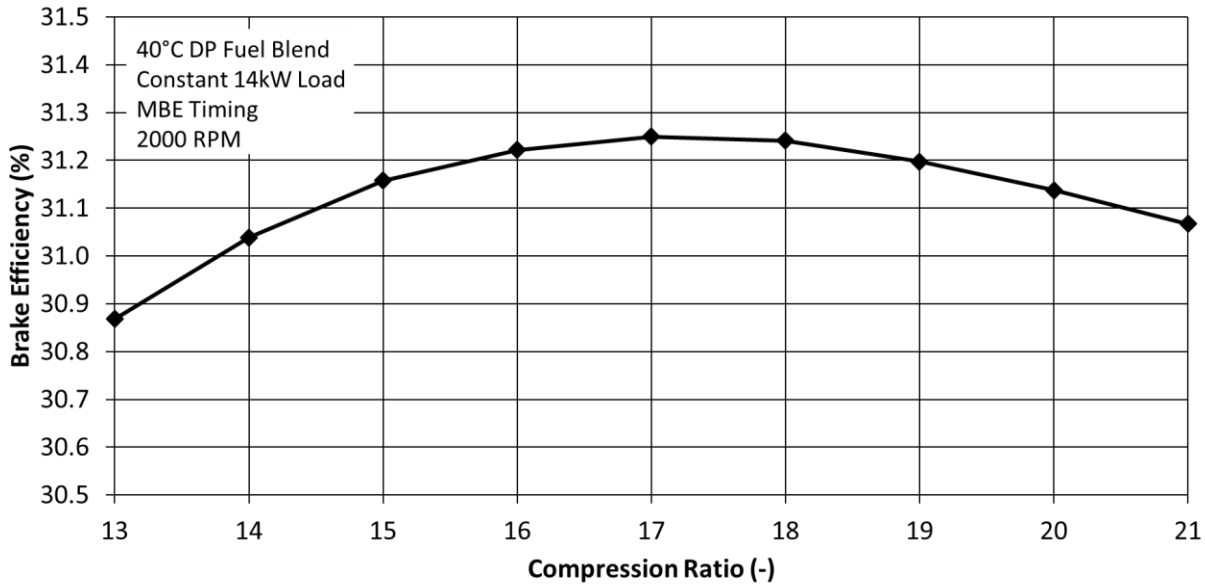

Figure 21: Brake Efficiency for Different Compression Ratios at 2000 RPM

This drop-in efficiency could be due to quenching, which occurs when the flame front in the cylinder encounters an obstruction, such as the cylinder wall, or piston. The flame goes out as it approaches the wall, due to heat transfer effects whereby the heat transfer to the surface is higher than the heat needed to sustain the flame, and the reaction stops. At higher compression ratios, there is more opportunity for quenching to occur due to the higher surface to volume ratios. On the macro scale, due to the higher surface to volume ratio, bulk heat transfer out of the cylinder may be higher at high compression ratios. Another factor that may affect this is the cylinder head and piston are made of aluminum while the block is made from cast iron. Aluminum has a thermal conductivity of 237 W/m*k, while cast iron has a thermal conductivity of 52 W/m*k [19]. For larger CRs and smaller clearance volumes, a larger fraction of the area is made of aluminum. This higher aluminum surface area increases the average thermal conductivity and likely resulting in the overall heat transfer out of the cylinder being higher than when the clearance volume is larger, and the average thermal conductivity is smaller. Possible

additional effects at high compression ratios could be turbulence. Moderate turbulence improves flame propagation and combustion efficiency in ICEs. But too much turbulence can hinder flame kernel growth during ignition. At high compression ratios, the high turbulence caused by the low clearance volume could be hindering flame development lowering overall combustion efficiency and leading to a failure to extract energy from the fuel. Subsequent simulations would are carried out with the most efficient compression ratio of 17:1.

2.4.3 TURBOCHARGER SIMULATIONS

Once standardized testing of valve timing and compression ratio had been completed, the forced induction strategy was examined. The original TEL turbocharger is sized for a 40 kW application. Figure 22 shows that the turbocharger on the original 993T did not start producing an adequate boost until 2200 RPM. This speed is above the maximum efficiency speed of 2000 RPM that was identified previously during compression ratio optimization.

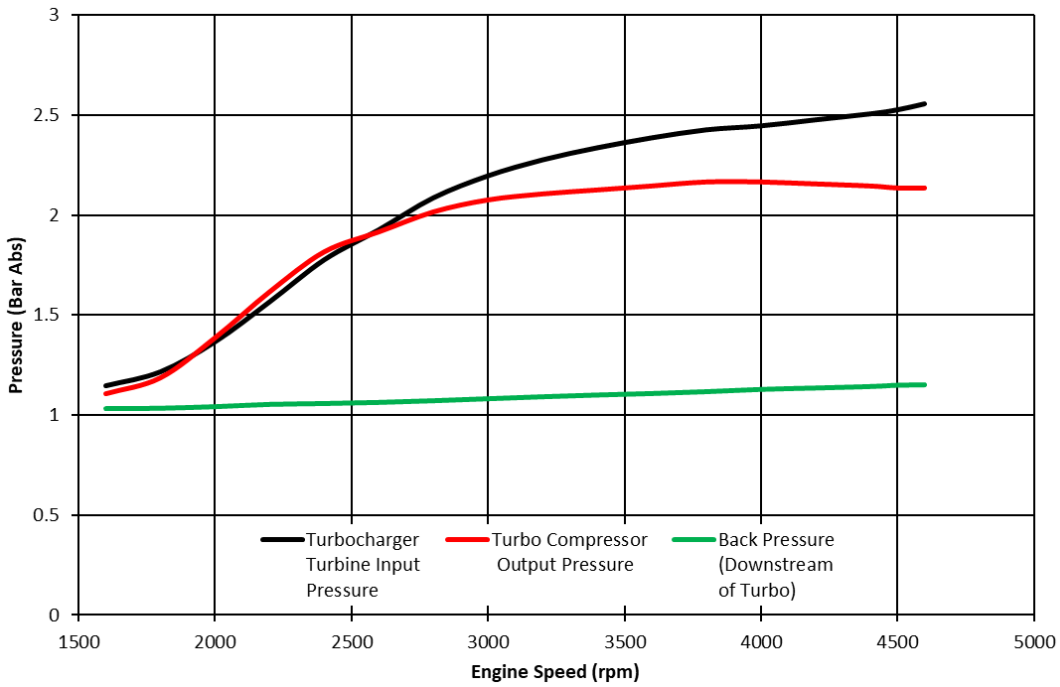

Figure 22: Stock TEL Turbocharger Characteristics

Simulations were run with the TEL turbocharger model, and it was found that the compressor was operating deep within the stall region. Compressor stall is a dangerous condition for turbomachinery. During a compressor stall, the flow inside the stage has separated from the rotor and operates unpredictably. Flow oscillations occur and frequently result in reversion through the compressor stage. Because the mixer is located upstream of the compressor, this is an extremely unfavorable condition for the physical prototype. Reversion of flow around the mixer results in fluctuations in the venturi vacuum. Causing oscillations in the fuel low rate and could cause instability in the AFR. To address this issue a new turbocharger had to be identified. Locating a turbocharger requires two main parameters: the mass flow rate, and the desired pressure ratio at a given operating condition. The *simulated turbocharger* model used to model the previous simulations provides both those measurements downstream of the throttle valve. These conditions can be seen in Figure 23.

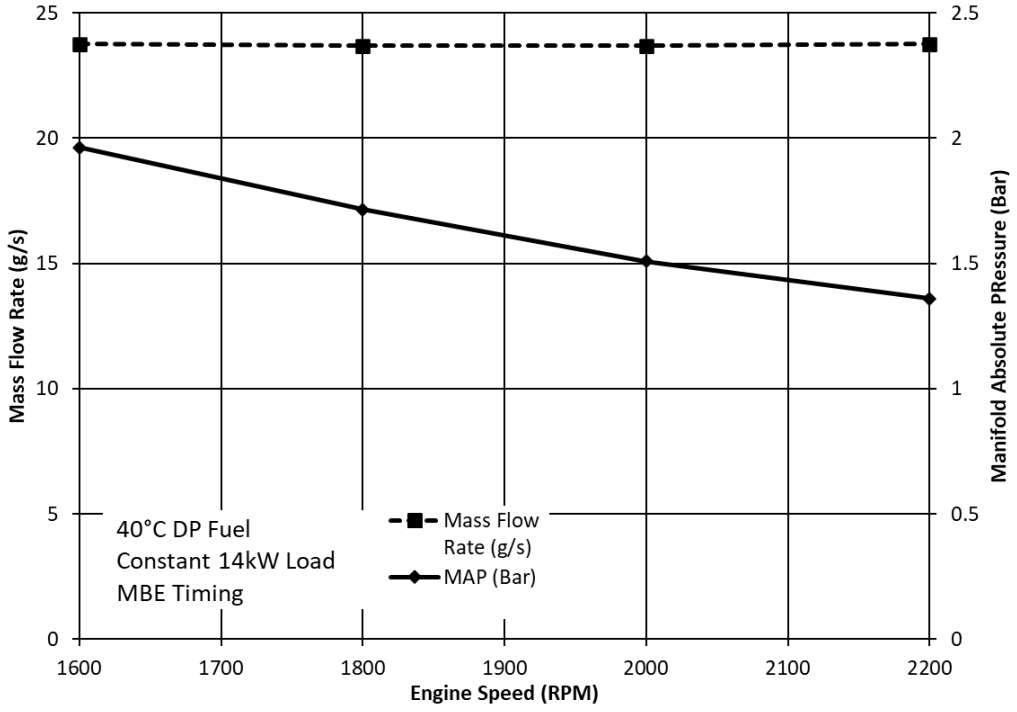

Figure 23: Mass Flow Rate and Boost Pressure vs. Speed

Similar measurements are needed for sizing the turbine, but rather than selecting an exhaust pressure, the compressor operating condition will determine the turbine. The compressor will need a certain shaft speed to create the required boost and mass flow rate since the mass flow rate will be the same at the intake and exhaust the exhaust backpressure will be determined by the shaft speed required. A wastegate will regulate the exhaust backpressure, allowing some of the exhaust flow to bypass the turbine, thus reducing the exhaust backpressure. To control the shaft speed the wastegate can be opened or closed depending on the needs of the engine. Using these parameters a turbocharger can be selected. A suitable turbocharger from Ishikawajima-Harima Heavy Industries (IHI), the RHF-25 was chosen for its ability to produce high boost pressures at low flow rates required by this engine. This turbocharger is OEM equipment on several small automotive engines. These cars are notable for their low displacement engines legally mandated to be 0.66L or lower. Making the RHF-25 optimal for use in the low displacement 993T. The IHI compressor and turbine maps are proprietary, so they cannot be shown. However, an example of compressor and turbine maps are shown in Figure 24a and 24b respectively.

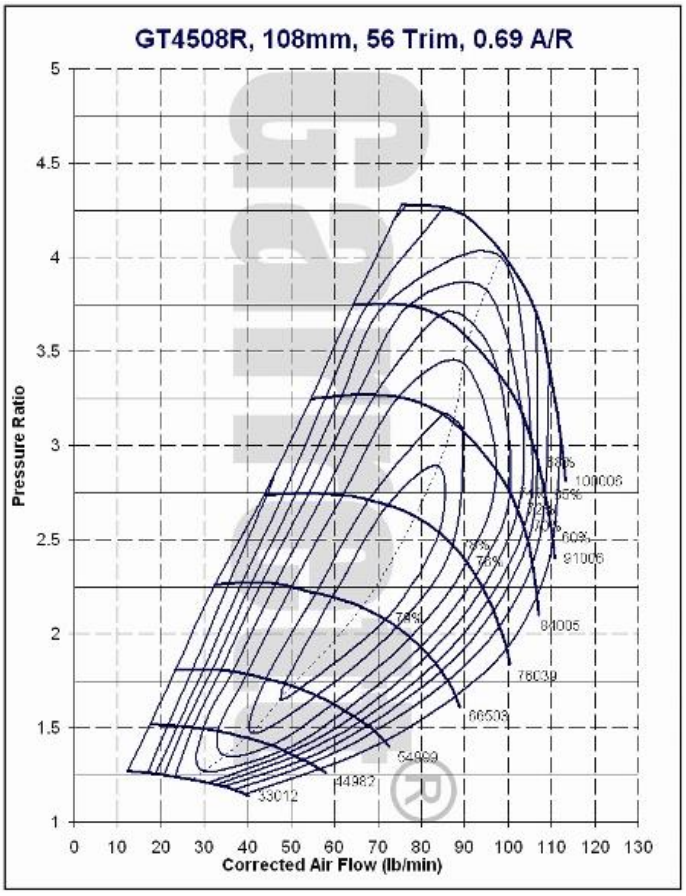

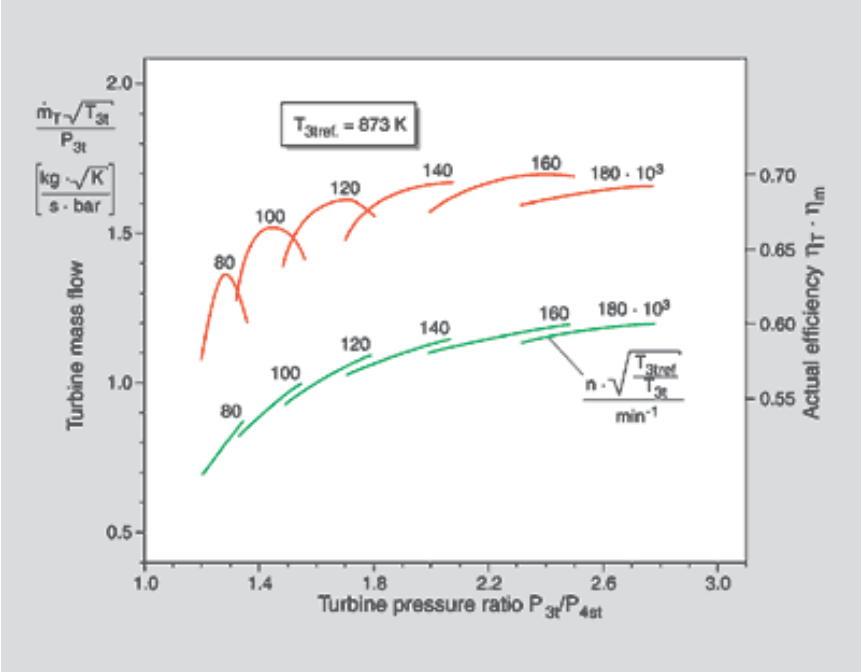

Figure 24 a) Compressor Map b) Turbine Map [Courtesy of Garret Corporation]

The IHI turbo was modeled in GT-Power using the provided templates. A PID wastegate controller was added to regulate the boost pressure to control the engine to 14kW. Initial testing showed that due to the small size of the IHI turbo (<1in diameter compressor wheel), the isentropic efficiency of the compressor was low. Resulting in excessive heating of the intake charge, which not only reduced volumetric efficiency but also substantially decreased the knock limit. To compensate for this heating, an intercooler was added to the system to reduce charge air temperatures. This intercooler ran in two configurations depending on the fuel being simulated. For the 40°C fuel the intercooler was cooled by 30°C air, for the 90°C fuel it was cooled by 95°C engine coolant. Water knockout is performed in a separate heat exchanger; the goal of the intercooler is to cool the gas after it exits the compressor. The 40°C fuel was tested first with the IHI turbocharger. Using the same standard timing sweep from 40 to 10°BTDC with both the fluidmixture model to identify the knock limit. And the fluidmixturecombined model from knock limit to 10°BTDC to identify MBET. These sweeps were repeated for the selected four speeds. During the simulations, it was essential to locate the knock limits and the proximity of MBET to the knock limit. Knock maps were constructed for each operating point to better visualize the safe and optimal operating area for the model. This map is a 3D graph where engine speed is on the x-axis, ignition timing is on the y-axis, and the compression ratio is on the z-axis. A slice can be taken at a given compression ratio to show the safe operating regime in that configuration. Two potential engine compression ratios have been identified at this point, stock 21:1, and the more efficient 17:1. Knock maps for both these configurations can be seen in Figures 25 and 26 respectively.

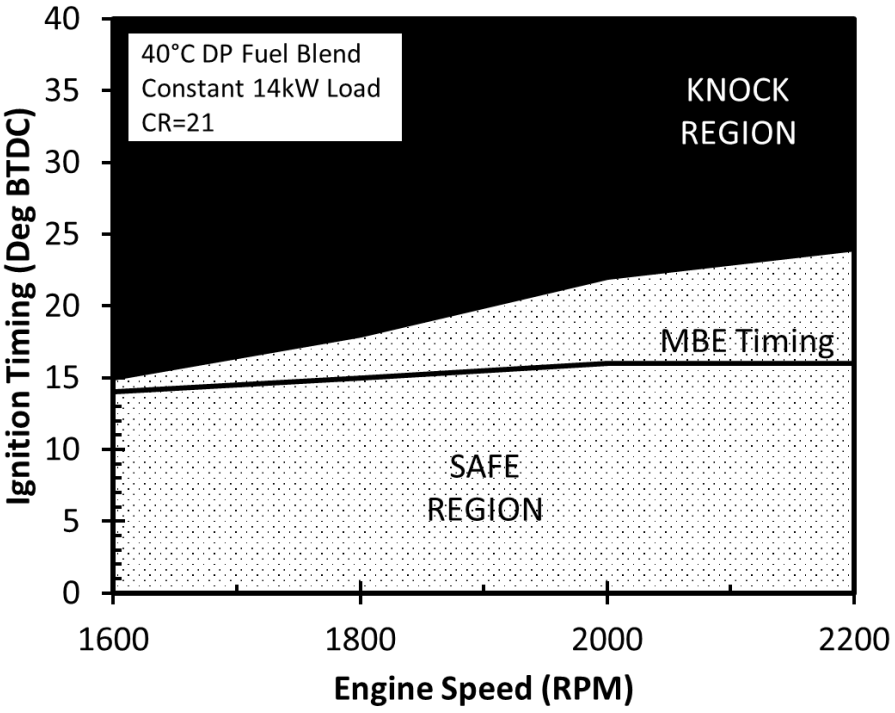

Figure 25: Knock map for 21:1 Compression Ratio

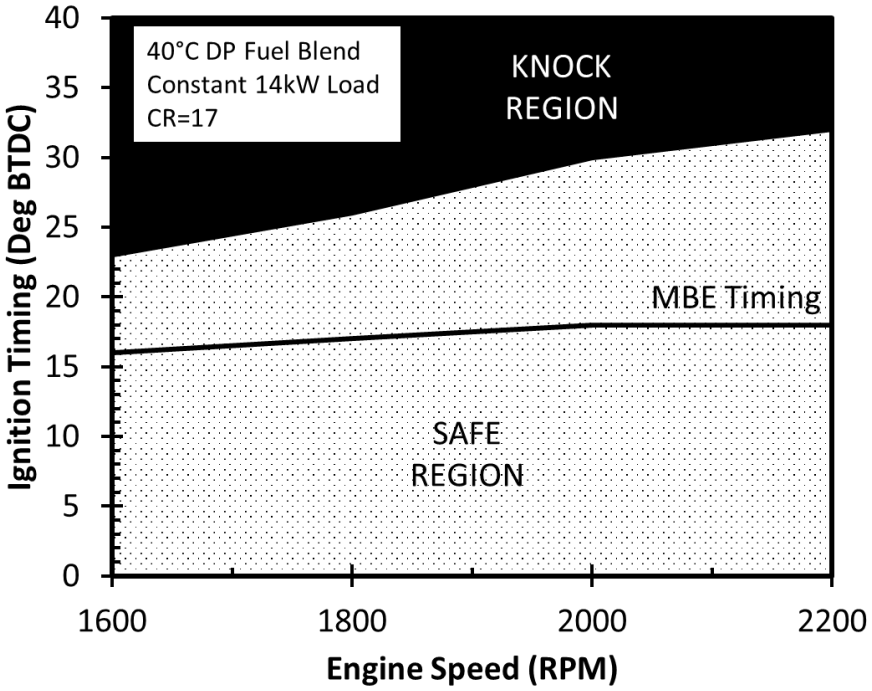

Figure 26: Knock Map for 17:1 Compression Ratio

While the 21:1 compression ratio would be easier from a manufacturing perspective because it requires less modification, higher efficiency is predicted for the 17:1 compression ratio. The ultimate reason for choosing 17:1 over 21:1 came down to the operation knock margin. Looking at Figure 25 the MBET line is extremely close to the knock limit. This does not leave much margin for controllability during operation. At the low engine speed of 1600 RPM, there is only 1 deg difference between MBET and knock initiation. This margin is much broader, looking at Figure 26, where 7 deg of margin exists at 1600 RPM. The margin only gets wider as engine speed increases. This effect is due to knock having less time to occur as speed increases. Since combustion duration is a relatively constant time at any engine speed, the crank angle duration of the event increases as engine speed increases. This phenomena is why ignition must be advanced as engine speed increases. This effect also has the effect of decreasing the time knock precursor reactions have to take place, so the knock limit moves more advanced as engine speed increases. The 90°C fuel was tested under similar conditions as well. The knock maps for this fuel can be seen in Figure 27.

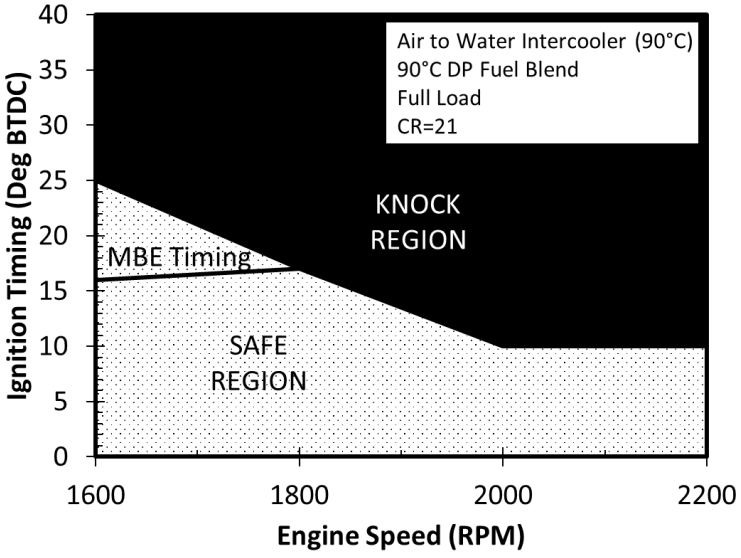

Figure 27: Knock map for 90°C fuel at a Compression Ratio of 21:1

This knock maps look much different compared to the maps presented for the 40°C fuel in Figures 25 and 26. This difference is not due to changes in fuel combustion characteristics due to the difference in composition., but rather the operation of the turbocharger. Since the 90°C fuel has a lower LHV than the 40°C fuel the engine was unable to operate at 14kW utilizing the 90°C fuel. It is operating at full load, which is causing the turbocharger to work at maximum capacity. As seen in Figure 28, the MAP steadily decreases for the 40°C case as the engine speeds up. This effect is due to the mass flow rate through the engine being a function of engine efficiency since power is held constant. So as the volume flow rate passing through the engine increases with increasing speed, the pressure decreases to keep the mass flow rate relatively constant. Since the 90°C case is not operating at 14kW, the wastegate is fully closed for the whole duration, and the turbocharger is spooling up as engine speed increases. Since the turbocharger is operating at maximum load under these conditions, the intake charge is extremely hot exiting the compressor.

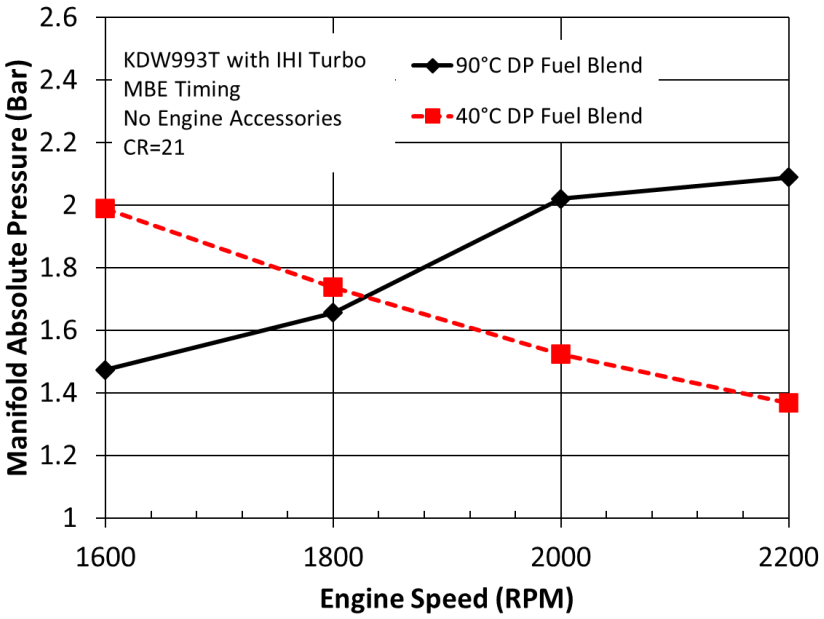

Figure 28: MAP vs. Engine Speed for 40°C and 90°C Fuel Blends

Combined with the higher 95°C coolant temperature for the 90°C cases leads to the excessively high intake air temperature. This effect can be seen in Figure 29, for the 40°C case as the turbocharger works less as engine speed increases, intake air temperature decreases. But for the 90°C case intake air temperature increases as engine speed increases. This heating leads to a reduction in the knock window as the engine speed increase. But as speed increases, the speed effect of knock reduction takes over, and the knock window levels out.

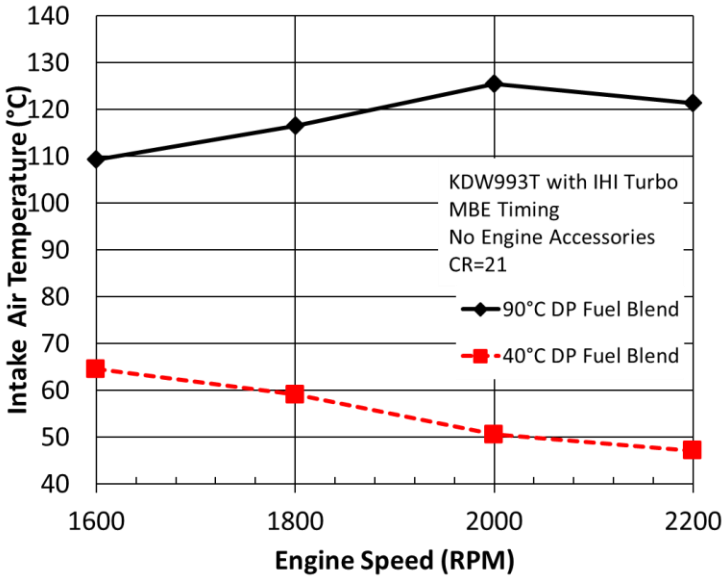

Figure 29: Intake Air Temperature vs Engine Speed for 40°C and 90°C Fuel Blends

The configuration that the GT-Power model predicts as most efficient is: stock valve timing, 17:1 compression ratio, IHI turbocharger, and an intercooler. This configuration has a predicted maximum brake efficiency of 31.25%.

2.4.4 PATHWAY TO 35% BRAKE EFFICIENCY

While 31.25% brake efficiency meets the goal of 30% brake efficiency, a pathway to 35% brake efficiency must be established. To accomplish this goal several more creative strategies must be tested on the model. These include friction-reducing coatings, a custom

turbocharger with high isentropic efficiency, and using the SOFC fuel cell stack blower as a source of pressurized air for the engine itself. These simulations were all performed at the maximum efficiency speed and a compression ratio of 2000 RPM and 17:1 previously identified. Ignition timing was swept from 40 to 10°BTDC to determine the knock limits and MBET. To simulate a custom turbocharger with high efficiency at the operating point the turbocharger model was changed. Rather than using a standard compressor and turbine map. Constant isentropic efficiency of 70% for the compressor and 65% for the turbine was used. Part of the goal for the developed engine is to drive the fuel cell stack blower on a common shaft. This blower will produce 3 bar of pressure for the stack. Consideration was given to bleeding air from the blower supply for use in the engine. In this supercharged configuration, there were two exhaust schemes tested as well. One where the exhaust was discharged back into the cathode exhaust stack, upstream of the expander at 3 bar of pressure, and one where the exhaust is discharged to atmosphere at 1 bar through a muffler. The final method tested for efficiency improvement was friction-reducing coatings on the piston skirts. To simulate these coatings the reciprocating component of friction was reduced by 25%; all other parts remained the same.

In Figure 30, all of these configurations can be seen. The lowest efficiency tested was the IHI turbo with all engine accessories attached at 30.1% efficiency with the 40°C fuel blend. Note that for all modeled turbocharger cases that the 40°C fuel is more efficient than the 90°C fuel due to the turbochargers being unable to provide sufficient boost to reach 14kW. When simulated conditions are used for the supercharged cases, both fuels have similar efficiency. The next case tested was the developed prototype with an efficiency of 31.25%. The high isentropic efficiency turbocharger was not much of an improvement over the IHI turbo at 31.5% efficiency.

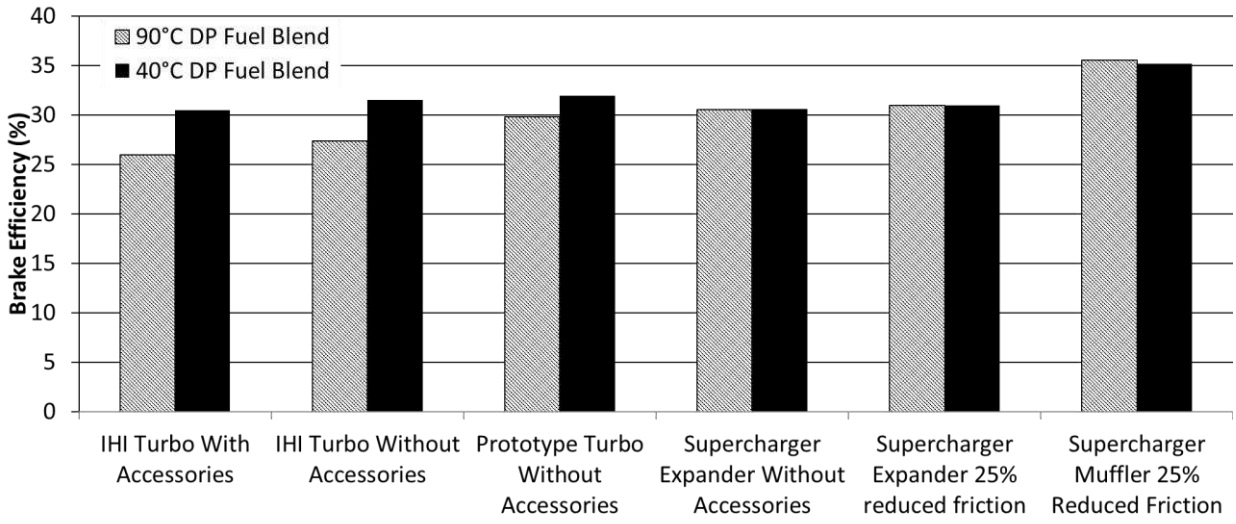

Figure 30: Pathway to 35% Brake Efficiency

Given the cost of developing and manufacturing a custom turbocharger, this pathway is likely not the most cost-effective way to improve efficiency. The supercharged cases represent the most promising pathway. When the exhaust is discharged to the cathode stack upstream of the expander, the brake efficiency is similar to the turbocharged efficiencies and is worse for the 40°C blend at 30.2% efficiency only surpassing the IHI case with accessories still attached. Friction reducing coatings on the high back pressure supercharged case did not help much, increasing efficiency to 30.35%. The most promising case is the final one, where the engine is allowed to exhaust through a muffler to the atmosphere, significantly reducing backpressure. The backpressure had a substantial effect on brake efficiency, increasing from 30.35% to 35.0% for the 40°C case, and 35.2% for the 90°C case. This efficiency gain is due to the decreased pumping losses from the reduced backpressure. This case is the most promising to achieve 35% efficiency. Still, this model does not capture the full effects of using the supercharger, such as increased shaft power needed to drive the blower, and it assumes that a 25% reduction in

reciprocating friction is achievable in the current engine. More study will be required if this case is selected for further development.

2.5 FINAL PROTOTYPE GUIDANCE

All of the modeling results were used to guide the development of the physical prototype engine. Consulting with Kohler it was decided to move forward with the IHI turbocharged version of the engine, with a 17:1 compression ratio. This configuration was selected because it would offer the most flexibility in testing. This configuration also provides the highest brake efficiency without extensive modifications such as antifriction coatings. The test skid at the CSU Powerhouse has a supercharger powered by a VFD driven electric motor, and an exhaust back pressure valve, which will allow testing of the supercharged versions and any potential turbocharger that could be placed on the engine.

CHAPTER 3: EXPERIMENTAL SETUP

3.1 PROTOTYPE ENGINE

For the physical testing, a Kohler KDW993T engine was commissioned as an ATG fueled prototype. The original engine specifications can be found in Table 1. This prototype was converted from a CI engine to SI by Davinci Engineering and Consulting in Oshkosh, WI. Modifications performed included removing the diesel injectors and fitting spark plugs in their place with a spark plug adapter. The valve cover was modified to install a coil on plug ignition system. The stock diesel pistons were modified to keep the compression ratio the same after the removal of the pre-chamber volume. Installation of a crank position sensor for ignition synchronization was performed. Modification of the exhaust was carried out to accept a new turbocharger and narrowband oxygen sensor. The intake was adapted to mount an Impco model 100 gas mixer. All electrical components were wired to a Pi Innovo M220 Open ECU. The prototype was then delivered to Kohler Power Sytems in Kohler, WI, where it underwent development of the ECM software and verification of timed spark. The engine was then delivered to the CSU Powerhouse. The engine as delivered, can be seen in Figures 31-34.

To supply ATG fuel blends to the engine a blending system was designed and built around the engine test cell. This blending system draws the calorific gases from bottles outside; carbon dioxide is drawn from eight dewars inside the lab. Due to the high flow rate of carbon dioxide the dewars had to be placed in a room with space heaters to ensure sufficient vaporization of the carbon dioxide. The eight dewars are split into two supply chains with four dewars feeding a 1kW inline gas heater. The gas is then passed through a 200W heated regulator

and the supply streams are mixed into one supply line to the blending system. This heating ensures that the regulators' do not freeze due to the rapid vaporization of a large quantity of cryogenic carbon dioxide. The gases travel to a fuel mixing manifold where they are blended. The exact proportions of these blends are controlled by Omega mass flow controllers and a Labview program, which controls these controllers in a locked ratio predetermined by the blend being tested. A PID controller is used to control the desired fuel pressure in the fuel manifold. The individual mass flow rates are summed to ensure that the mix composition is correct. The gases then pass to the steam manifold where steam is injected into the gas mixture from a steam generator. The full gas mixture then passes through a Krohne Optimass 6400C Coriolis mass flow meter that provides the full flow measurement for use in efficiency calculations. The high-pressure mixture passes through two Itor B42 regulators in parallel to regulate down to 0.75 psig, this gas is then supplied to a zero pressure regulator with a variable outlet pressure. The low-pressure gas then flows from the regulator to the gas mixer on the engine.

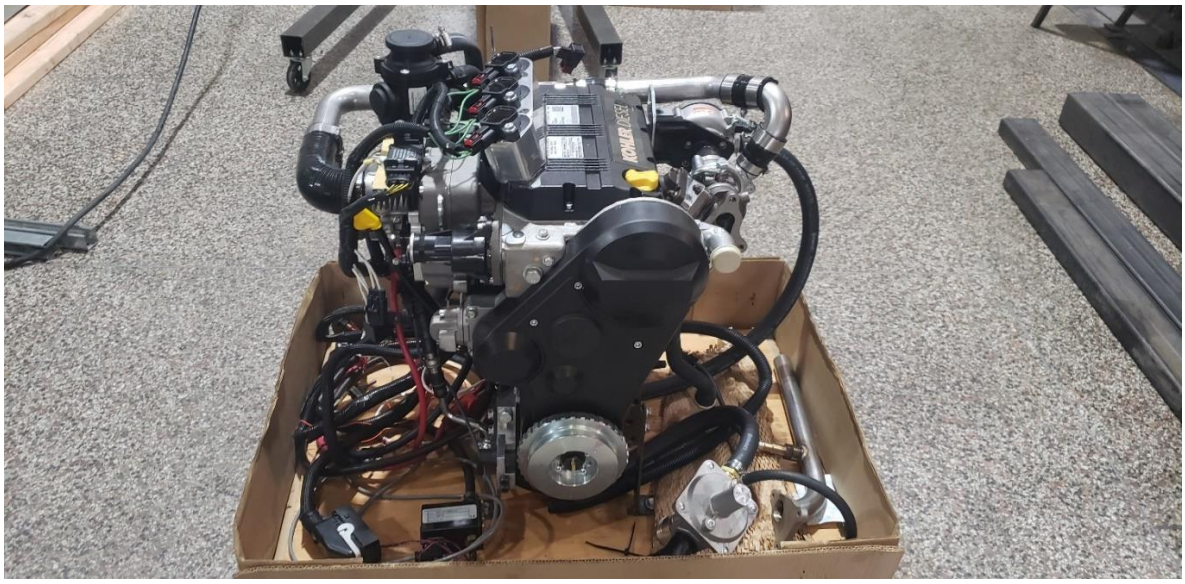

Figure 31. Delivered Engine Front View

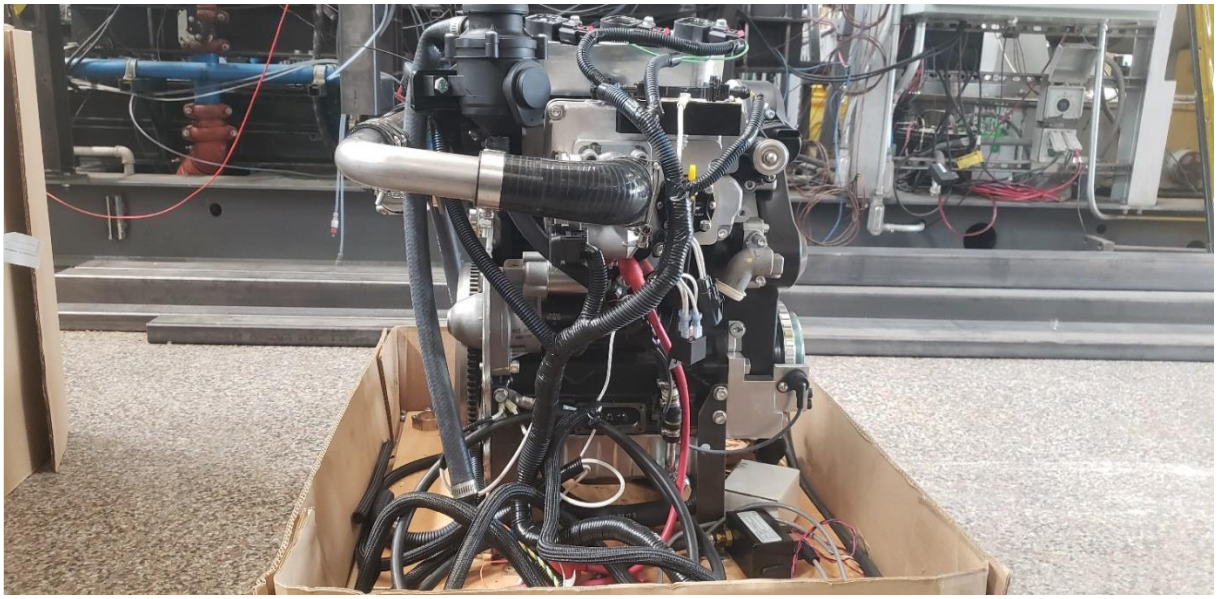

Figure 32. Delivered Engine Intake Side

Figure 33. Delivered Engine Exhaust Side

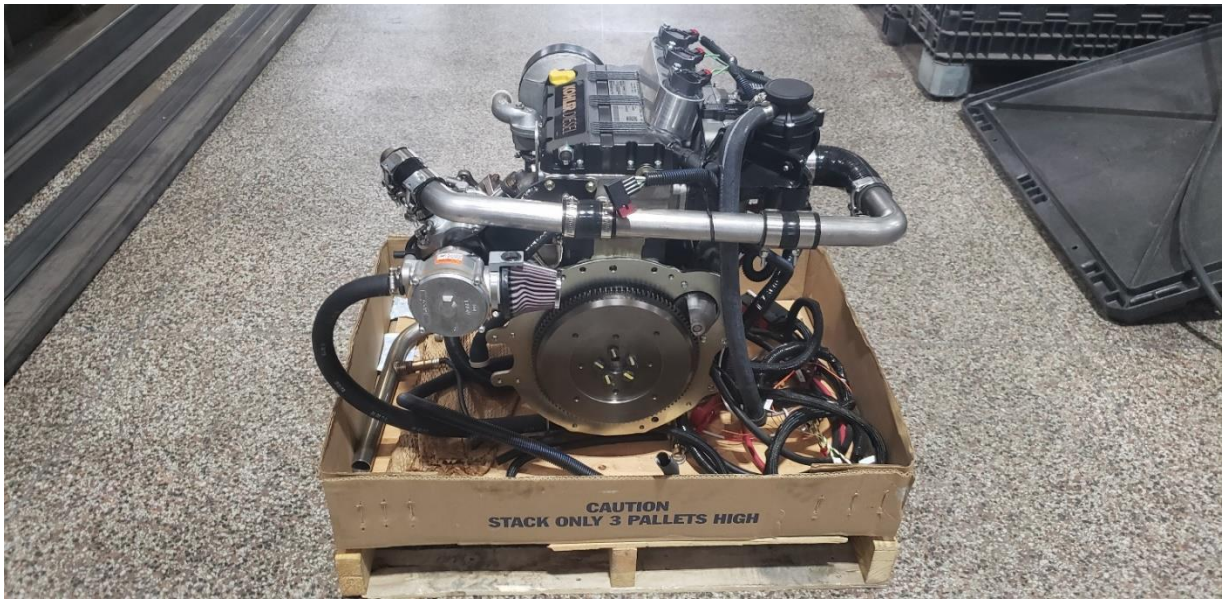

Figure 34. Delivered Engine Back

3.2 ON-SITE ENGINE MODIFICATIONS

From GT-Power modeling in Chapter 2 it was found that there is an expected efficiency peak with a compression ratio of 17:1. This peak was found too late for Davinci Engineering to perform the required modifications. This reduction in the compression ratio was implemented on-site at CSU. A spare stock 993T had been delivered to CSU ahead of the prototype engine. This engine was disassembled to remove the stock diesel pistons seen in Figure 35a. A new piston crown design based on the design by Davinci Engineering was created. This new design had an increased bowl volume so that the clearance volume was increased. The design can be seen below in Figure 35b. This design was then fabricated in house at CSU, the results of which can be seen in Figure 35c. The prototype engine disassembled so that the 21:1 pistons could be replaced with the new 17:1 pistons. Photos detailing these operations can be seen in Figures 36-37. During this process, a potential hot spot was identified at the lip where the pre-chamber was located. This sharp lip could potentially become a location where knock initiates. The cylinder

head was sent to the in-house machine shop to have an exterior fillet machined at this location to eliminate the potential hot spot. The results of this work can be seen in Figure 37. The prototype engine was then reassembled and prepared for commissioning.

Figure 35:a) Stock Diesel Piston b) 21:1 Piston, c) 17:1 Piston

Figure 36. Modified 17:1 Pistons Ready for Installation

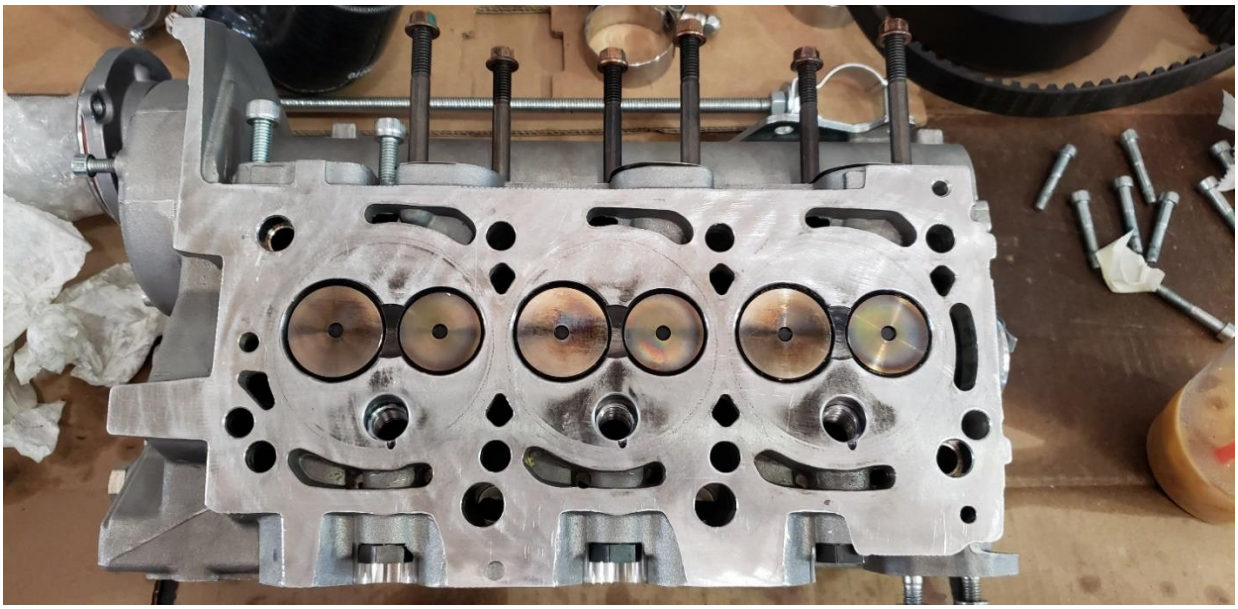

Figure 37: Modified Cylinder Head

3.3 CSU FACILITIES

Several modifications were made to the engine to collect selected temperatures and pressures at various locations. Critical measurements to be made include engine speed, brake torque, intake/exhaust manifold pressure, intake/exhaust manifold temperature, fuel flow, equivalence ratio, A complete lists of these metrics are available in Table 5.

Table 5: Critical Engine Metrics

Measurement	Unit	Instrument
Engine Speed	RPM	Dyn-Loc IV
Torque	N*m	Dyn-Loc IV
Power	kW	Calculated
Ambient Pressure	PSIA	Omega Oil Filled Pressure Transducer
Ambient Temperature	°F	Omega K-Type Thermocouple
Inlet Air Temperature	°C	Omega K-Type Thermocouple
Intake Manifold Temperature	°C	Omega K-Type Thermocouple
Intake Manifold Pressure	Bar Abs	Omega Oil Filled Pressure Transducer
Exhaust Port Temperature (Cylinder #1)	°C	Omega K-Type Thermocouple
Exhaust Manifold Temperature	°C	Omega K-Type Thermocouple
Exhaust Manifold Pressure	Bar Abs	Omega Oil Filled Pressure Transducer
Equivalence Ratio	-	Bosch Wideband Oxygen Sensor
Totalized Fuel Flow	g/s	Krohne Optimass 6300C
Constituent Fuel Flow	SLPM	Omega Mass Flow Controller
Fuel Manifold Pressure	Bar Abs	Omega Oil Filled Pressure Transducer
Fuel Manifold Temperature	°C	Omega K-Type Thermocouple
Fuel Power	kW	Calculated
Brake Efficiency	%	Calculated

High speed combustion data was collected alongside these slow speed measurements. This was done through the use of Kistler type 6013C dynamic pressure transducers installed in the former glow plug locations. An indicator passage was drilled from the glow-plug port to the cylinder to record cylinder pressures (detailed in Figure 38). These transducers are paired with a 0.1° resolution encoder coupled to the crankshaft to resolve cylinder pressure to crank angle. This data is captured by a national instruments high-speed data acquisition system, running a custom CSU Labview program for analyzing combustion data. This system can measure cylinder

pressure, apparent heat release, indicated mean effective pressure (IMEP), pumping mean effective pressure (PMEP), and knock intensity averaged over 100 cycles. The test cell configured for validation testing can be seen in Figure 39.

Figure 38: Indicator Passage Location

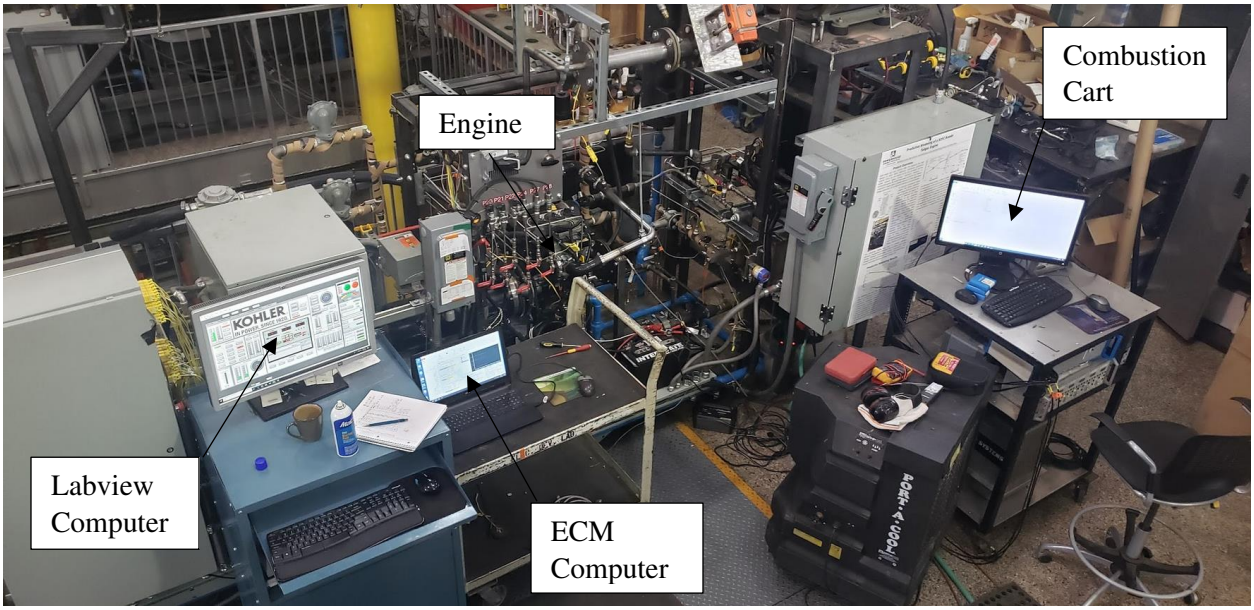

Figure 39: CSU Test Cell

3.4 ENGINE COMMISSIONING

Engine commissioning was performed during October of 2019. Kohler Power Systems was on-site at CSU during this time. Engine commissioning was performed without the use of the blending system to reduce complexity and facilitate troubleshooting. The fuel used for this testing and tuning was the 40°C dew point blend with a direct molar replacement of the water

content with carbon dioxide premixed in bottles. This replacement fuel would provide the same LHV and a similar mass AFR. The content of this fuel compared to the standard 40°C DP fuel can be seen in Table 6. These bottles were mixed according to Dalton's law of partial pressures, where the partial pressure Pi of a constituent gas is a fraction of the total pressure of the mixture P equal to the mole fraction of the constituent seen in Equation 8.

Table 6: 40°C DP Bend Compositions by Mole Percentage

Fuel Mix	Carbon Dioxide	Water	Hydrogen	Carbon Monoxide	Methane	LHV (MJ/kg)	Mass AFR
40°C Full Blend	53.79	2.49	33.64	9.31	0.76	4.165	1.15
40°C CO2 Replacement Blend	56.28	0.00	33.64	9.31	0.76	4.165	1.18

$$P_{Total} = \Sigma x_i * P_i \qquad (8)$$

3.4.1 INITIAL COMMISSIONING

During commissioning, the engine was able to run on the Impco mixer but for a very brief amount of time and not reliably. The fuel mixture stratified in the bottles due to density differences, which allowed the Hydrogen to be pulled off first. Allowing the engine to run with an extremely lean AFR on the Impco mixer. By placing the fuel bottle on rollers then rolling for an hour after mixing, and for 30 min directly before the bottle was used on the engine a homogenous gas mixture was ensured. Which allowed for reliable operation on bottled gas.

During commissioning with the Kohler team, it was discovered that the gas mixer supplied with the engine, an Impco CA100, was designed for use in natural gas engines and

provided a gas mixture that was to lean—causing rough running and starting difficulties. Also, the equivalence ratio control method devised for use with this mixer proved to be erratic. To solve both these problems at the same time a new method of mixing was researched.

The initial results of commissioning were not promising. By the end of the commissioning period the engine had not run for an extended period of time and continued to have difficulties starting and running. To solve this a custom mixer was developed for ATG fuel in conjunction with Eden Innovations, who have experience with developing custom gas mixers for use in duel fuel diesel engines. This venturi mixer was 3D printed from glass fiber reinforced nylon which attached to a Woodward L-series butterfly valve. Fuel is supplied to the L-Series via a high flow Madas AGP/RC zero pressure regulator. Equivalence ratio control is achieved through the actuation of the L-Series valve via the ECM. The venturi effect of the mixer body ensures a consistent equivalence ratio in response to both engine speed and load. Figure 40 shows the complete system.

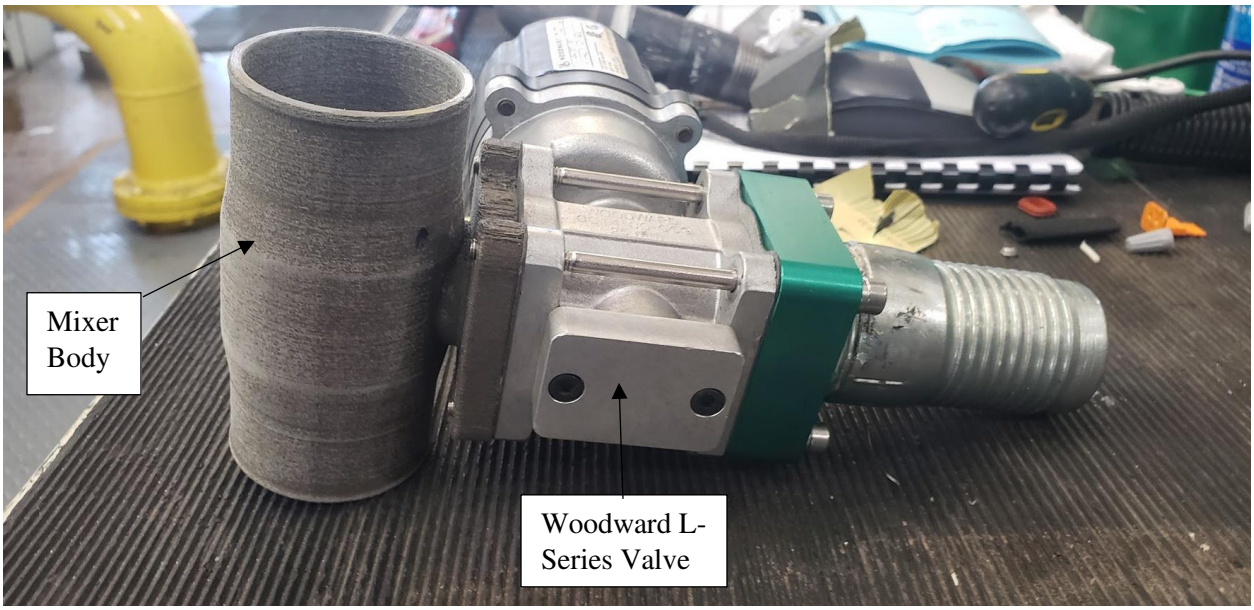

Figure 40: Eden Innovations Mixing System

During this change in mixing hardware, all upstream regulators in the fuel supply system were resized to ensure adequate flow. The original Impco zero pressure regulator was determined to have inadequate flow; the Madas zero pressure replaced this. The regulator providing the initial step down from line pressure was also undersized. A second Itron regulator was added in parallel to increase the flow rate provided to the zero pressure regulator. A standalone wideband oxygen sensor was also installed into the exhaust downstream of the turbocharger to verify the equivalence ratio.

The new mixing system tested with pre-mixed fuel bottles. Initial startups on the new system were performed by holding the L-series valve at a fixed position of 50%, and adjusting the zero pressure regulator outlet pressure via an adjustment screw. This screw would directly adjust the AFR via changing the outlet pressure. The regulator was set to a known rich position and backing the screw out after each attempt. In a rich condition, the engine would surge while the starter was cranking after the fuel was shut off. This adjustment was continued until the engine started and ran; or no longer surged, indicating a lean condition. The engine was then operated up to 1000 RPM controlled by the speed controller on the dynamometer. The L-series valve was then used to adjust the equivalence ratio to stoichiometric. These starting tests found that the engine would not start with a stoichiometric mixture; and that a lean mixture was needed, contrary to most conventional fuel engines which require a rich mixture on startup.

3.4.2 CONTROLS TUNING

The ECM was supplied with an integrated speed controller, which needed to be tuned to the engine while it was running. This controller is a PID controller with two loops, one for steady-state, and one for transient operation. These loops were tuned by entering a desired engine speed into the ECM, observing the response, and adjusting the PID parameters accordingly. This

process was done entirely on bottles while the fuel cell simulator was being built and programmed in parallel. This process took a significant amount of time due to instability in the fuel supply induced by rapid changes in engine speed, caused by the improperly tuned speed controller. To solve this problem, the desired speed was approached with a constant throttle angle. Then the speed controller was activated. This approach eliminated large transient operations. In addition, there was a third throttle controller, which controls the actual throttle position to the command position. This controller was found to be oversensitive, resulting in a discrepancy between command and actual throttle position, causing instability. These issues were solved by properly tuning this third throttle controller, after which all controllers functioned as designed.

The fuel cell simulator provides mixed gas to the engine drawn from constituent gas bottles. This system is run via a Labview program. A set of four Omega mass flow controllers are commanded by the program to mix the gases in a manifold. The mixed gases are run through a Khrone Coriolis meter, which measures a summed flow rate. The percentages are checked by dividing the omega flow rate by the total flow rate, and adjustments were made through PID loops. A problem was encountered with the constituent loops that stemmed from the hydrogen and carbon dioxide controllers. These controllers would interfere with each other. In Figure 41, the response of both controllers can be seen during steady-state operation at 2 g/s total flow.

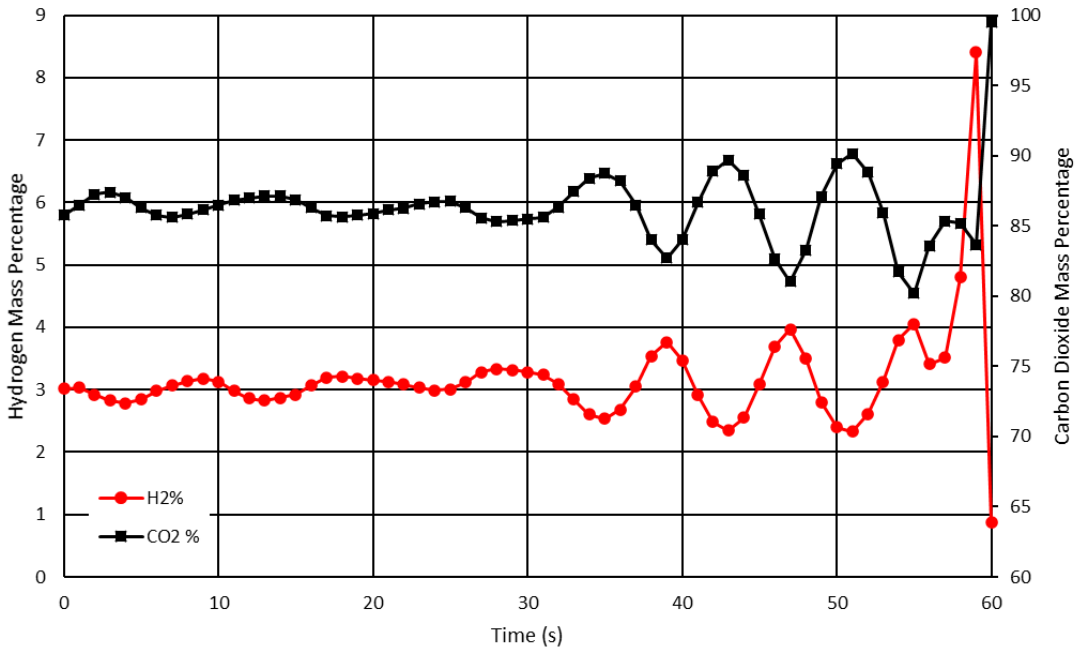

Figure 41: Hydrogen and Carbon Dioxide Response at Steady State

The controllers will destructively interfere with each other causing higher and higher disturbances until the controllers go out of bounds. This fluctuation is dangerous for running the engine on due to hydrogen having a methane number of 0. High hydrogen content caused knock and a higher propensity for backfires leading to dangerous operating conditions. This interference could not be tuned out even by dampening the response of one of the controllers to be extremely slow; eventually, the destructive interference would cause unacceptable composition. The constituent PID loops were removed, and the ratios of the gases are locked together. A single PID loop controls all four gases; the user must manually verify that gas percentages are correct. A fuel bypass valve was installed to allow for gas to bypass the engine during startup. This allows the controllers to operate outside of the bottom 10% of their control regions. The bypass valve is closed once the engine reaches speed and load, which allows full gas flow to be utilized. To increase or decrease the range of the equivalence ratio available for

control at the L-Series valve the fuel manifold pressure could be increased or decreased while the engine was running. This system ensured a stable equivalence ratio and a consistent composition.

3.5 TEST PLAN

Testing was planned to be carried out at a full design load of 14kW. Due to time constraints, the turbo simulator was not functioning during testing, so each data point was taken with the throttle fully open, and the wastegate fully closed. Once the engine reached the data point, it was allowed to run for two minutes to stabiliz. A one minute average was taken at the ignition timing GT-Power predicted the best efficiency and knock. This was repeated for four speeds between 1600 and 2200 RPM.

Table 7: GT-Power Verification Test Plan

Test Run	**Brake Power (kW)**	**Ignition Timing (°BTDC)**	**Fuel Blend**	**Engine Speed (RPM)**	**IC Exit Temperature (°C)**
1,2	Maximum attainable	GT Max Eff., and GT knock)	40°C CO2 Replacement	1600	Minimize
3,4	“	“	“	1800	“
5,6	“	“	“	2000	“
7,8	“	“	“	2200	“

CHAPTER 4: EXPERIMENTAL TESTING

The testing was carried out according to the procedure in Chapter 3. Data collection occurred at four speeds and two ignition timings for each speed. The engine produced power under all conditions tested, and knock was never encountered. The maximum power of 7.42 kW occurred at 2200 RPM and 18°BTDC timing. The maximum efficiency of 27.34% occurred at 1600 RPM and 16°BTDC timing. During the testing of 2000 RPM, the engine overheated due to a control system error. The data collected for these two points were of poor quality and have been eliminated.

4.1: BACKFIRE PROBLEMS IN DATA

Backfires, causing a loud pop and drop in engine speed and torque; were a regular occurrence during testing. These occurred at every data point collected. Backfires created inconsistencies in the data due to the reduction in engine output and speed. Thus the data had to be post processed to remove the effects of backfiring. A backfire is identified in the data set by a drop in speed and torque. Speed dropping below the set point was the start of the backfire event, and speed reaching the set point was the end of the event. All data below the rated speed has been removed from the set. Results then averaged over the remaining data points to obtain the set average. Figures 45 and 46 show the variability caused by the backfires at 1600 RPM and 16° timing. Figures 47 and 48 show the effect of removing the backfire transients from the data set. During data point collection, several sets of combustion data were taken. These sets consist of pressure data over 100 cycles. It was possible to collect a backfire free set of combustion data, so no action was necessary to remove data points.

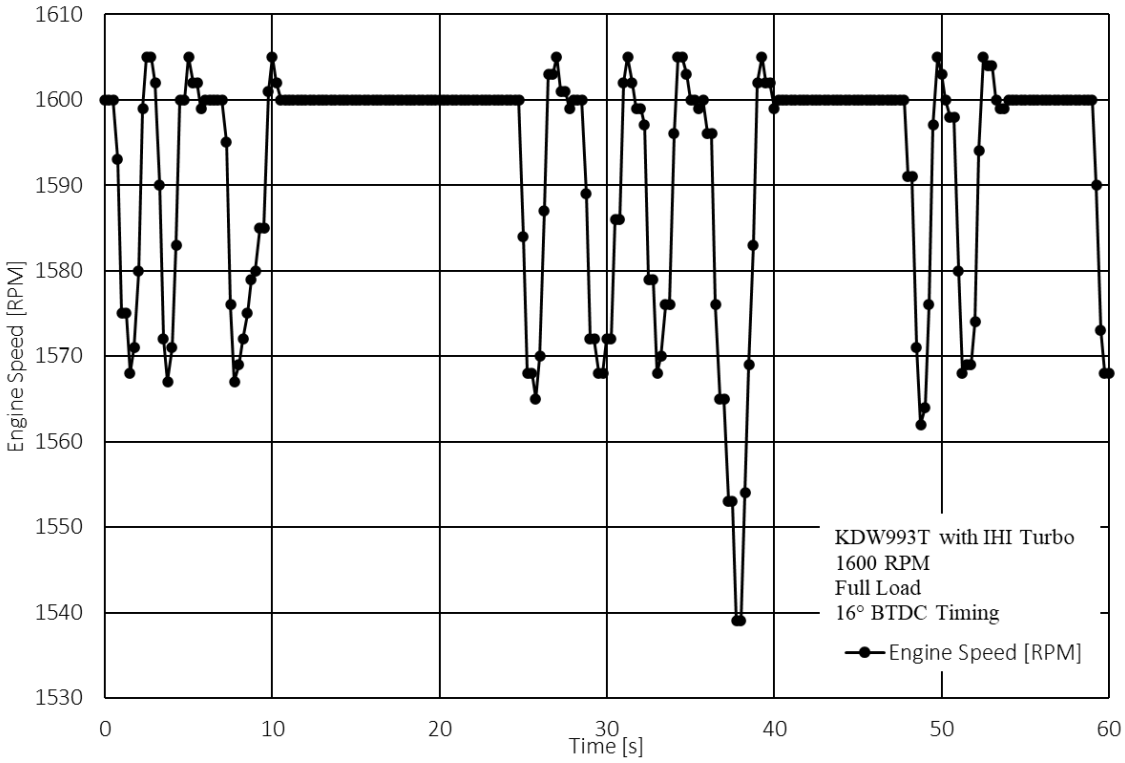

Figure 45: Engine Speed vs Time at 1600 RPM and 16° Timing

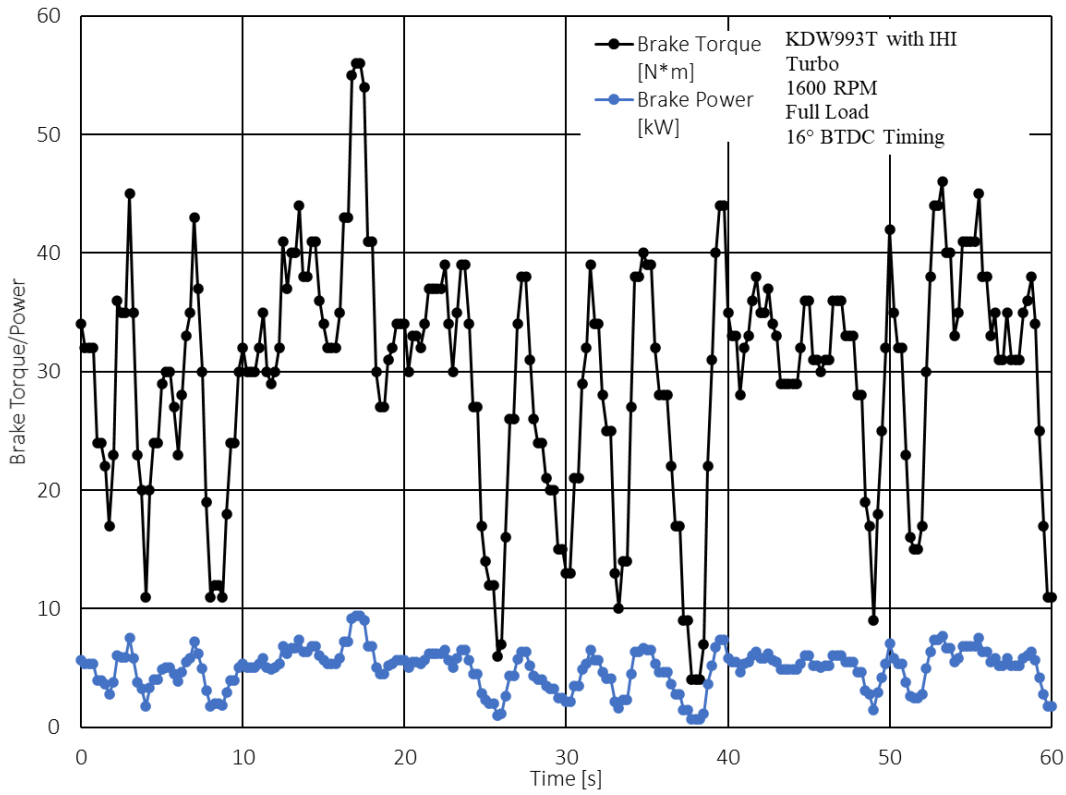

Figure 46: Brake Torque and Power Variations vs Time at 1600RPM and 16° Timing

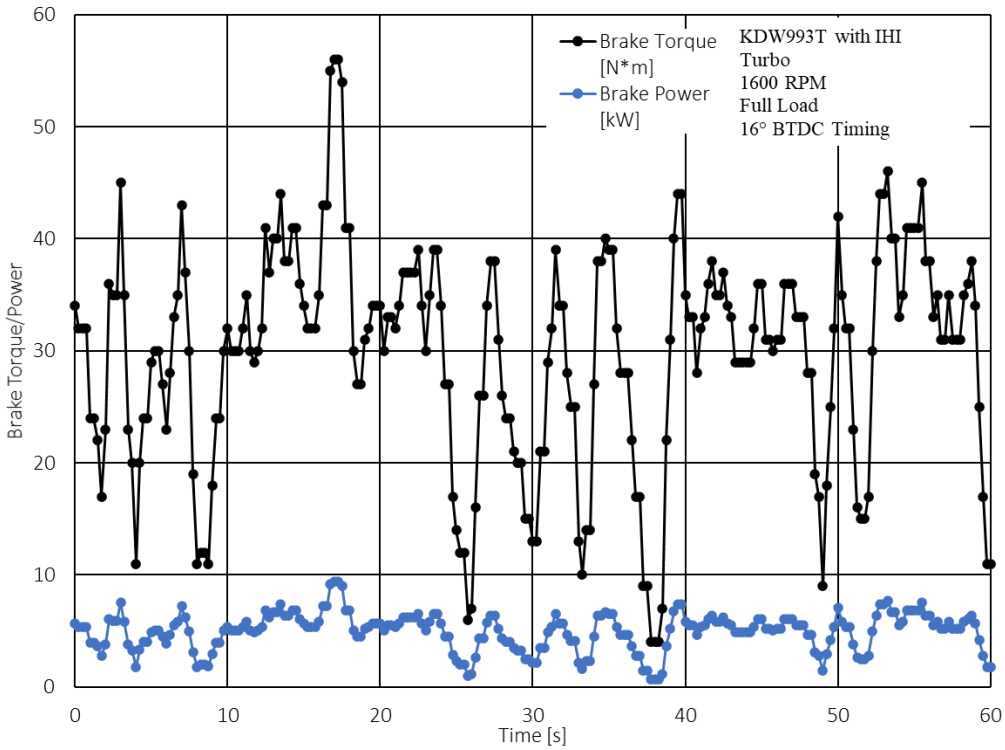

Figure 47: 1600RPM and 16°Timing with the backfires removed

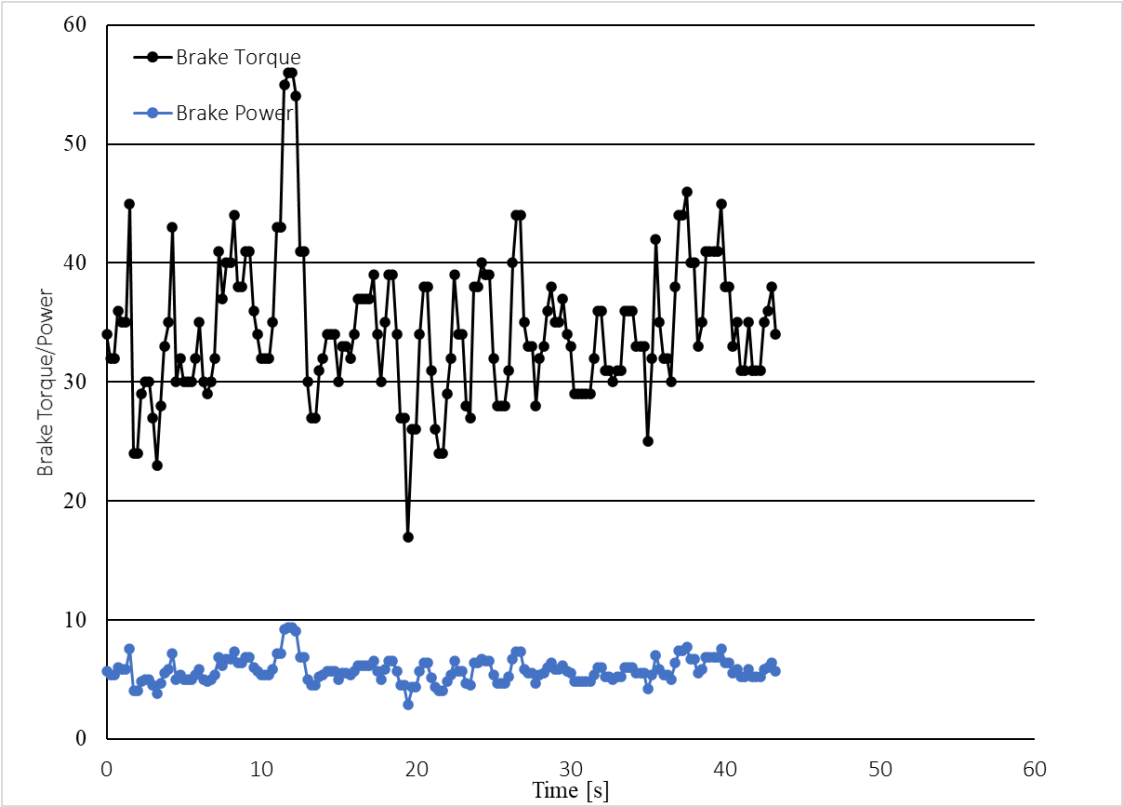

Figure 48: 1600 RPM and 16° Timing Brake Torque and Power with the Backfires Removed

Backfires did not occur during cold startups. Only after the engine had warmed up did the events occur. It was initially thought that the cause was late ignition. This late ignition causes the charge to still be burning during valve overlap, allowing the flame to propagate into the intake manifold.It is hypothesized that high exhaust port temperatures would indicate the presence of late burning fuel, due to the burning charge outside the cylinder. However, no elevated temperatures were observed. Advancing ignition timing would remedy this situation. Upon doing so, a reduction in backfires did not occur. Applying load to the engine made backfires more frequent. It is hypothesized that a hot spot is forming when torque is applied to the engine. The most likely candidate is the spark plugs, which are a platinum J gap type. Platinum is a catalyst for hydrogen combustion [20], significantly lowering the energy required for autoignition. If the spark plugs are too hot, then autoignition can occur during the intake stroke, causing a flame to propagate into the intake manifold—possible steps to solve this backfire issue include.

- Switching to copper core plugs to remove the platinum
- Using colder heat range plugs to reduce the tip temperature
- Using a surface gap style plug to remove the electrode tip and reduce the thermal mass

4.2 TIME AVERAGED DATA

The time-averaged data was smoothed according to the procedure in section 4.1. To calculate brake efficiency the fuel power input was calculated. In Equation 10, the LHV of the constituent gas was multiplied by its flow rate. Summing these quantities gives the fuel power input. The dynamometer measures torque and speed. A calculation for power is done from these quantities according to Equation 11, where torque is in N*m, and N is in RPM. The brake power is divided by the fuel power to calculate the brake efficiency as per Equation 12.

$$\dot{W}_{Fuel} = \sum \dot{m}_i * LHV_i \quad (10)$$

$$\dot{W}_{Brake} = \frac{\tau_{Brake} * N}{9548.8} \quad (11)$$

$$\eta_{Brake} = \frac{\dot{W}_{Brake}}{\dot{W}_{Fuel}} \quad (12)$$

4.2.1 BRAKE TORQUE AND POWER

Brake torque and power were allowed to float for the tests that were performed. These quantities were allowed to float due to the engine not being able to reach its design power of 14kW without the turbocharger simulator. The throttle was set to fully open, and the turbo wastegate set to closed. This allowed maximum boost production from the turbocharger. Table 8 shows the brake torque and power at all conditions tested.

Table 8: Brake Torque and Power at Test Conditions

Engine Speed [RPM]	1600	1600	1800	1800	2200	2200
Ignition Timing [°BTDC]	16	23	17	26	18	30
Brake Torque [N*m]	34.43	33.99	29.96	32.30	32.21	13.15
Brake Power [kW]	5.77	5.70	5.65	6.09	7.42	3.03

Figure 49 shows the average brake torque at all conditions tested. For 1600 and 2200 RPM, the more advanced timing produced less brake torque. This effect is most notable at 2200 RPM where there was a drastic decline in torque, indicating that the more advanced timing is well past maximum brake torque timing (MBTT). Early combustion may be the cause of this drop and will be explored further in section 4.3.3. At 1800 RPM, the more advanced timing

showed an increase in brake torque. The location of MBTT could be around this point. A maximum brake torque of 34.43 N*m occurred at 1600 RPM and 16° BTDC timing.

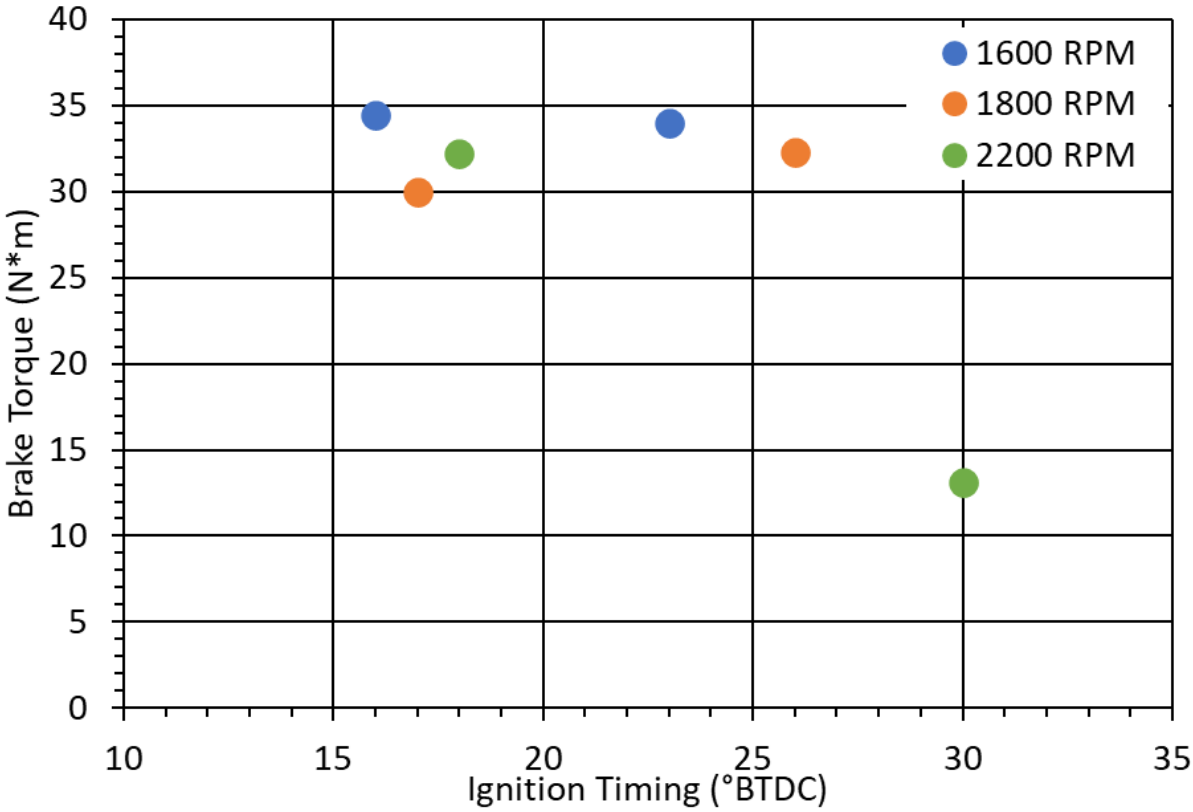

Figure 49: Brake Torque at Test Conditions

Figure 50 shows the average brake power at all test conditions. Brake power follows the same trends as brake torque due to power varying with torque while speed is constant, as shown in Equation 11. It is interesting to note that even though both timings at 1600 RPM produced more torque, the more advanced timing at 1800 RPM made more power due to the increased engine speed. A maximum brake power of 7.42 kW occurred at 2200 RPM and 18°BTDC timing.

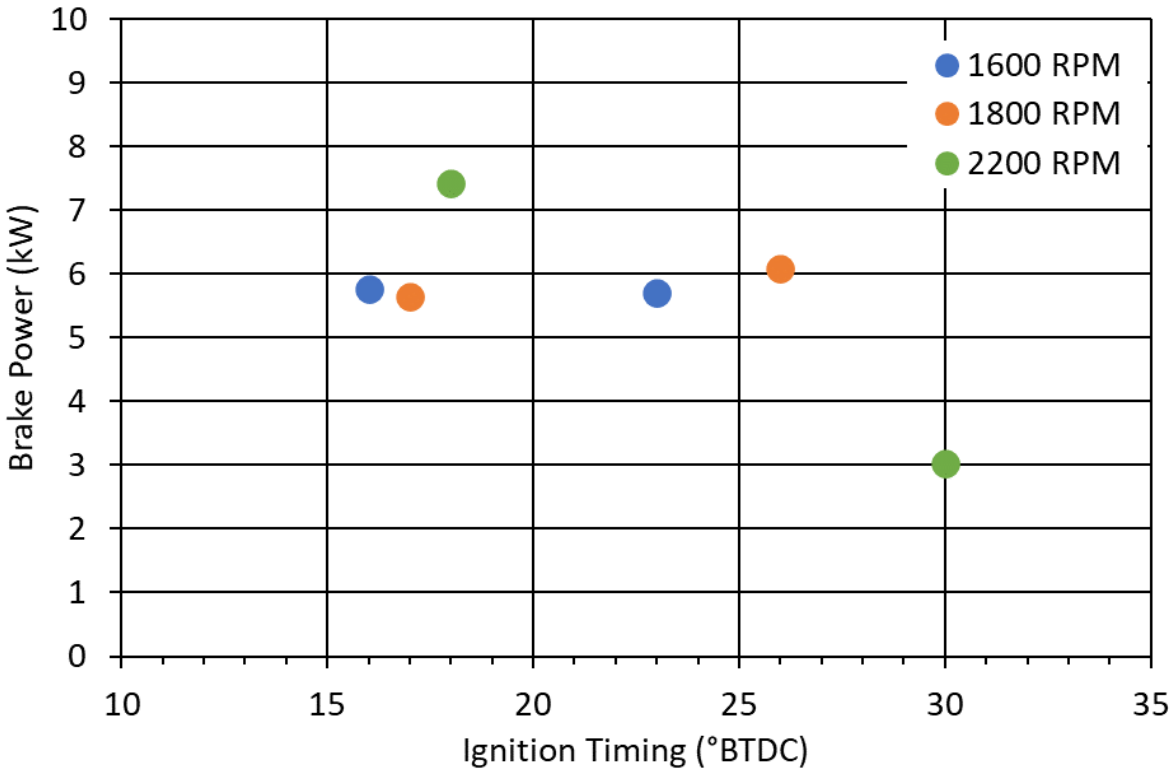

Figure 50: Brake Power at Test Conditions

4.2.2 BRAKE EFFICIENCY

Brake efficiency is the principle measurement of interest in this study. The goal was to create an engine with greater than 30% brake efficiency at 14kW. Brake efficiency is lower at part load, such as the test conditions reported above. The goal was revised to see if the GT-Power model matches the collected data. If the model matches the experimental data well, then the efficiency predictions at full load should be accurate. Table 9 shows brake efficiency at all test conditions. This data is presented both as a percentage and brake specific fuel consumption (BSFC). BSFC is calculated according to Equation 13, where fuel flow is in g/hr, and brake power is in kW.

Table 9: Brake Efficiency Measurements at Test Conditions

Engine Speed [RPM]	1600	1600	1800	1800	2200	2200
Ignition Timing [°BTDC]	16	23	17	26	18	30
Fuel Flow [g/s]	5.6162	5.6260	6.3740	6.3618	8.0719	8.5384
Brake Efficiency [%]	27.34	26.98	23.31	23.86	23.73	8.86
BSFC [g/kWh]	3614	3663	4168	3864	3985	10476

$$BSFC = \frac{\dot{m}_{fuel} * 3600}{\dot{W}_{Brake}} \qquad (13)$$

Figure 51 shows brake efficiency at all test conditions. For the advanced timings at 1600 and 2200 RPM, brake efficiency fell. This fall in efficiency indicates that the maximum brake efficiency timing (MBET) is located later than the advanced timings. The steep drop in brake efficiency at 2200 RPM coincides with the steep decline in torque and power. Fuel flow remains approximately the same as the retarded timing seen in Table 9. A maximum brake efficiency of 27.34% occurred at 1600RPM and 16°BTDC timing.

Figure 52 shows the BSFC at all conditions tested. For the advanced timings at 1600 and 2200 RPM BSFC increased. At 1800 RPM, the advanced timing decreased BSFC. Comparing the BSFC to conventional fueled (e.g., gasoline) engines, the dilute fuel has a BSFC about an order of magnitude higher. The high BSFC is due to the LHV value of the ATG fuel being an order of magnitude lower than traditional hydrocarbon fuels (4MJ/kg ATG vs. 40MJ/kg gasoline). A minimum BSFC of 3614 g/kWh occurred at 1600 RPM and 16°BTDC timing.

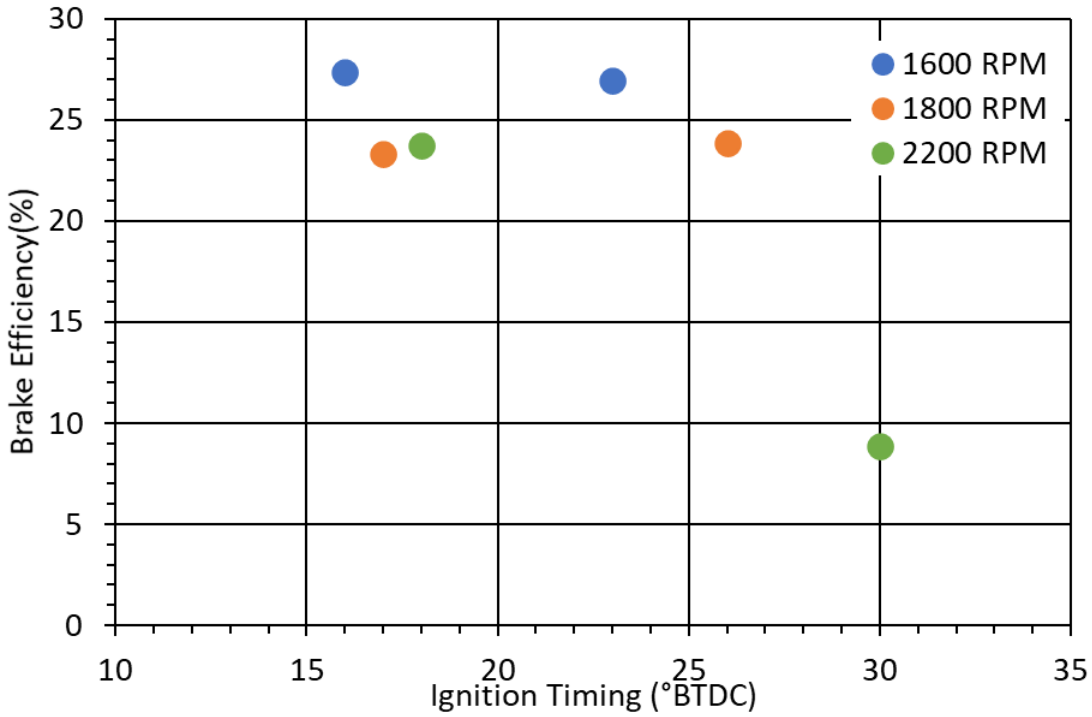

Figure 51: Brake Efficiency at Tested Conditions

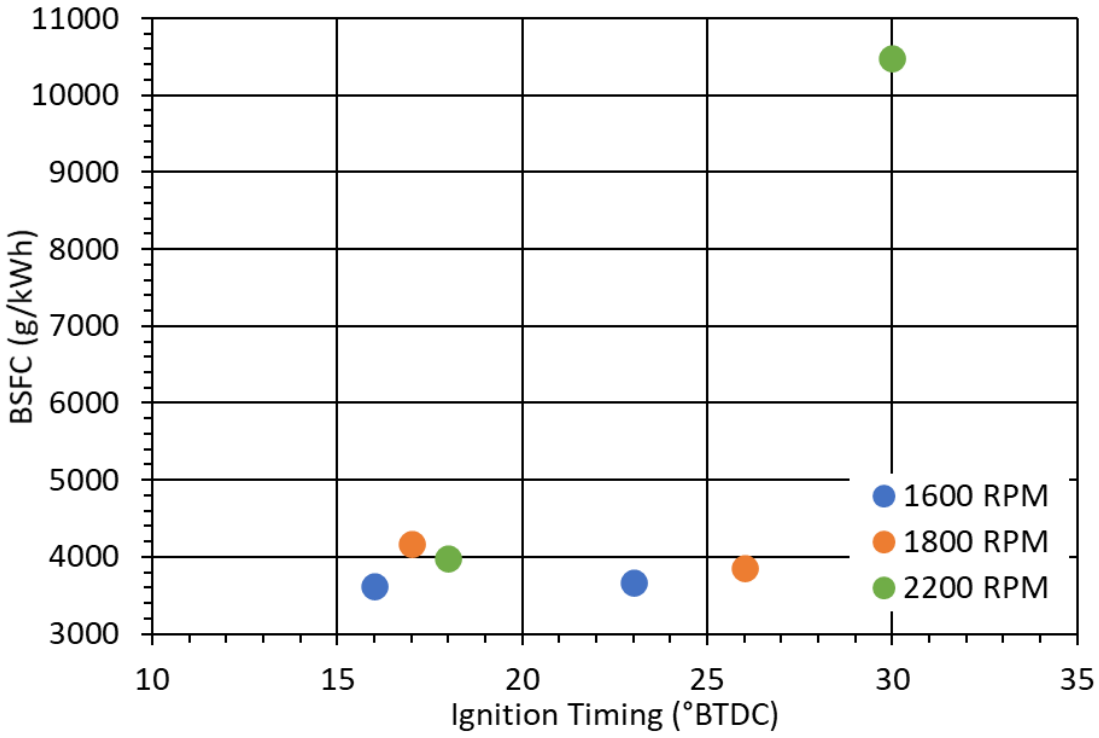

Figure 52: BSFC at Tested Conditions

4.2.3 EXHAUST EMISSIONS

Engines emissions data was collected for two engine speeds 1600 and 1800 RPM. The emissions analyzer was not available on the day the 2200 RPM data was taken. The primary indicator of combustion completeness is CO and CO2. The lower CO emissions and the higher CO2 emissions are indicative of more complete combustion. Low O2 content is an indicator of combustion completeness as well. Total hydrocarbons (THC) emissions were not available for this testing on the five-gas analyzer. Oxides of nitrogen (NOx) data were recorded from the five-gas analyzer, but no NOx was detected. An error in measurement occurred, and no data was collected. Table 10 outlines a summary of the emissions data collected from the five-gas analyzer.

Table 10: Five-Gas Emissions Data at Test Conditions

Engine Speed [RPM]	1600	1600	1800	1800
Ignition Timing [°BTDC]	16	23	17	26
Oxygen Content [%]	0.412	0.471	1.846	0.005
Carbon Dioxide Content [%]	35.6	35.5	33.5	36.2
Carbon Monoxide Content [ppm]	6046	4572	5828	4228
NOx Content [ppm]	N/V	N/V	N/V	N/V
THC Content [ppm]	N/V	N/V	N/V	N/V

Figure 53 shows CO emissions for all points tested with emissions. Advancing the timing at both speeds significantly reduced CO emissions. This effect is due to the longer time the combustion has to occur since the combustion process starts earlier in the cycle. It is interesting to note that 1800 RPM has lower emissions than 1600 RPM, even though the residence time is

shorter at higher engine speeds. A minimum of 4228 ppm occurred at 1800 RPM and 26°BTDC timing.

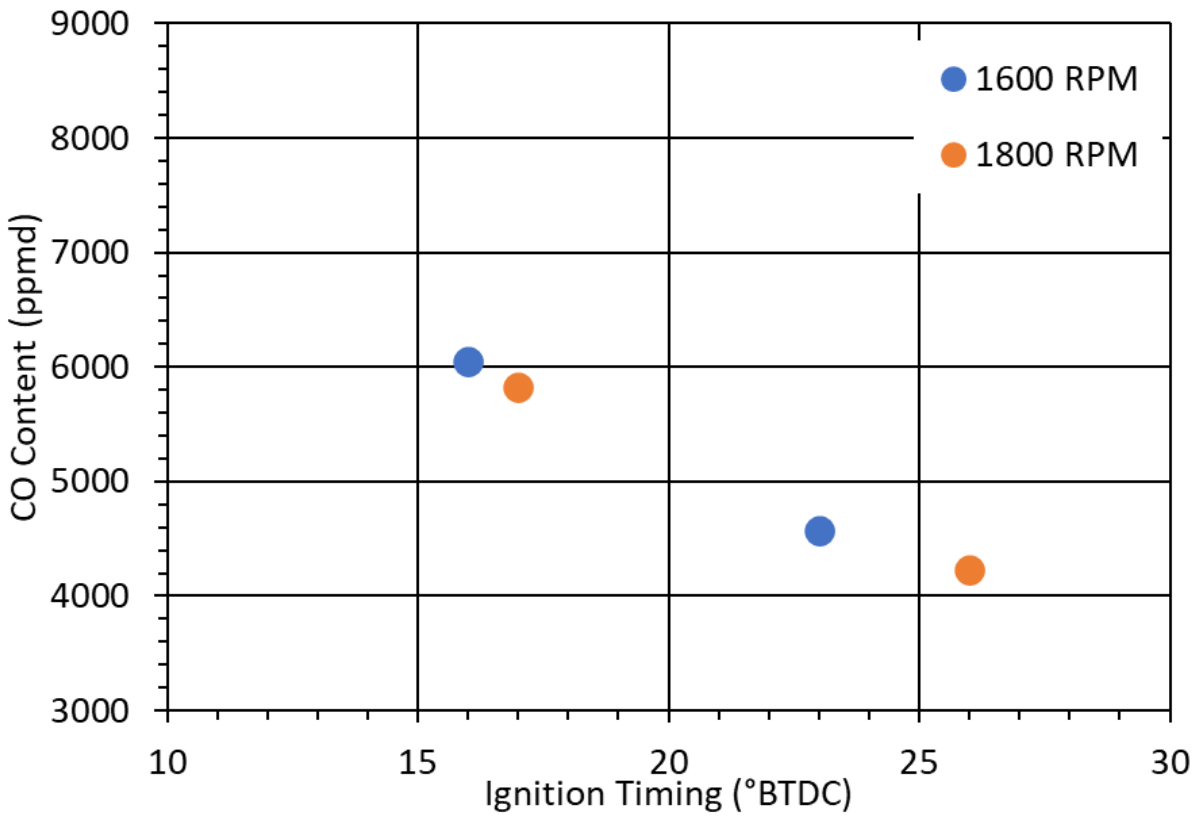

Figure 53: Carbon Monoxide Content at Tested Conditions

Figure 54 shows the carbon dioxide content for all test conditions. Carbon Dioxide is an indicator of combustion efficiency because it is the final product of the oxidation of carbon monoxide and hydrocarbons. The highest concentration of carbon dioxide occurred at 1800 RPM and 26° timing, coinciding with the lowest carbon monoxide point recorded. Other gases in the exhaust can cause carbon dioxide content to fluctuate. At 1800 RPM and 17° timing, a period of lean operation occurred. Oxygen content is higher at this point, causing CO2 content to be lower due to excess air dilution.

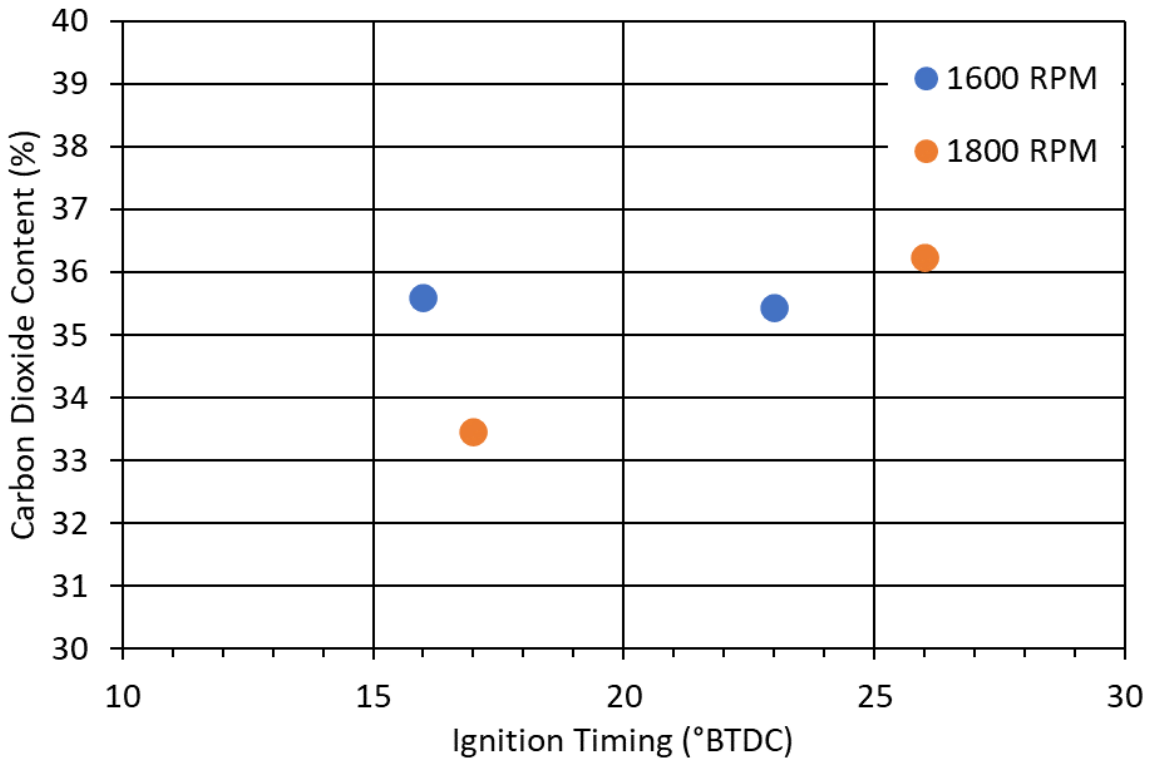

Figure 54: Carbon Dioxide Content at Tested Conditions

Figure 55 shows the oxygen content for all test conditions with emissions. Oxygen content is low for all test conditions except 1800 RPM 17°. This is due to a fuel pressure transient occurring during operation, causing the engine to run lean for approximately 15s, disrupting the data point. It is interesting to note that even though there was significant excess oxygen at this point, CO emissions remained relatively equal with 1600 RPM 16°. A possible cause of this could be the lean mixture having a slower flame speed, causing incomplete combustion. There is also still significant CO content at all other data points except 1800 RPM 26°, even though oxygen is still available. The minimum oxygen content of 0% occurred at 1800 RPM and 26°, coinciding with maximum CO2, and minimum CO, indicating complete combustion.

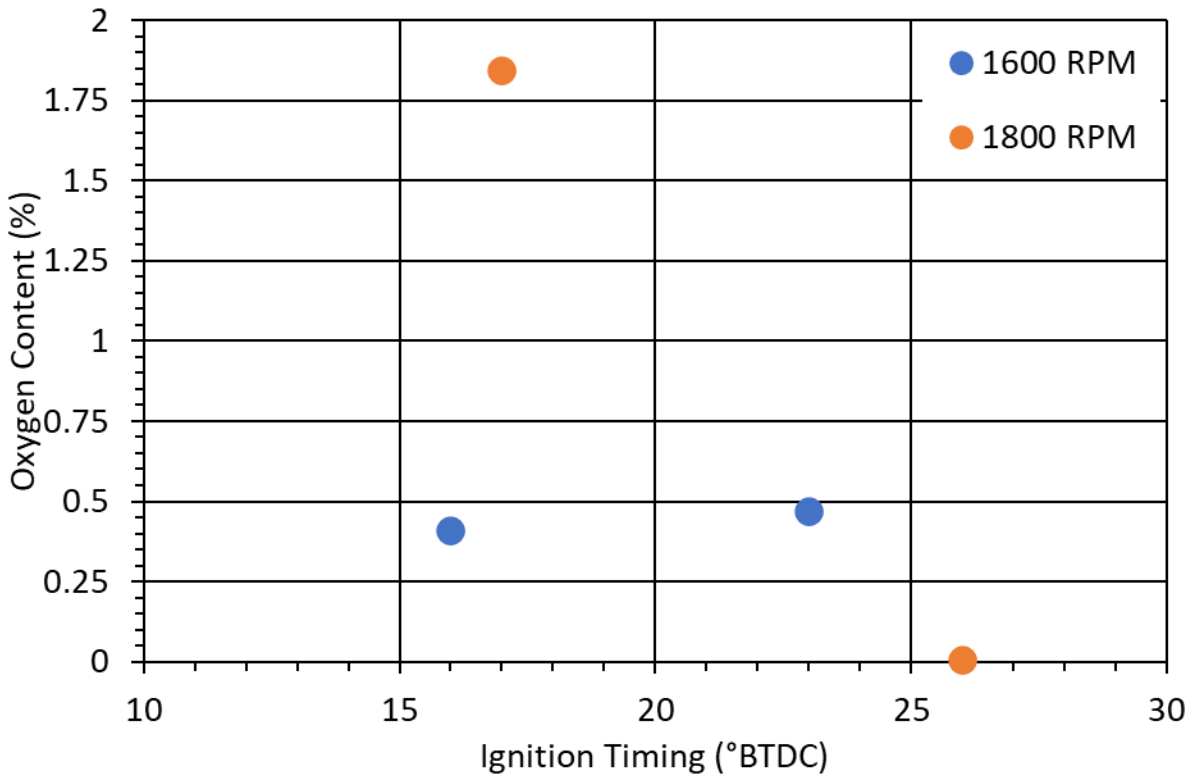

Figure 55: Oxygen Content at Tested Conditions

The exhaust gas analysis included Fourier-transform infrared spectroscopy (FTIR) alongside the five-gas analyzer. The data from the FTIR is post-processed into brake-specific emissions (BSE). BSE is the industry method for standardizing emissions, represented as g/bkW-hr. The three brake-specific emissions of interest are total hydrocarbons (THC), carbon monoxide, and oxides of nitrogen (NOx). The raw ppm measurement from the FTIR is converted to a mass flow value, which can then be normalized by the brake power output of the engine. Table 11 outlines the brake-specific emissions of the engine at the test conditions.

Table 11: FTIR Brake Specific Emissions at Test Conditions

Engine Speed [RPM]	1600	1600	1800	1800
Ignition Timing [°BTDC]	16	23	17	26
Brake Specific THC [g/bkW-hr]	0.53	0.56	0.67	0.39
Brake Specific Carbon Monoxide [g/bkW-hr]	45.56	65.10	51.69	41.36
Brake Specific NOx [g/bkW-hr]	6.88	6.83	11.00	8.70

Figure 56 shows the brake specific total hydrocarbons for the test conditions. THC emissions are low, due to the fuel containing a minimal amount of hydrocarbons. The lean case at 1800 RPM and 17° had the highest BSTHC at 0.67 g/bkW-hr, even though there was sufficient excess oxygen to react with the methane in the fuel. This effect may be due to a reduction in combustion efficiency due to a drop in flame speed at lean conditions. A minimum BSTHC of 0.39 g/bkW-hr occurred at 1800 RPM and 26° BTDC timing, coinciding with minimum O2, CO, and maximum CO2. Further supporting that relatively complete combustion occurs at this point.

Figure 57 shows brake specific carbon monoxide (BSCO). Lower BSCO indicates a higher combustion efficiency as CO oxidizes to CO2. It is interesting to note that the lean case of 1800 RPM 17° had a higher BSCO than the stoichiometric case at 1800 RPM and 26°. Peak BSCO of 65.10 g/bkW-hr occurred at 1600 RPM and 23°. Minimum BSCO of 41.36 g/bkW-hr occurred at 1800 RPM and 26°. The legal limits for this engine class for BSCO emissions are 610 g/bkW-hr [21]. The engine is well below that limit at all test conditions without the use of a catalytic converter.

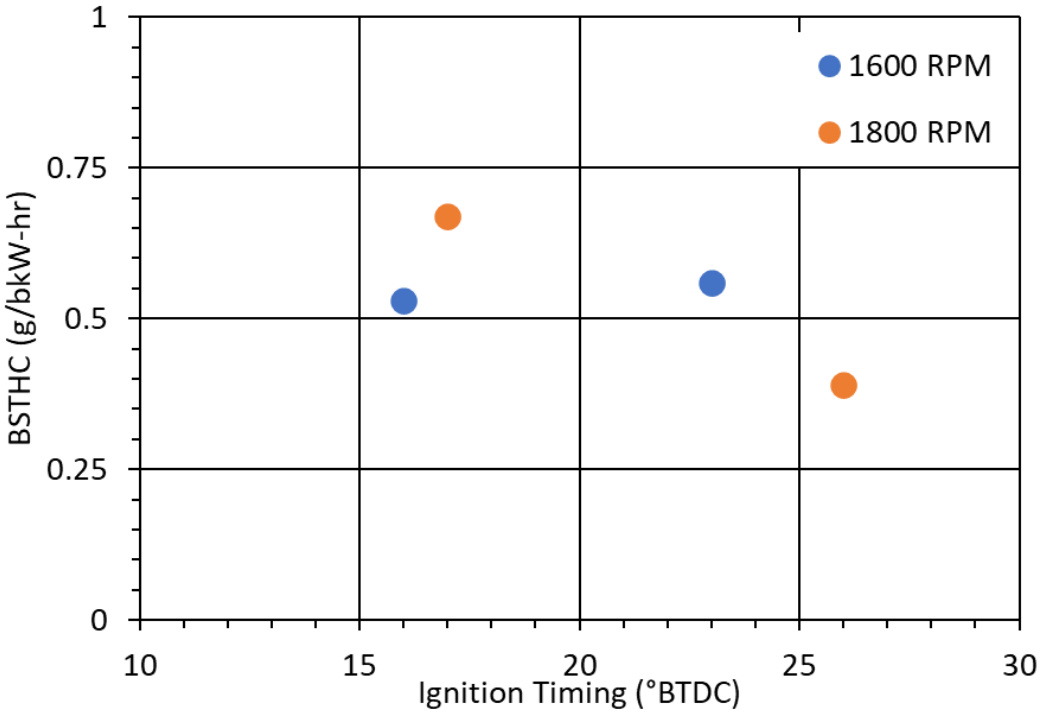

Figure 56: Brake Specific Total Hydrocarbons at Test Conditions

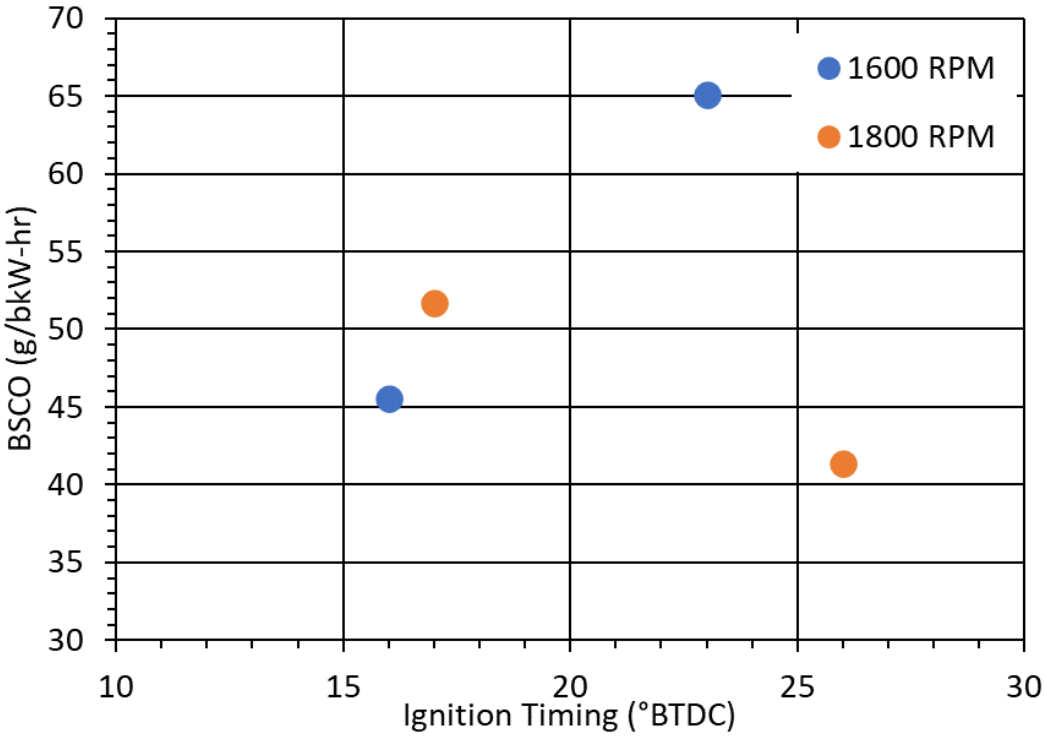

Figure 57: Brake Specific Carbon Monoxide at Test Conditions

Figure 58 shows the brake specific NOx emissions at test conditions. NOx emissions are low for an engine with a diesel-like compression ratio. This effect is most likely due to low combustion temperatures associated with high CO2 diluent in the fuel inhibiting NOx formation. A spike in BSNOx occurs at 1800 RPM and 17°. This is due to the lean operation of the engine over that data point, allowing excess oxygen to form NOx. The legal limit for BSNOx+BSTHC emissions for an engine of this size is 8 g/bkW-hr [21]. The engine is close to this goal without the use of a catalytic converter. These numbers are for half load. It is anticipated that BSNOx will rise with an increase in load due to increased combustion temperatures causing more NOx formation. A minimum BSNOx of 6.83 g/bkW-hr was found at 1600 RPM and 23°BTDC timing.

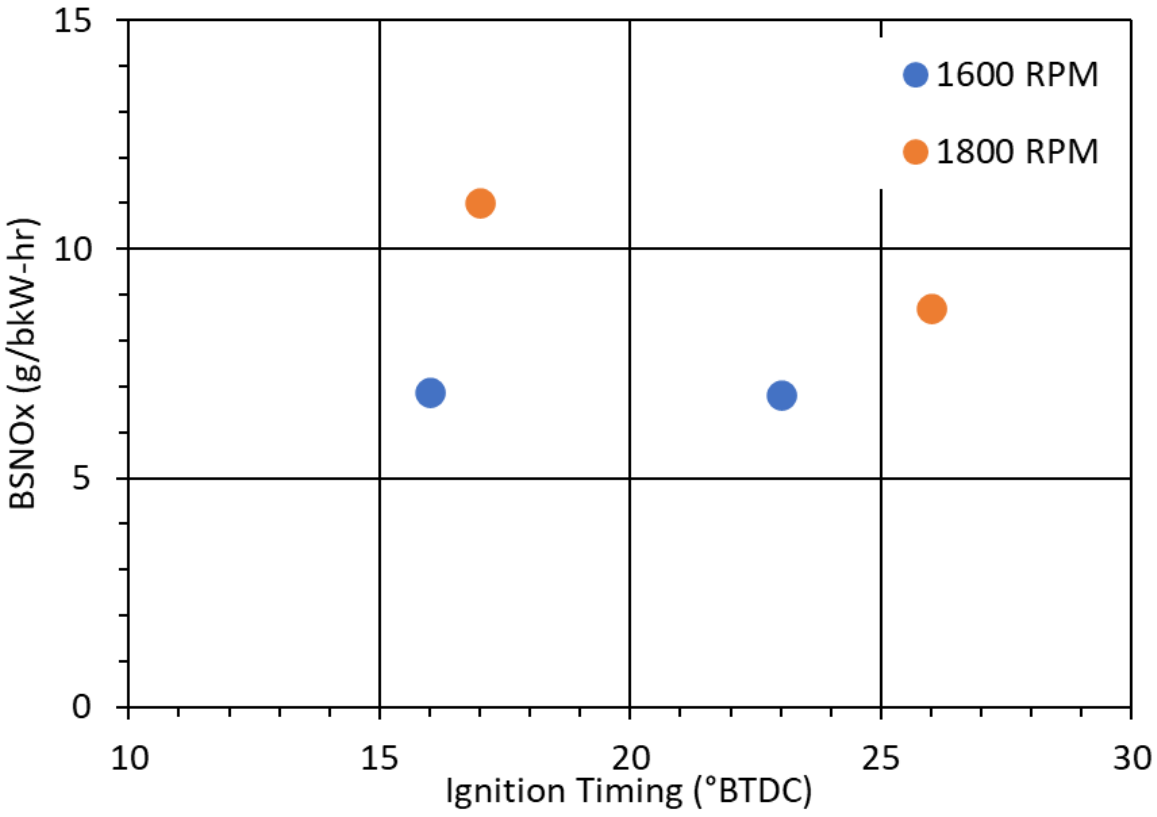

Figure 58: Brake Specific NOx at Test Conditions

4.2.4 TURBOCHARGER PERFORMANCE

The turbocharger is a critical part of making sufficient power with ATG fuel. The compressor and turbine pressure ratio can be used to evaluate the operating condition of the turbocharger. Throughout testing, the wastegate was fully closed, allowing maximum flow through the turbine, however, the turbocharger underperformed from what GT-Power predicted. As a result, the engine never reached the full load of 14kW. The atmospheric pressure at the test location is approximately 84 kPa. Using the turbocharger simulator in the future to provide sea level pressure air to the compressor will raise the power of the engine. But likely not enough to increase the power level to 14kW. Table 12 outlines the operating conditions of the turbocharger at all test points. A maximum compressor pressure ratio (PR) of 1.229 occurred at 2200 RPM and 30° timing, coinciding with maximum turbine PR of 1.415. Turbine performance is likely the limiting factor as the turbocharger continues to produce more boost as engine speed increases, and the exhaust flow rate increases.

Table 12: Turbocharger Parameters at Tested Conditions

Engine Speed [RPM]	1600	1600	1800	1800	2200	2200
Ignition Timing [°BTDC]	16	23	17	26	18	30
Compressor Pressure Ratio	1.080	1.076	1.072	1.114	1.174	1.229
Intake Manifold Pressure [Bar]	0.918	0.915	0.911	0.947	0.998	1.045
Intake Manifold Temperature [°C]	52.8	50.7	43.6	41.0	55.6	60.2
Turbine Pressure Ratio	1.245	1.213	1.248	1.294	1.395	1.415
Exhaust Manifold Pressure [Bar]	1.023	0.995	1.031	1.064	1.158	1.173
Exhaust Manifold Temperature [°C]	382.2	396.7	369.9	440.9	431.6	473.1

Figure 59 shows the intake manifold absolute pressure (MAP) for all test conditions. Advancing the timing had little effect on the MAP. Increasing the engine speed did raise the MAP significantly. This effect is because the turbocharger was operating at low flow conditions. By raising the engine speed, the mass flow rate through the turbine increases, and a higher compressor performance is achieved. This relationship is explored further in Figure 63. Maximum boost pressure of 1.045 Bar occurred at 2200 RPM and 30°BTDC timing. Figure 60 shows the pressure ratio across the compressor, which determines where in the compressor map the compressor is operating. At the low flow conditions that testing occurred at the compressor was working in a very inefficient region of the map.

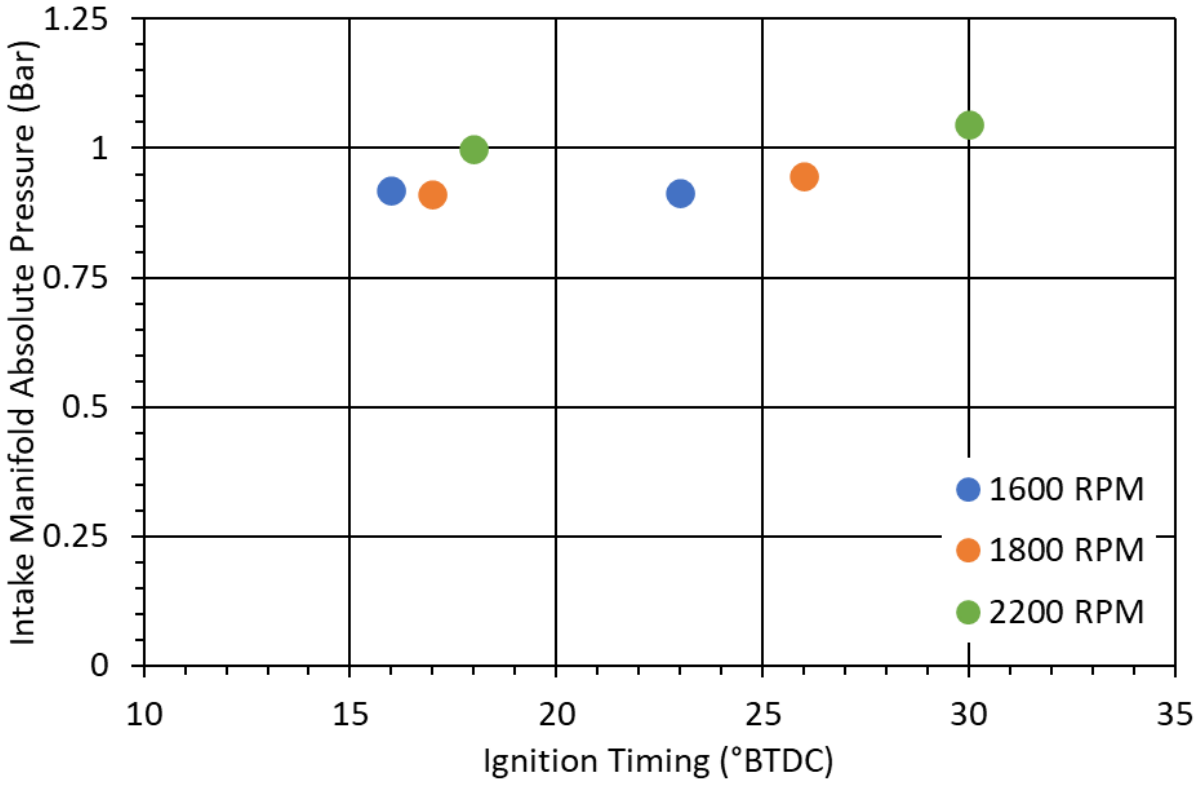

Figure 59: Intake Manifold Pressure at Tested Conditions

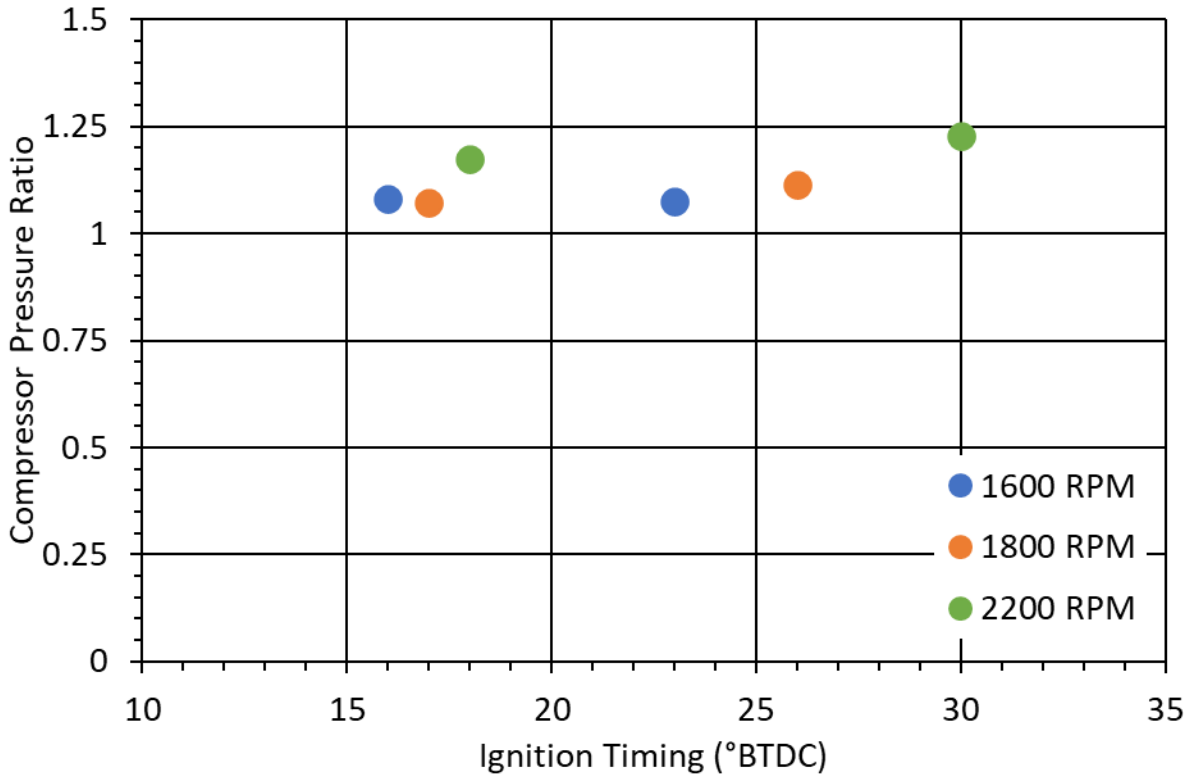

Figure 60: Compressor Pressure Ratio at Tested Conditions

Figure 61 shows the intake manifold temperature at all tested conditions. Intake manifold temperature (IMT) varied a lot with speed, and somewhat with ignition timing. At 1600 and 1800 RPM advancing the ignition timing reduced the IMT. While At 2200 RPM advancing the ignition timing increased the IMT. A minimum intake temperature of 41.0°C occurred at 1800 RPM and 26° timing, while maximum intake temperature of 60.2°C occurred at 2200 RPM and 30°timing. Minimum IMT occurs at low engine speeds because the cooling power of the intercooler is constant. Cooling potential ideally occurs according to Equation 14. So as mass flow increases, delta T decreases.

$$\dot{W}_{cooling} = C_p \dot{m}_{mix}(T_o - T_i) \qquad (14)$$

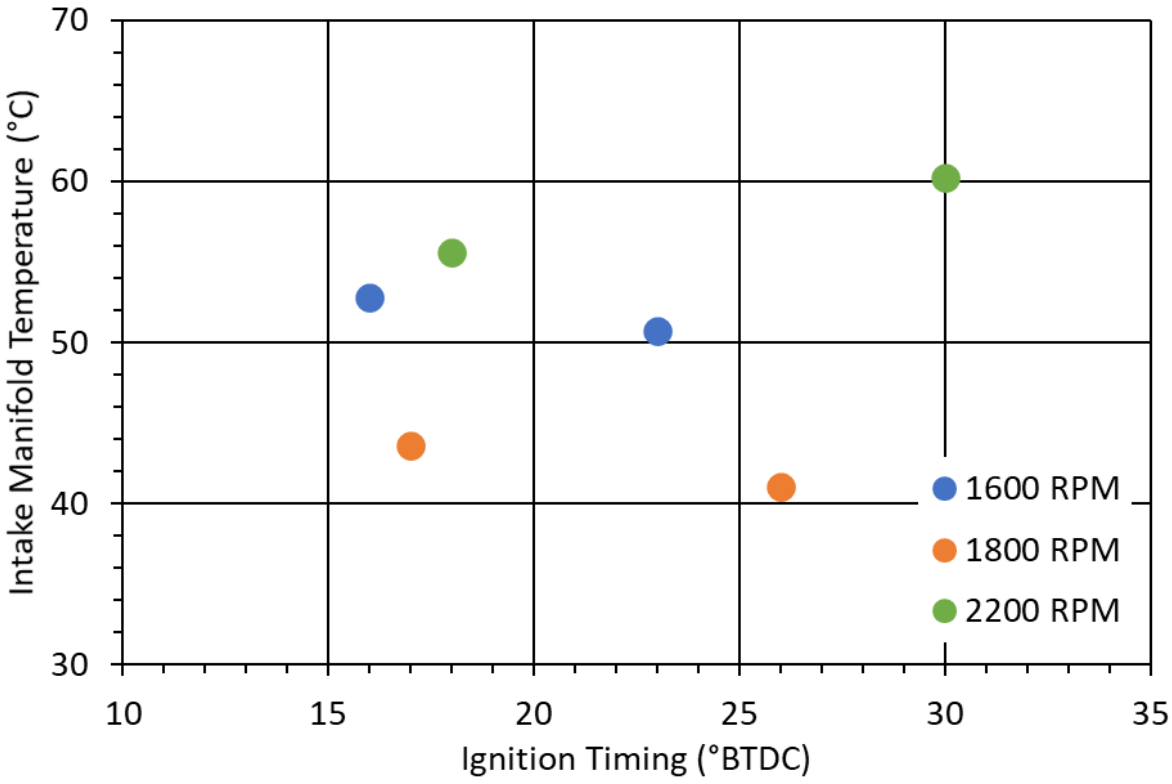

Figure 61: Intake Manifold Temperature at Tested Conditions

The maximum boost provided by the compressor is determined by how much power the turbine can provide. This is a function of the change in pressure and temperature of the exhaust across the turbine. Figure 63 shows the pressure ratio across the turbine for all test conditions, and Figure 62 shows the exhaust manifold absolute pressure. The ignition timing does not affect either of these parameters much. But increasing the engine speed had a significant effect on the turbine pressure ratio. The increased mass flow rate from higher speeds increases the turbine speed. Thus, allowing the compressor to operate at higher speeds and pressure ratios.

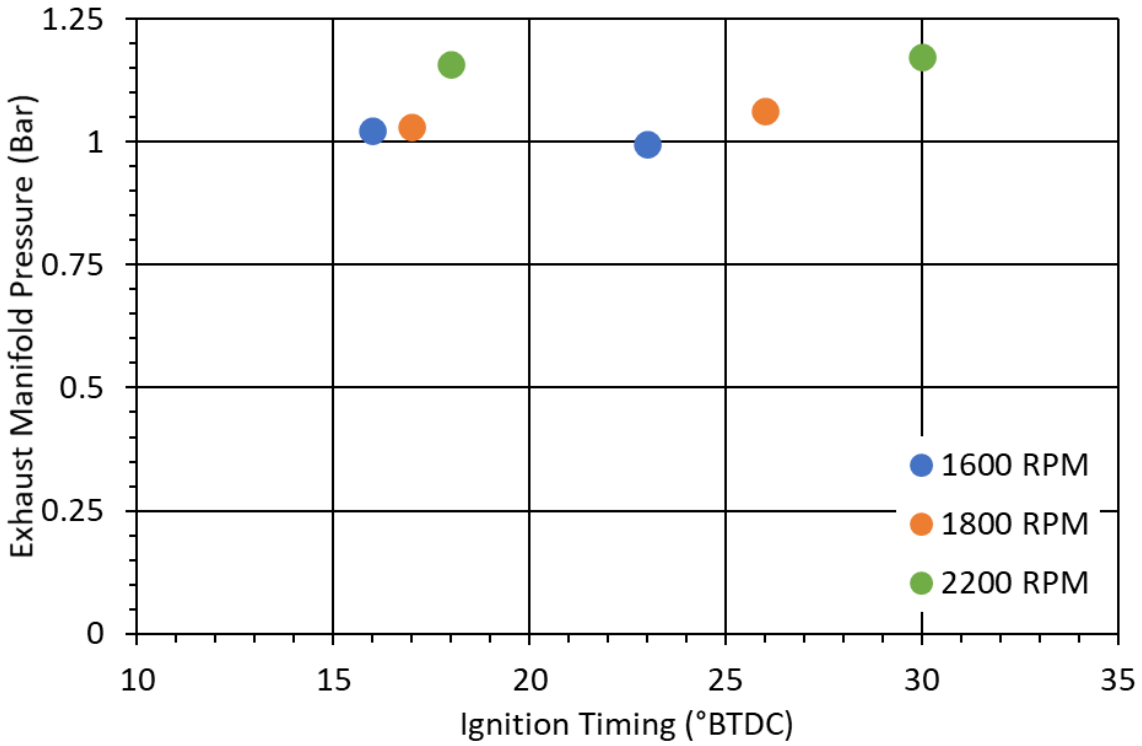

Figure 62: Exhaust Manifold Pressure at Tested Conditions

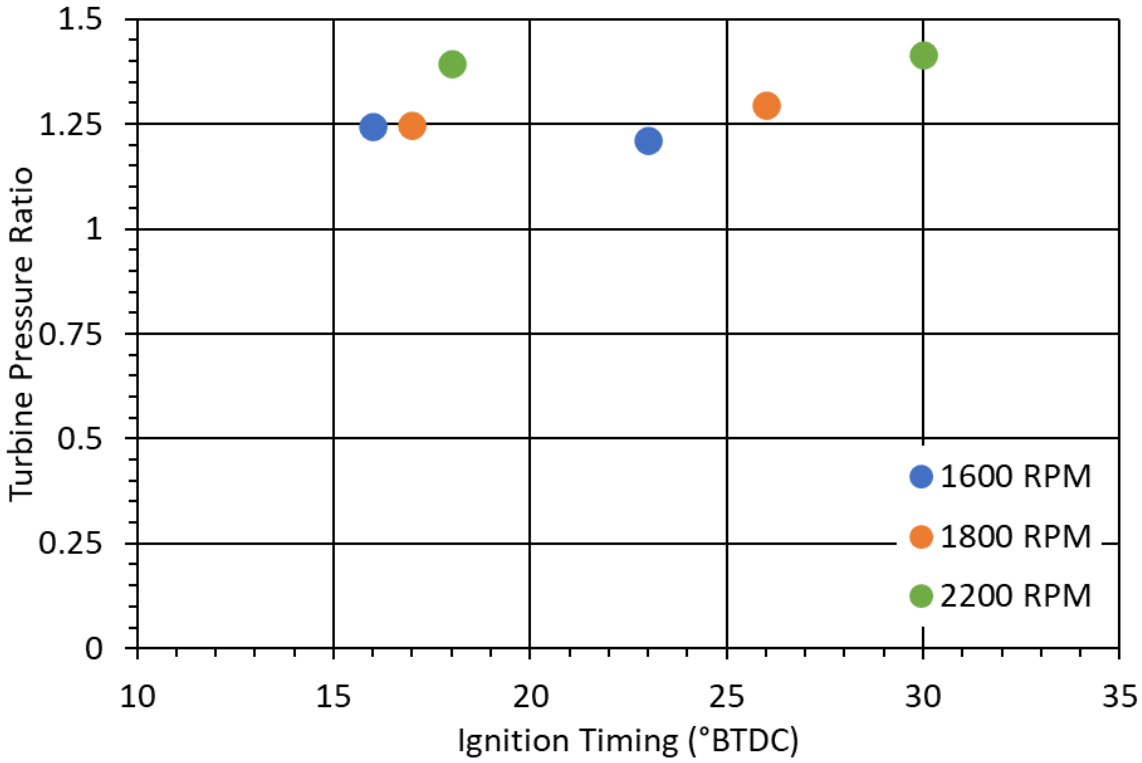

Figure 63: Turbine Pressure Ratio at Tested Conditions

Figure 64 shows the exhaust gas temperature at all test conditions (EGT). Exhaust temperature generally rose with increasing engine speed. A maximum EGT of 473.1°C occurred at 2200 RPM and 30° timing. This was the least efficient speed and indicates that a significant amount of energy that was available for expansion work is wasted as heat going out the exhaust. Minimum EGT of 369.9°C occurred at 1800 RPM and 17° timing.

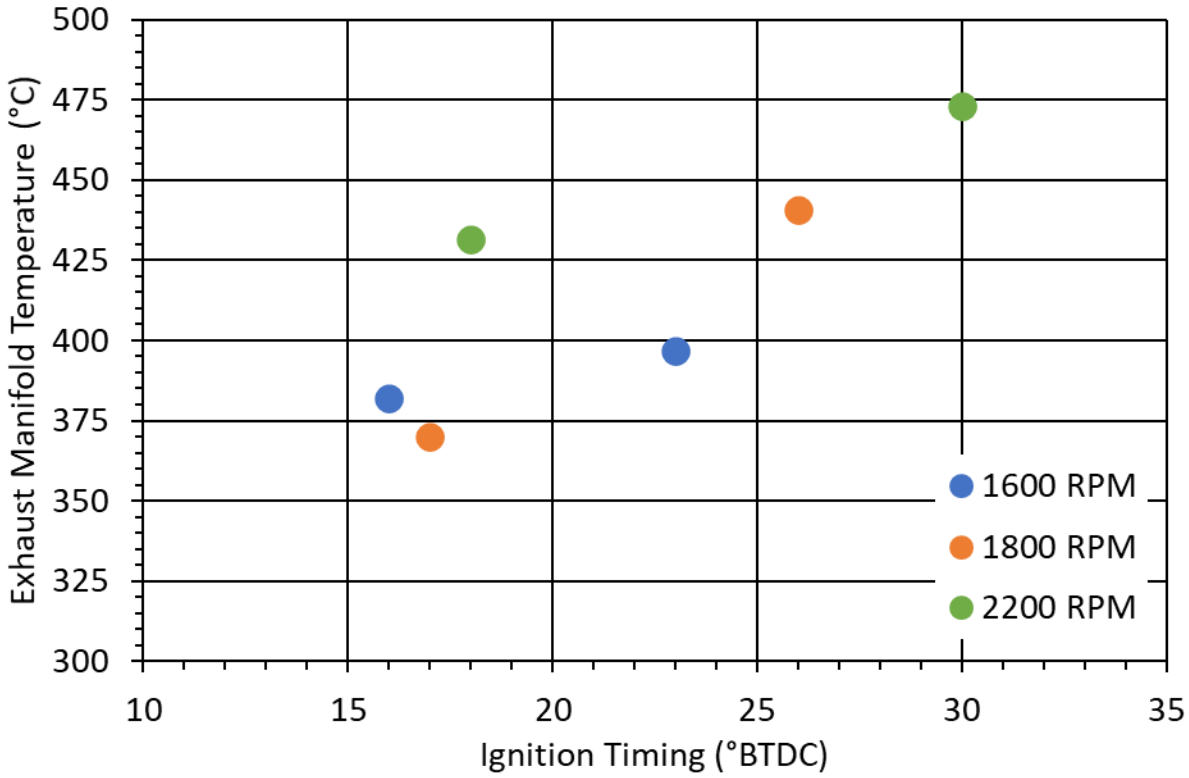

Figure 64: Exhaust Manifold Temperature at Tested Conditions

4.3 COMBUSTION DATA

Combustion data was gathered with the Powerhouse combustion analyzer cart. The raw data was post-processed with the cart to produce values for cylinder pressure, indicated mean effective pressure, and heat release. It was found during data analysis that the heat release calculations have an extreme amount of noise, and show abnormalities. This is explored further

in section 4.3.3. The pressure trace graphs show pressure averaged over 100 cycles for the entire cycle. The x-axis is in crank angle degrees (CAD). 0° is TDC firing, 0-180° is expansion, 180°-360° is exhaust, -360°—180° is intake, and -180°-0° is compression.

4.3.1 CYLINDER PRESSURE

Cylinder pressures were recorded for every data point collected. Since the data point is 100 cycles, long several were taken during the one-minute average. At least one of these was free of backfires for every data point. The CSU combustion analyzer post-processes the data collected from the cylinder pressure transducer and calculates combustion statistics. These statistics are indicators of combustion quality and stability. Tables 13-18 show the data collected for each test condition; Figures 65-70 show the average pressure trace for the 100-cycle data point.

Table 13: Cylinder Pressure Data at 1600 RPM and 16°BTDC Timing

Parameter	Cylinder 1	Cylinder 2	Cylinder 3	Average
Average Peak Pressure [Bar]	61.14	58.17	60.41	59.90
Max Peak Pressure [Bar]	62.15	59.14	61.45	60.91
Min Peak Pressure [Bar]	58.40	56.54	58.58	57.84
Peak Pressure Standard Deviation	0.542	0.506	0.472	0.507
Peak Pressure COV	0.887	0.869	0.782	0.846
Average Peak Pressure Location [°ATDC]	0.924	1.016	0.792	0.911
Peak Location Standard Deviation	0.325	0.406	0.352	0.361
Peak Location COV	35.22	39.95	44.42	39.86

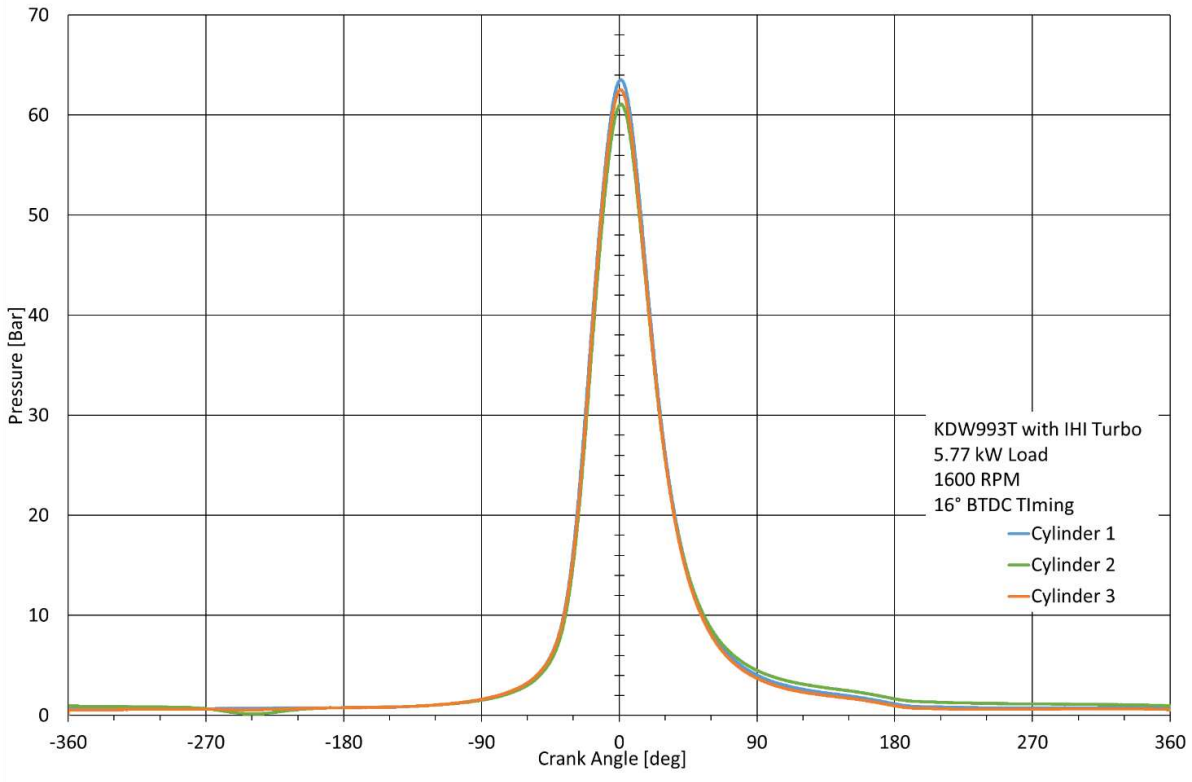

Figure 65: Average Cylinder Pressure Curves for 1600RPM and 16°BTDC Timing

Table 14: Cylinder Pressure Data at 1600 RPM and 23°BTDC Timing

Parameter	Cylinder 1	Cylinder 2	Cylinder 3	Average
Average Peak Pressure [Bar]	61.64	58.83	60.64	60.37
Max Peak Pressure [Bar]	62.40	59.68	61.53	61.21
Min Peak Pressure [Bar]	59.87	57.43	58.95	58.75
Peak Pressure Standard Deviation	0.476	0.448	0.532	0.485
Peak Pressure COV	0.772	0.761	0.878	0.804
Average Peak Pressure Location [°ATDC]	1.047	0.980	0.769	0.932
Peak Location Standard Deviation	0.374	0.324	0.383	0.361
Peak Location COV	35.72	33.10	49.82	39.55

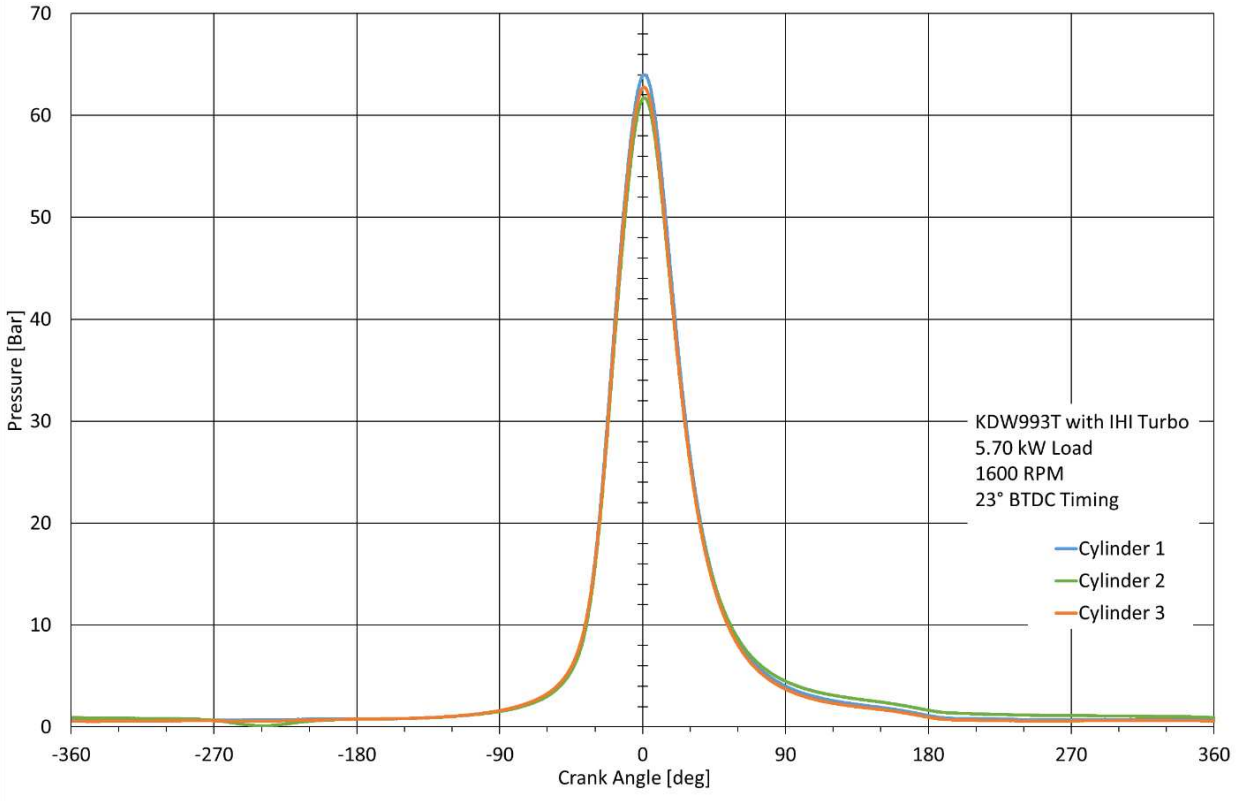

Figure 66: Average Cylinder Pressure Curves for 1600RPM and 23°BTDC Timing

Table 15: Cylinder Pressure Data at 1800 RPM and 17°BTDC Timing

Parameter	Cylinder 1	Cylinder 2	Cylinder 3	Average
Average Peak Pressure [Bar]	61.23	59.93	60.65	60.60
Max Peak Pressure [Bar]	62.47	60.93	61.41	61.60
Min Peak Pressure [Bar]	59.13	58.33	59.07	58.84
Peak Pressure Standard Deviation	0.695	0.529	0.557	0.594
Peak Pressure COV	1.135	0.883	0.918	0.979
Average Peak Pressure Location [°ATDC]	0.942	0.954	0.777	0.891
Peak Location Standard Deviation	0.360	0.327	0.365	0.351
Peak Location COV	38.24	34.31	49.92	40.82

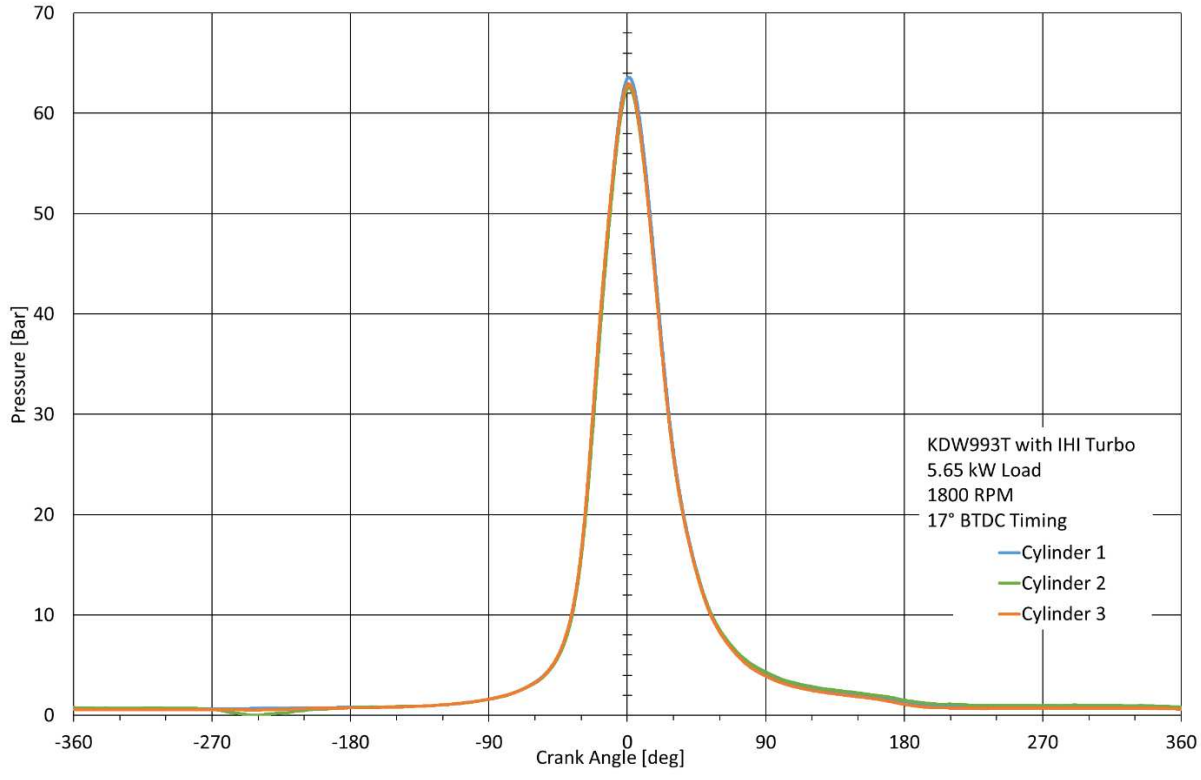

Figure 67: Average Cylinder Pressure Curves for 1800RPM and 17°BTDC Timing

Table 16: Cylinder Pressure Data at 1800 RPM and 26°BTDC Timing

Parameter	Cylinder 1	Cylinder 2	Cylinder 3	Average
Average Peak Pressure [Bar]	61.67	60.91	61.35	61.31
Max Peak Pressure [Bar]	62.57	61.56	62.01	62.05
Min Peak Pressure [Bar]	60.55	59.91	59.12	59.86
Peak Pressure Standard Deviation	0.419	0.340	0.465	0.408
Peak Pressure COV	0.679	0.559	0.758	0.665
Average Peak Pressure Location [°ATDC]	1.015	0.837	1.197	1.016
Peak Location Standard Deviation	0.302	0.311	0.350	0.321
Peak Location COV	29.72	37.15	29.27	32.05

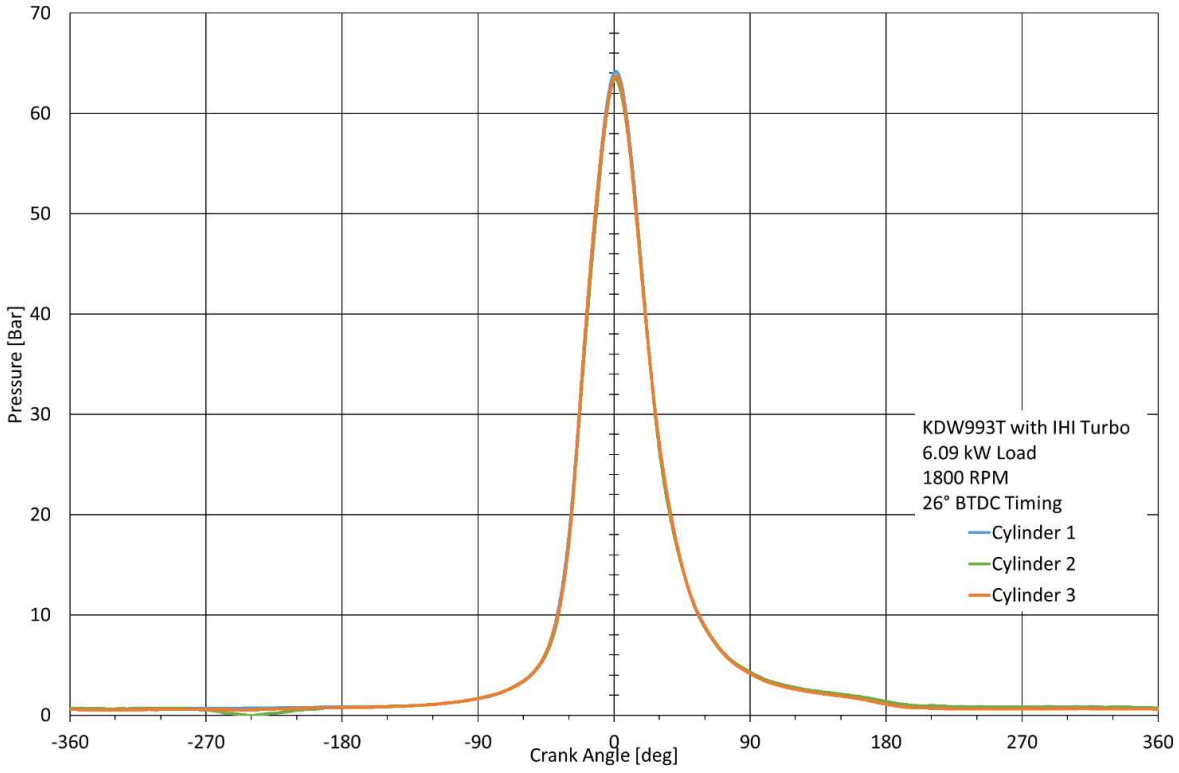

Figure 68: Average Cylinder Pressure Curves for 1800RPM and 26°BTDC Timing

Table 17: Cylinder Pressure Data at 2200 RPM and 18°BTDC Timing

Parameter	Cylinder 1	Cylinder 2	Cylinder 3	Average
Average Peak Pressure [Bar]	70.71	67.13	68.56	68.80
Max Peak Pressure [Bar]	71.16	68.40	69.62	69.73
Min Peak Pressure [Bar]	68.18	64.23	65.34	65.92
Peak Pressure Standard Deviation	0.541	0.746	0.692	0.660
Peak Pressure COV	0.772	1.111	1.009	0.964
Average Peak Pressure Location [°ATDC]	1.171	1.367	0.376	0.971
Peak Location Standard Deviation	0.358	0.376	0.366	0.366
Peak Location COV	30.54	27.53	26.09	29.03

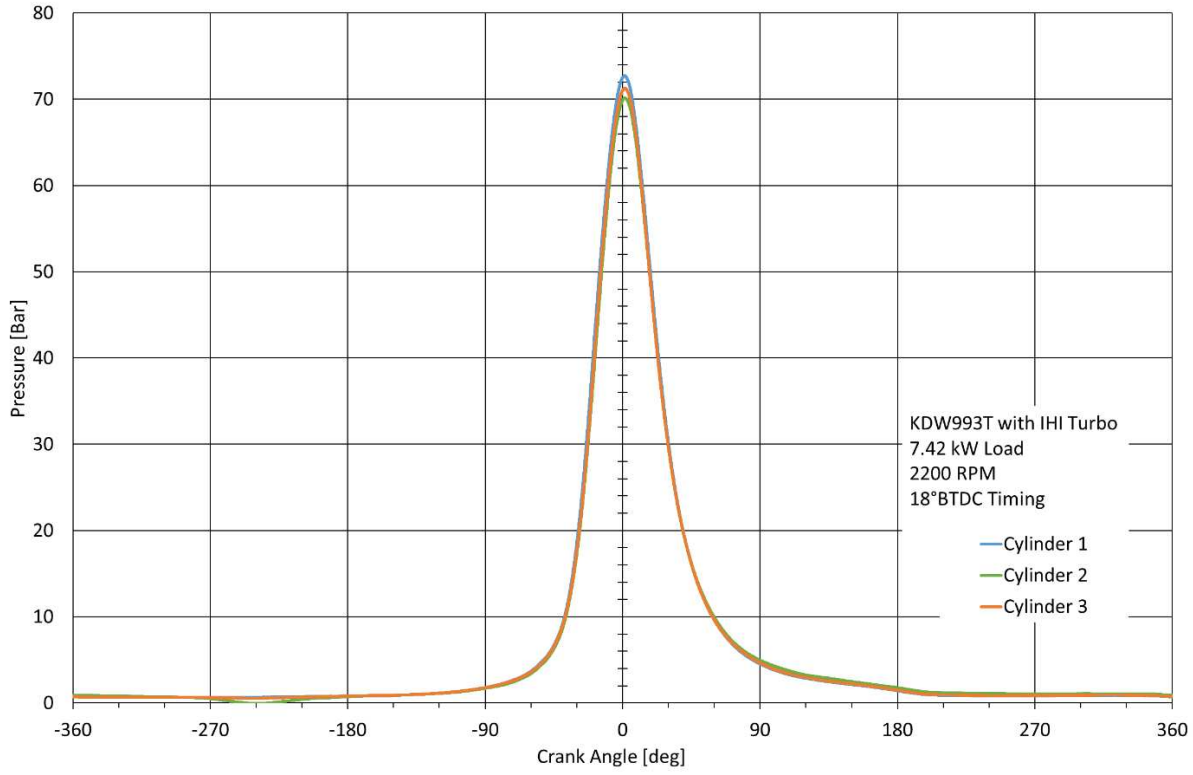

Figure 69: Average Cylinder Pressure Curves for 2200RPM and 18°BTDC Timing

Table 18: Cylinder Pressure Data at 2200 RPM and 30°BTDC Timing

Parameter	Cylinder 1	Cylinder 2	Cylinder 3	Average
Average Peak Pressure [Bar]	75.14	72.88	73.63	73.88
Max Peak Pressure [Bar]	75.84	73.68	74.54	74.69
Min Peak Pressure [Bar]	73.74	72.12	72.70	72.85
Peak Pressure Standard Deviation	0.379	0.374	0.312	0.355
Peak Pressure COV	0.504	0.514	0.424	0.481
Average Peak Pressure Location [°ATDC]	1.141	1.291	1.203	1.207
Peak Location Standard Deviation	0.317	0.389	0.271	0.325
Peak Location COV	27.75	30.11	22.49	26.78

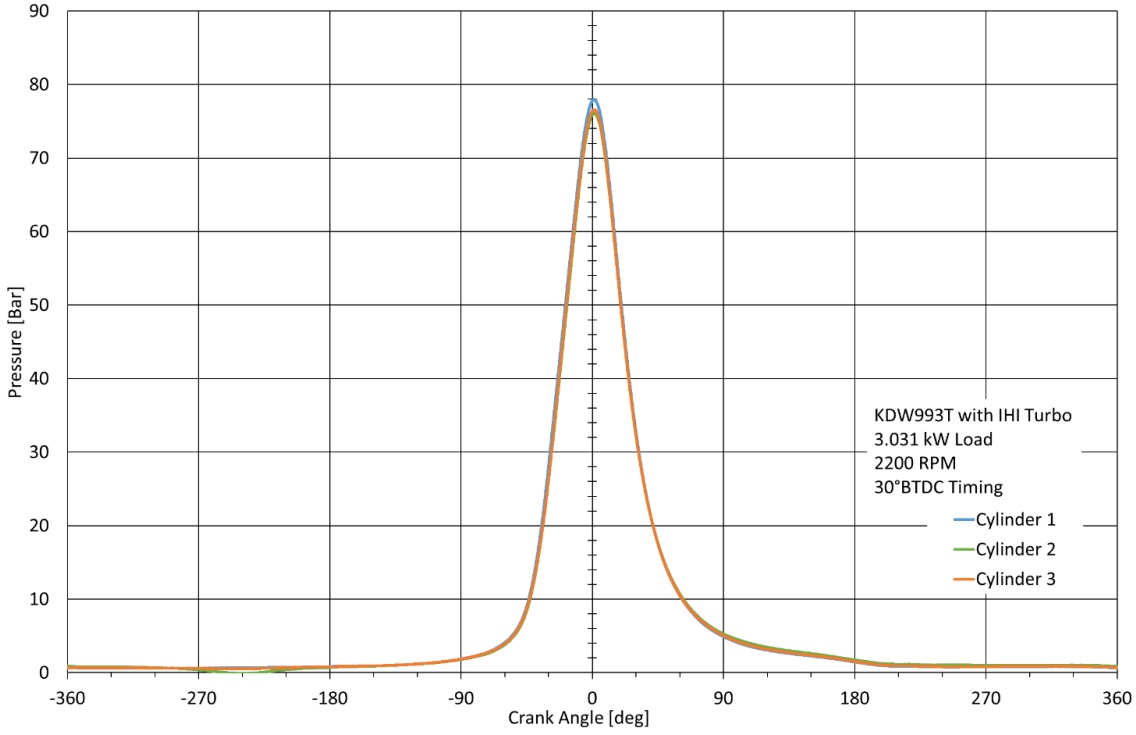

Figure 70: Average Cylinder Pressure Curves for 2200RPM and 30°BTDC Timing

Figure 71 shows the average peak cylinder pressure for all tested conditions. Increasing engine speed increased the peak pressure for every case tested, due to both increased turbocharger speed and more boost at higher engine speeds. This higher pressure may also be caused by the lower residence time at higher engine speeds, retaining more energy in the cylinder. Advancing the ignition timing also had the effect of raising the peak pressures observed. Due to the combustion starting earlier in the cycle, allowing more fuel to burn before TDC, thus increasing the maximum pressure seen. A maximum average peak pressure of 73.88 Bar was observed at 2200 RPM and 30° timing.

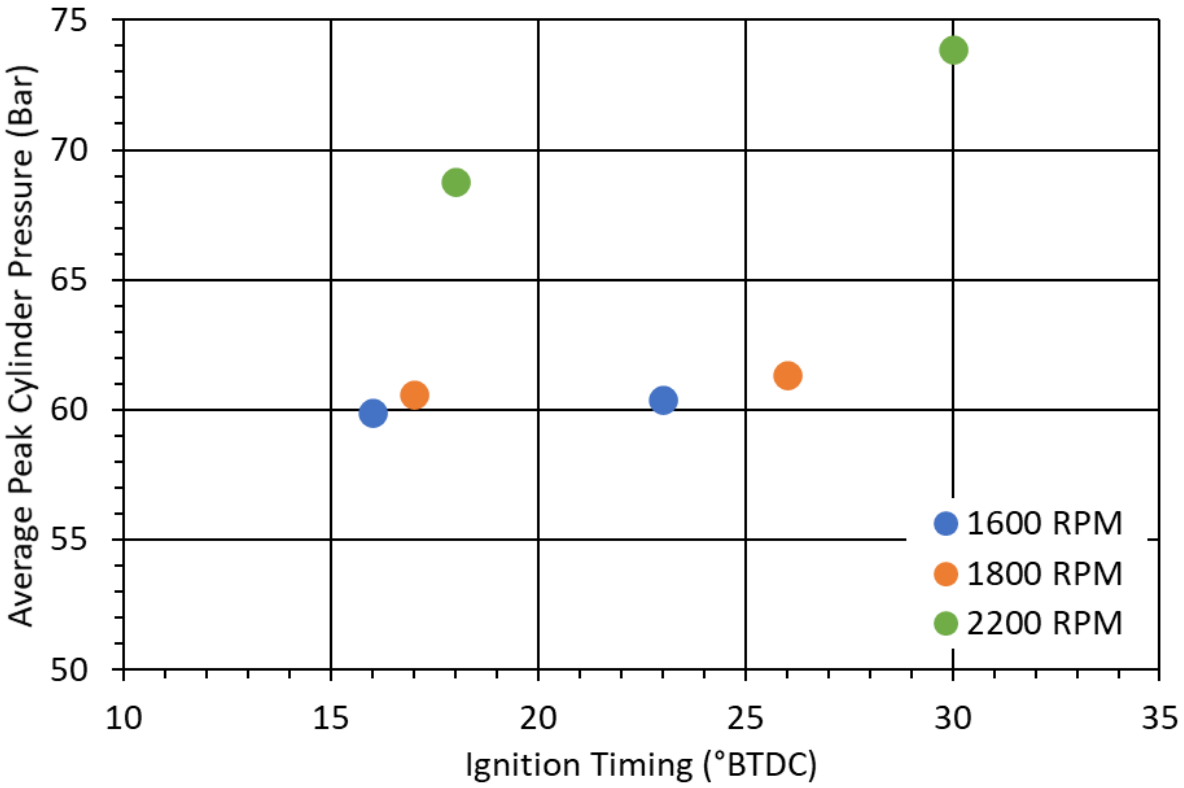

Figure 71: Average Peak Cylinder Pressure at Tested Conditions

Figure 72 shows the peak pressure coefficient of variation (COV) at all conditions tested. At the retarded timings increasing the engine speed had the effect of increasing the COV. At the

advanced timings increasing the engine speed had the effect of decreasing the COV. This effect is due to the residence time lowering as engine speed increases, and the small advance in timing not being large enough to compensate. Thus the combustion process may not be fully complete at TDC, increasing the COV.

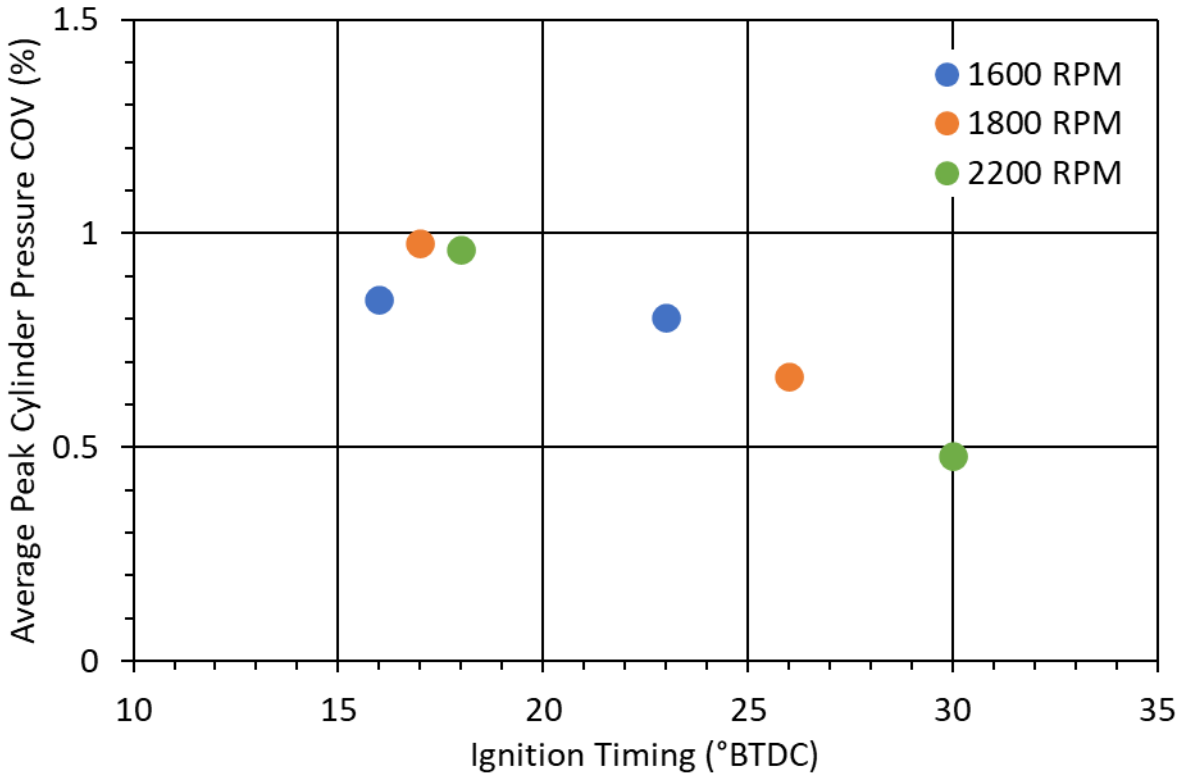

Figure 72: Average Peak Cylinder Pressure COV at Tested Conditions

Figure 73 shows the average peak pressure location for all tested conditions. For a SI engine advancing the ignition timing should shift the peak location towards TDC. For every speed advancing the ignition timing moved the peak location more ATDC. Increasing engine speed shifted the maximum peak pressure location later in the cycle as well. A regular SI engine has a location of peak pressure around 18° ATDC [12]. Interestingly, this engine has a peak location around 1° ATDC, and ignition timing has no significant impact on its location. There

may be a more complicated combustion process going on here; this will be explored further in Section 4.3.3 and merits further study. The engine produces a large amount backfires, so this insensitivity to ignition timing may be caused by pre-ignition occurring during the compression stroke. The latest location ATDC occurred at 2200 RPM and 30°BTDC timing giving a location of 1.207°ATDC.

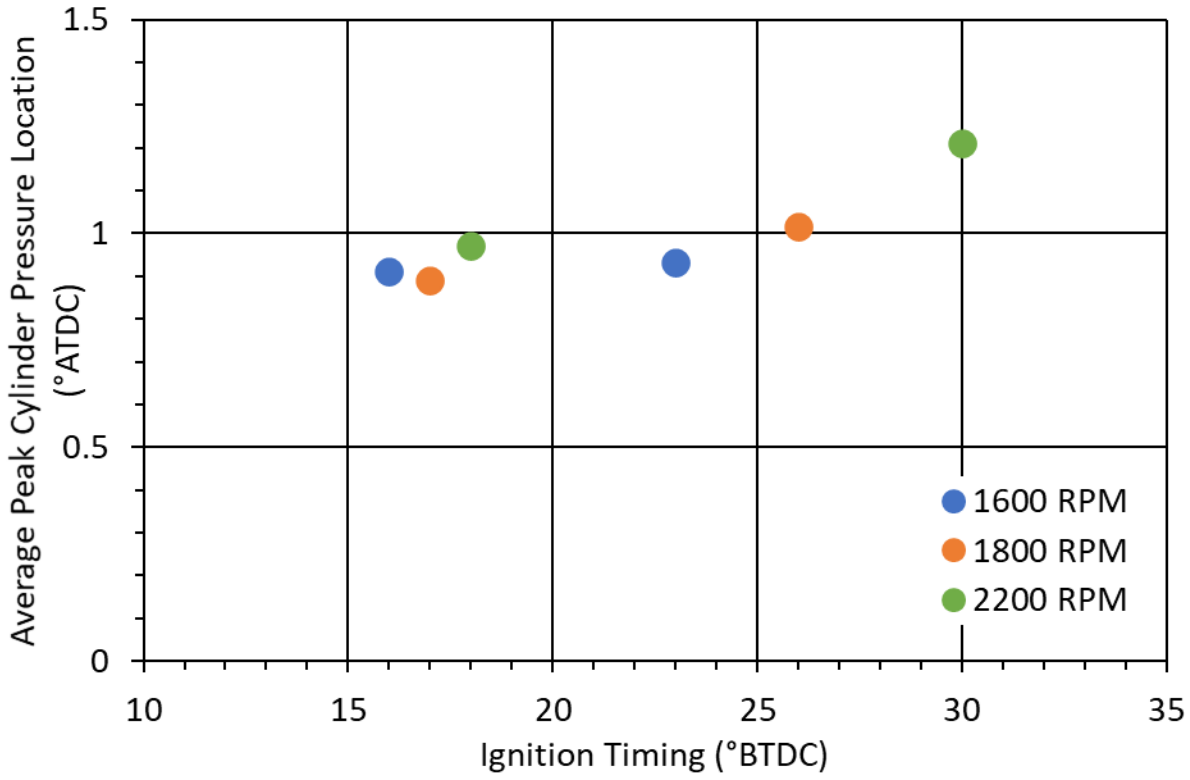

Figure 73: Average Peak Cylinder Pressure Location at all Tested Conditions

Figure 74 shows the peak pressure location COV for all tested conditions. The COV is relatively high. This is due to the low absolute value and the high standard deviation of around 0.4° relative to the absolute value. Advancing the ignition timing had the effect at every speed of decreasing the COV. This is due to the combustion process being more complete by the time peak pressure occurs. Raising the engine speed also had the effect of reducing the COV for

almost every condition, except 1800RPM and 17°, where the COV slightly increased. A minimum COV of 26.8% occurred at 2200 RPM and 30° BTDC timing.

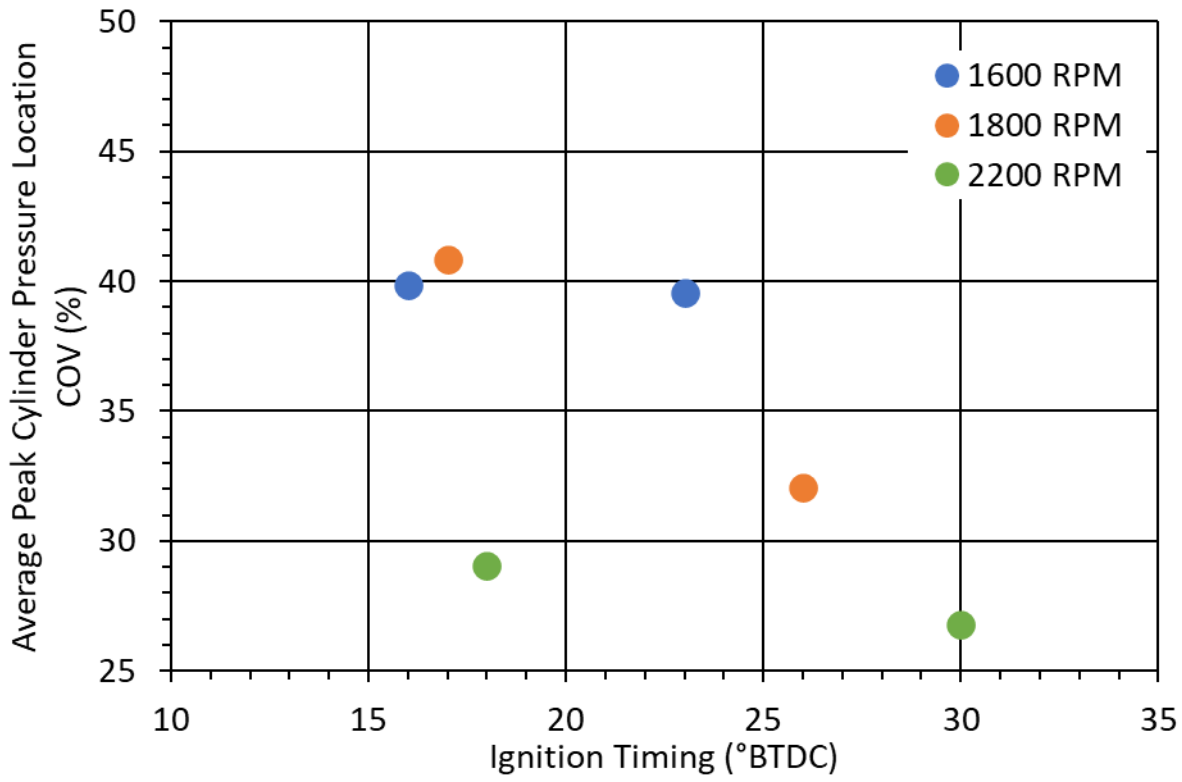

Figure 74: Average Peak Cylinder Pressure Location COV at all Tested Conditions

4.3.2 INDICATED MEAN EFFECTIVE PRESSURE

Indicated mean effective pressure (IMEP) is the average pressure on the piston over the entire cycle. It is the average pressure required to have the same area under the curve as the actual pressure trace. IMEP can be used as a performance indicator, and to calculate the friction losses in the engine by subtracting BMEP from IMEP. Tables 19-24 show the IMEP data gathered for all the test conditions. IMEP did not vary significantly across the entire test; IMEP

stability was good for every test condition. It is interesting to note that cylinder 2 has better IMEP stability with a lower COV and standard deviation than cylinders 1 and 2.

Table 19: IMEP Data at 1600RPM and 16°BTDC Timing

Parameter	Cylinder 1	Cylinder 2	Cylinder 3	Average
Average IMEP [Bar]	3.929	4.418	3.565	3.971
IMEP Standard Deviation	0.197	0.191	0.213	0.200
IMEP COV	5.003	4.334	5.960	5.099

Table 20: IMEP Data at 1600RPM and 23°BTDC Timing

Parameter	Cylinder 1	Cylinder 2	Cylinder 3	Average
Average IMEP [Bar]	3.947	4.125	3.698	3.923
IMEP Standard Deviation	0.374	0.324	0.383	0.361
IMEP COV	5.311	3.871	6.882	5.355

Table 21: IMEP Data at 1800RPM and 17°BTDC Timing

Parameter	Cylinder 1	Cylinder 2	Cylinder 3	Average
Average IMEP [Bar]	3.947	4.125	3.698	3.923
IMEP Standard Deviation	0.214	0.177	0.202	0.197
IMEP COV	5.412	4.285	5.463	5.053

Table 22: IMEP Data at 1800RPM and 26°BTDC Timing

Parameter	Cylinder 1	Cylinder 2	Cylinder 3	Average
Average IMEP [Bar]	3.915	4.019	3.933	3.956
IMEP Standard Deviation	0.175	0.155	0.202	0.177
IMEP COV	4.466	3.847	5.138	4.484

Table 23: IMEP Data at 2200RPM and 18°BTDC Timing

Parameter	Cylinder 1	Cylinder 2	Cylinder 3	Average
Average IMEP [Bar]	4.516	5.064	4.667	4.749
IMEP Standard Deviation	0.199	0.222	0.221	0.214
IMEP COV	4.409	4.385	4.732	4.509

Table 24: IMEP Data at 2200RPM and 30°BTDC Timing

Parameter	Cylinder 1	Cylinder 2	Cylinder 3	Average
Average IMEP [Bar]	3.950	4.510	4.212	4.224
IMEP Standard Deviation	0.213	0.224	0.196	0.211
IMEP COV	5.401	4.968	4.644	5.004

Figure 75 shows the average IMEP for all the conditions tested. A maximum IMEP of 4.749 bar occurred at 2200 RPM and 18° timing. This is also the point of max power. Cylinder pressures at this point are higher than other tested points, and thus the area under its curve is higher. The lowest IMEP of 3.923 bar occurred at 1800 and 17° timing.

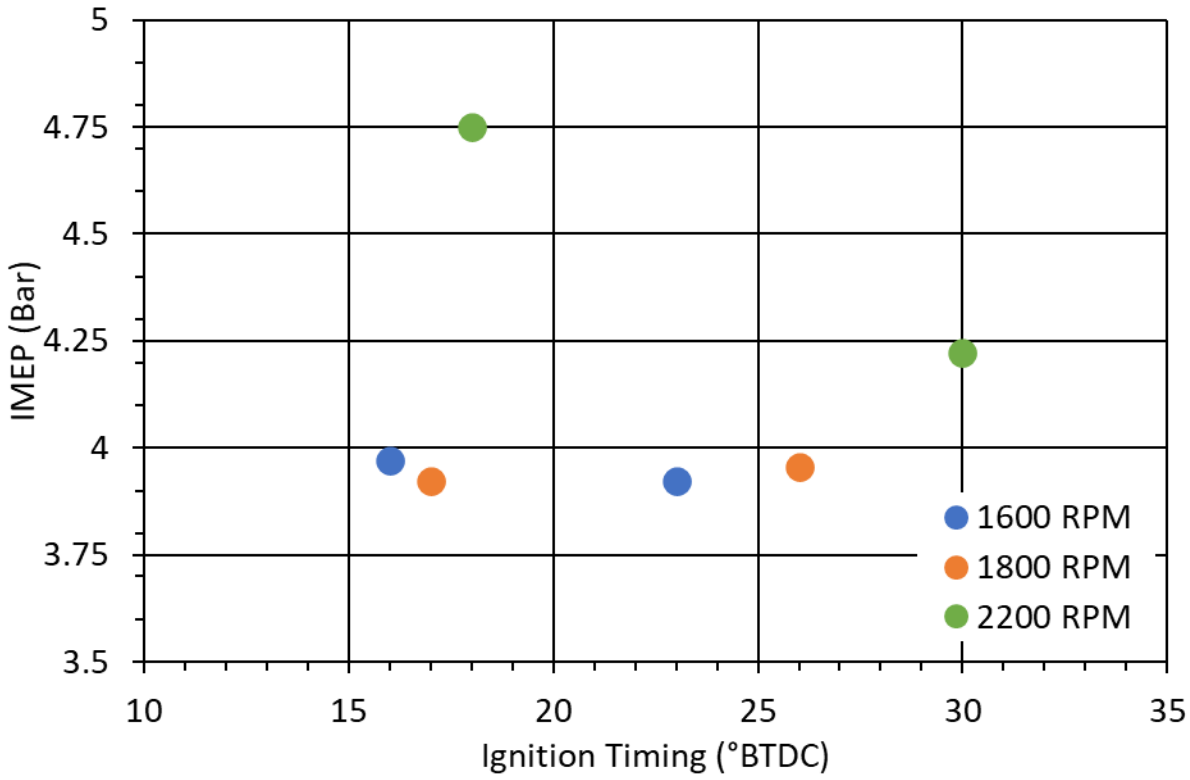

Figure 75: IMEP at all Tested Conditions

Figure 76 shows the IMEP COV for all tested conditions. Minimum IMEP COV of 4.48% occurs at 1800 RPM and 26° timing, coinciding with the point of the highest quality combustion, as indicated by the emissions. A maximum IMEP COV of 5.10% occurred at 1600 RPM and 23° timing. Advancing the ignition timing increased the IMEP COV for speeds 1600 and 2200 RPM, while at 1800 RPM, it decreased the IMEP COV. Increasing the speed lowered IMEP COV for the retarded timings, but at the advanced timings, IMEP COV dropped until 2200 RPM, where it increased.

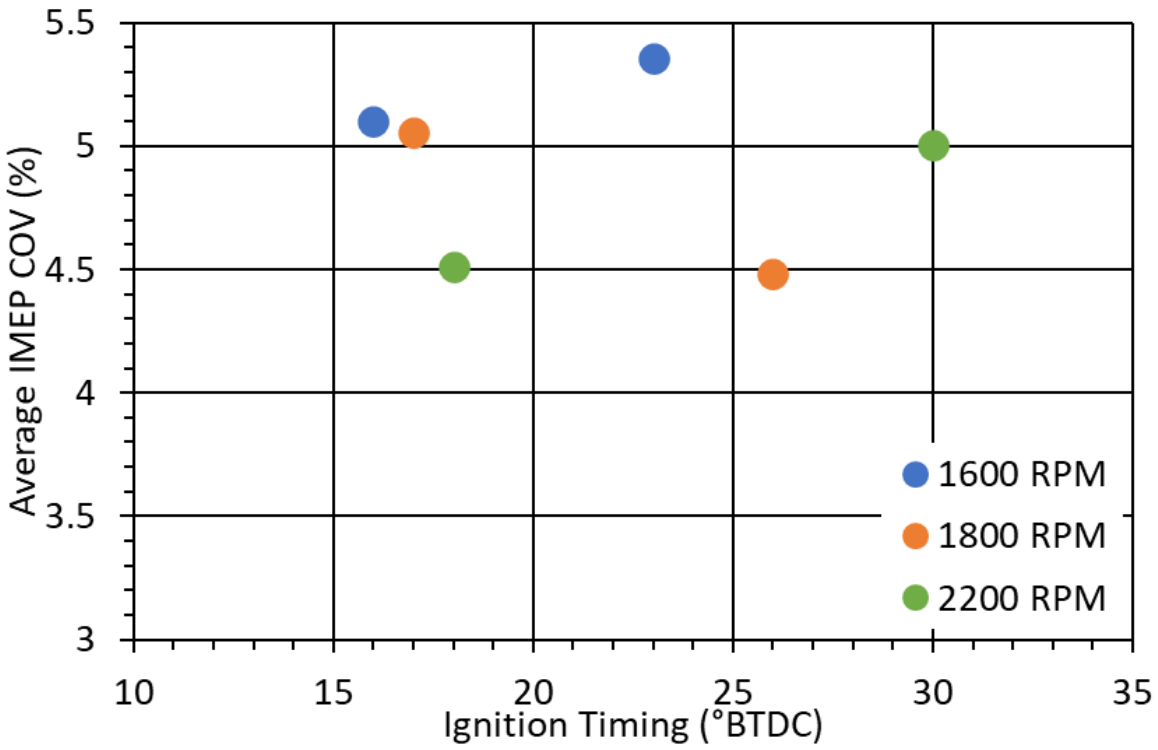

Figure 76: IMEP COV at all Tested Conditions

4.3.3 HEAT RELEASE RATE

The heat release data obtained from the combustion analyzer is of little value outside of a narrow range due to the 1st law being invalid in an open system. There is an extreme amount of noise in the data, as can be seen in Figure 77.This noise is normal for this type of dataset. Noise can be limited by looking at the late compression and early expansion strokes where the combustion is occurring. This limited view can be seen in Figure 78. From this figure, it can be seen that a significant heat release spike is happening at 30°BTDC. This spike is before the spark angle of 16°, indicating that there may be pre-ignition occurring. To further reduce the noise, a five-point moving average was taken to smooth the data. This procedure can be seen in Figure 79.

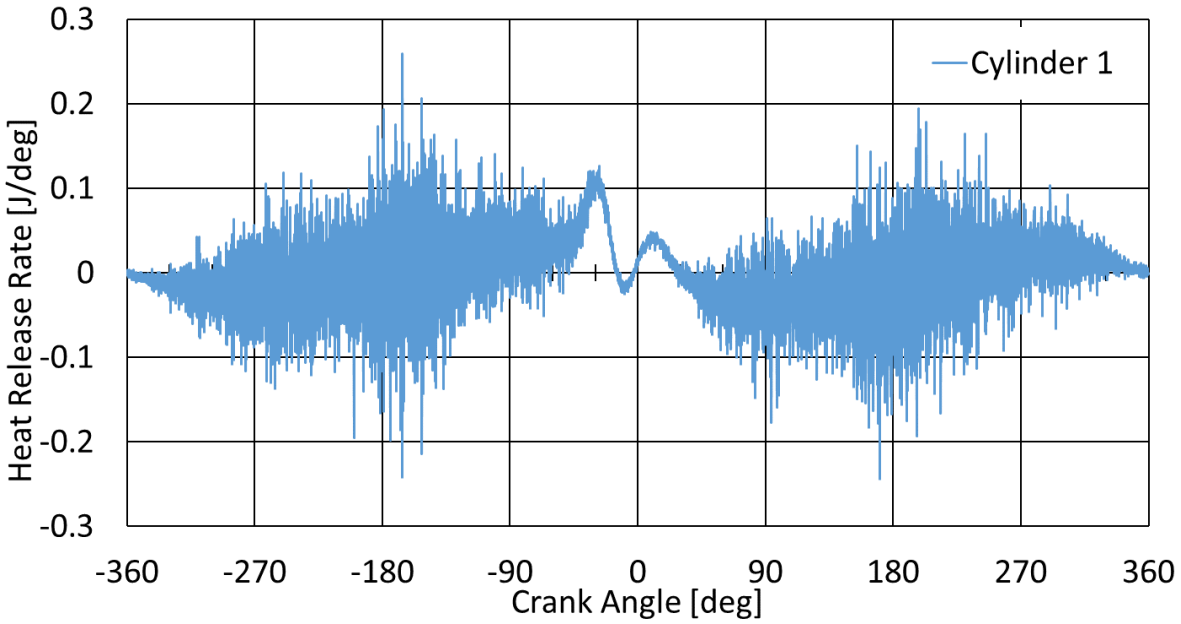

Figure 77: Raw Heat Release Rate Graph for 1600RPM and 16°BTDC Timing

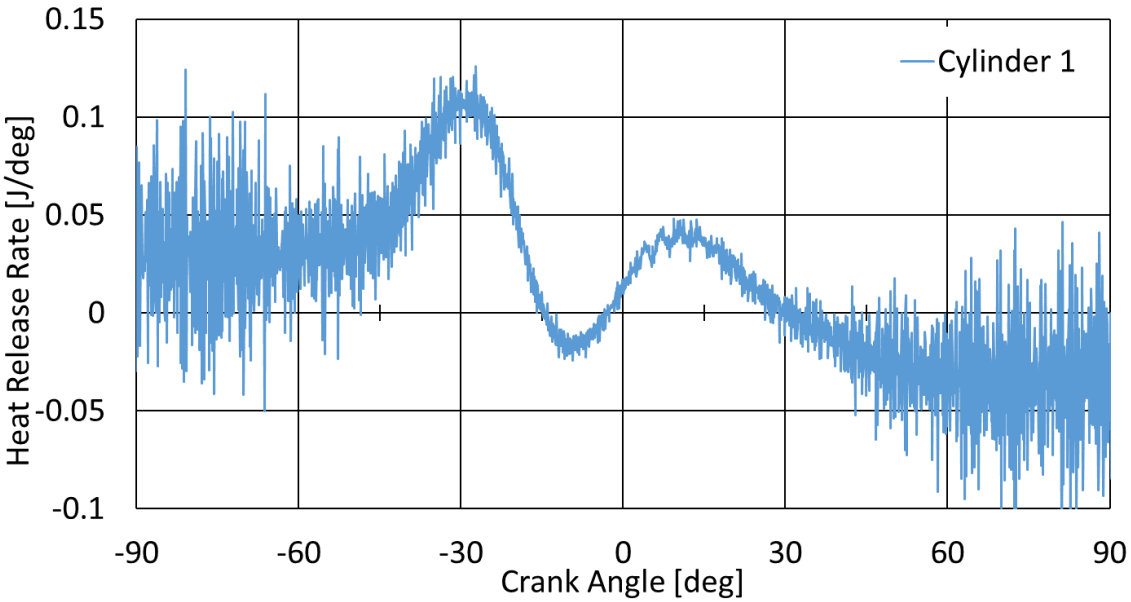

Figure 78: Detail View HRR for 1600RPM and 16°BTDC Timing

The HRR is positive during the compression stroke indicating heat transfer is occurring from the cylinder walls to the charge. A significant spike occurs at 30°BTDC; this is before the

start of combustion at 16°. Indicating that pre-ignition may be occurring. A second spike occurs at 12° ATDC; this shows that the combustion is happening in two phases. An SI engine usually has a smooth curve shown in figure 80. After the second spike, the HRR goes negative, indicating heat transfer from the cylinder charge to the cylinder walls.

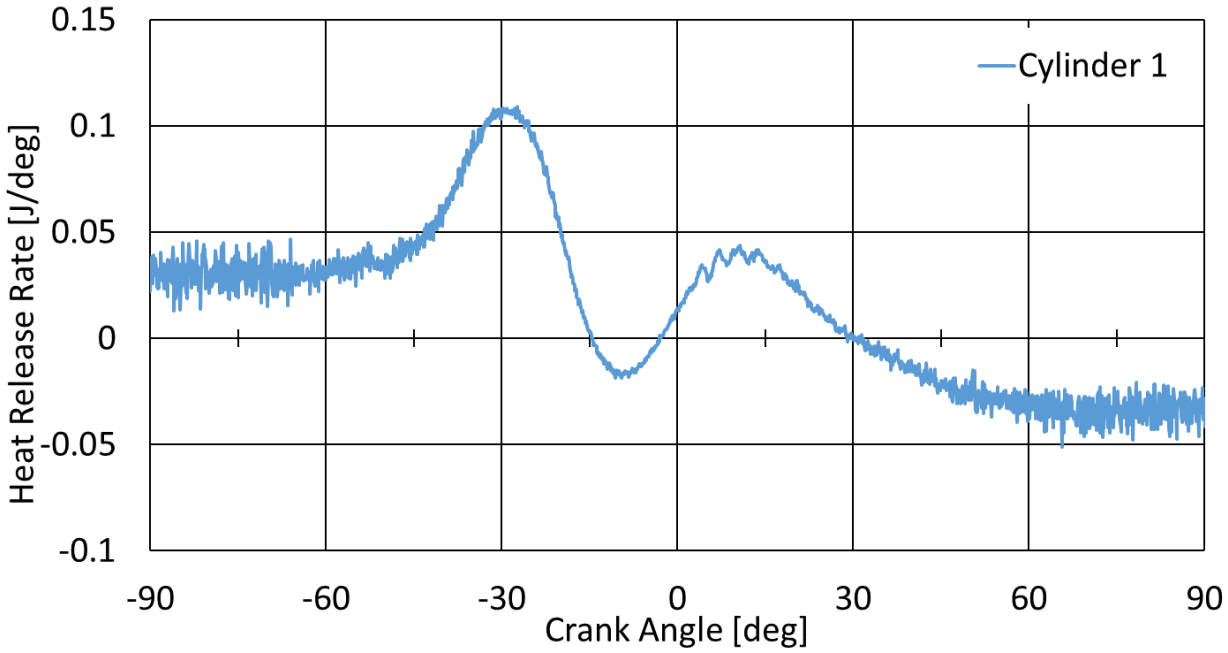

Figure 79: Smoothed HRR for 1600 RPM and 16°BTDC Timing

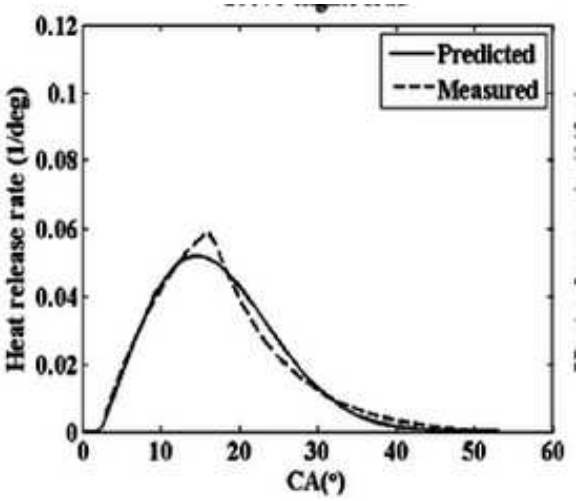

Figure 80: SI Heat Release Rate [22]

This early HRR spike before spark timing can explain the insensitivity of the peak pressure location to spark timing. If uncontrolled ignition events are occurring consistently, then the spark timing will have little effect on the start of combustion and, thus the peak pressure location. The smoothed graphs for every other test condition can be seen in Figures 81 through 85.

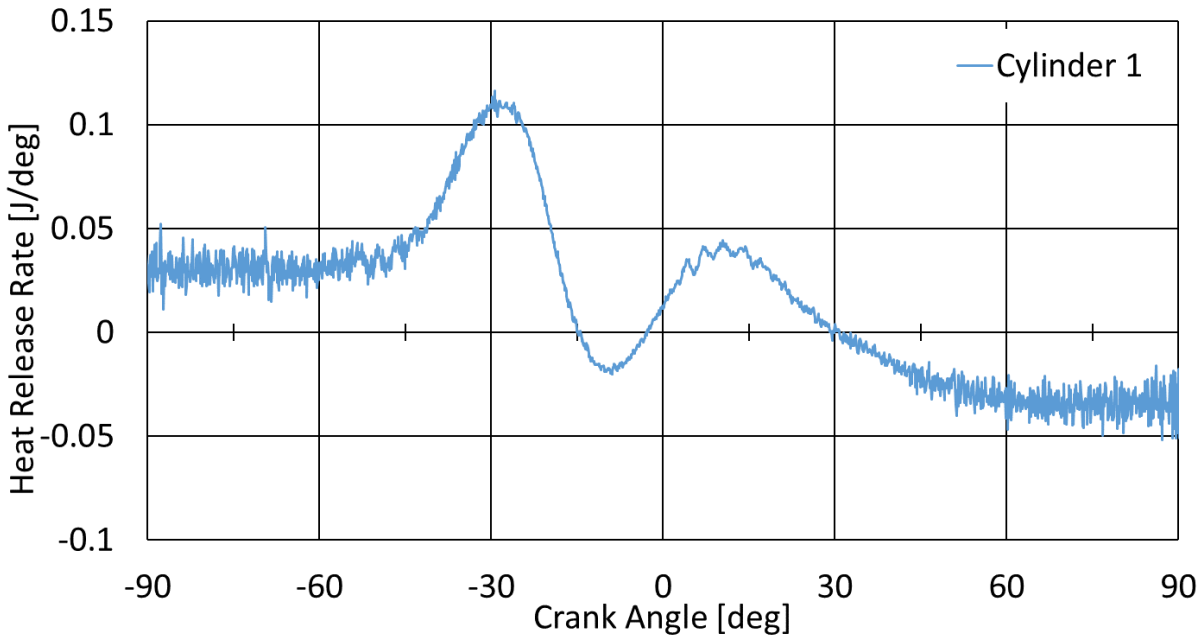

Figure 81: Smoothed HRR at 1600 RPM and 23°BTDC Timing

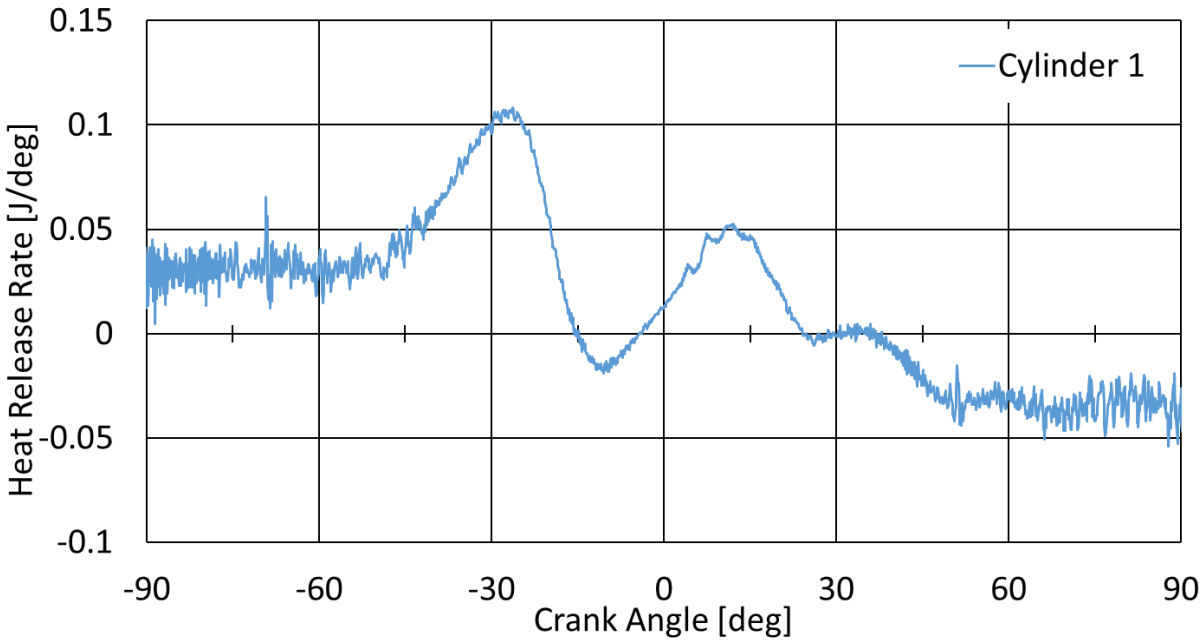

Figure 82: Smoothed HRR at 1800 RPM and 17°BTDC Timing

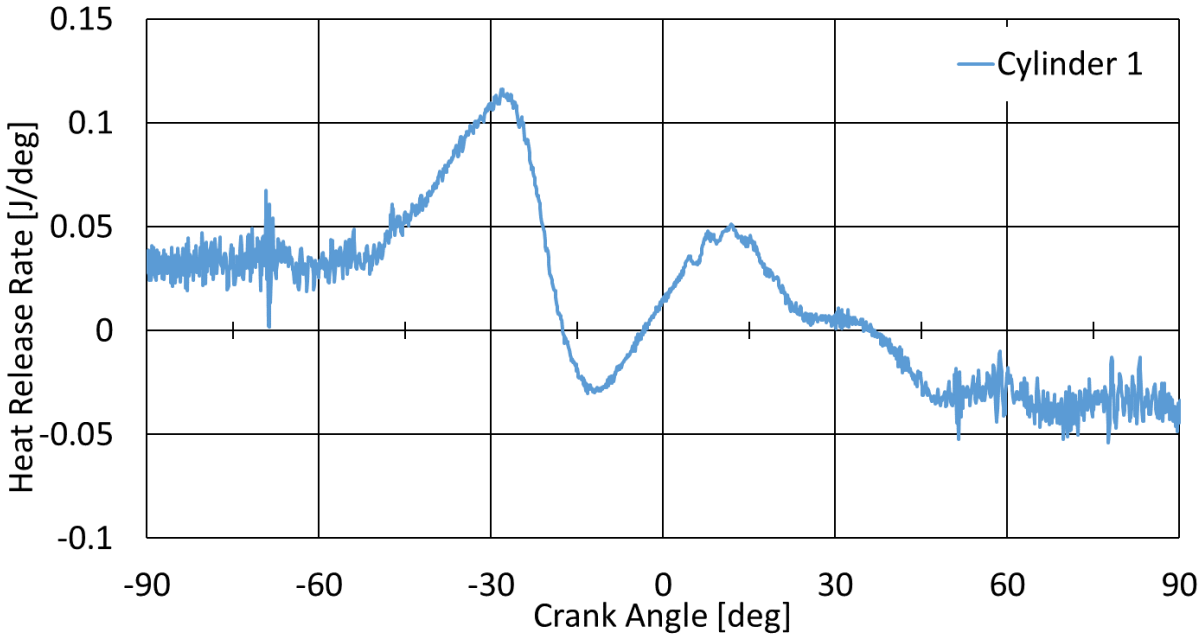

Figure 83: Smoothed HRR at 1800 RPM and 26°BTDC Timing

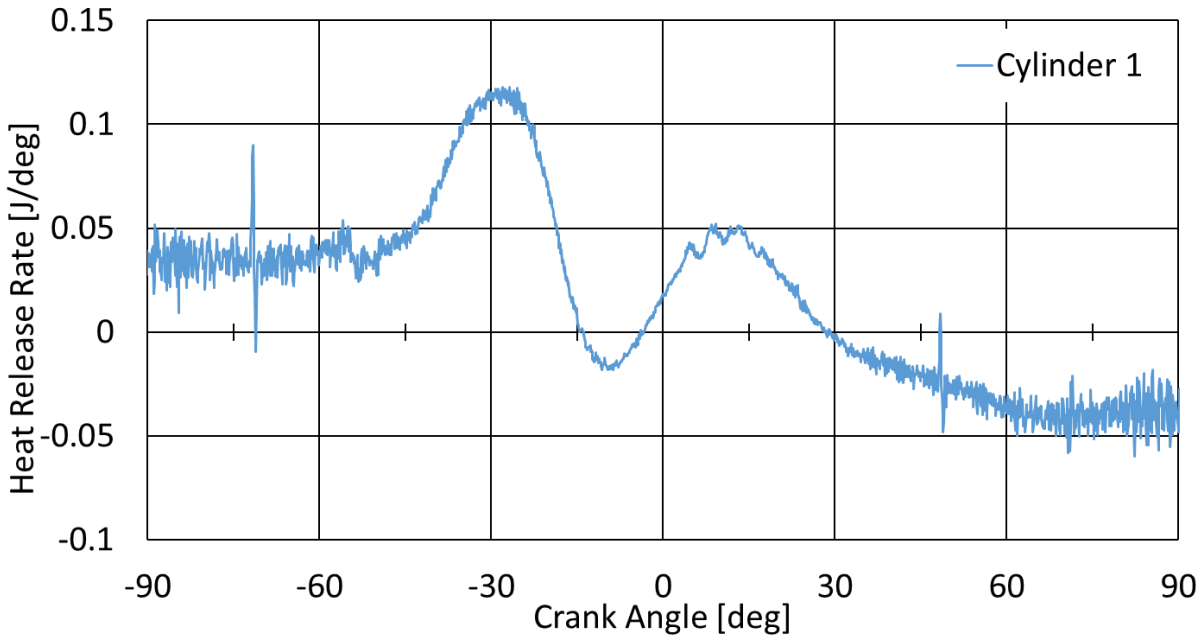

Figure 84: Smoothed HRR at 2200 RPM and 18°BTDC Timing

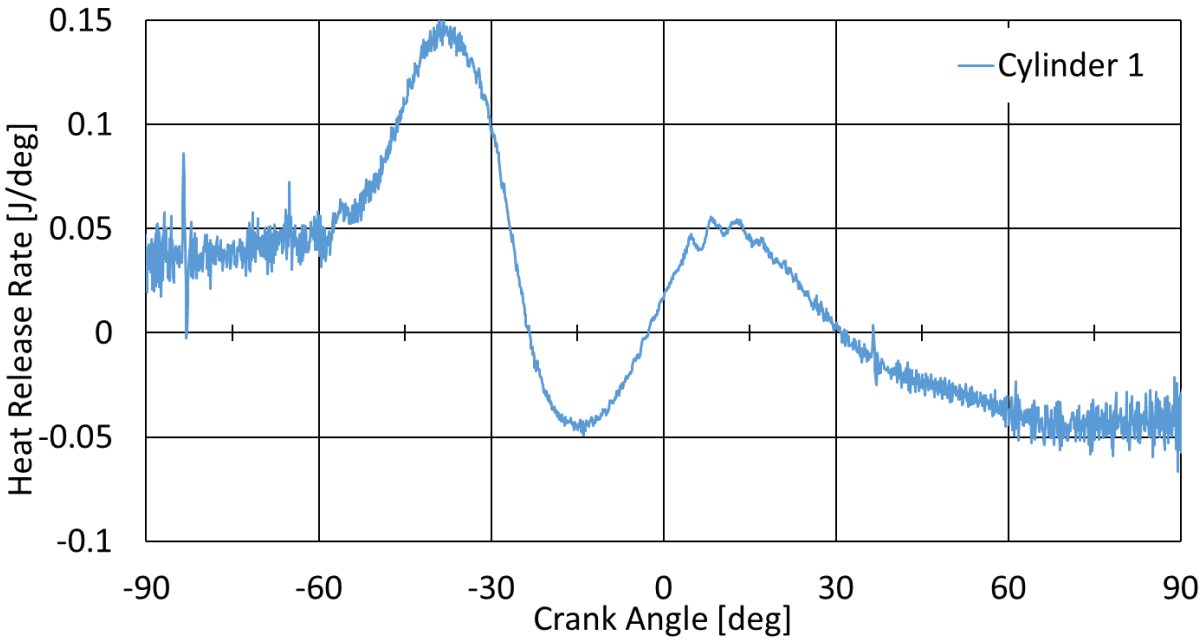

Figure 85: Smoothed HRR at 2200 RPM and 30°BTDC Timing

For every test condition except 2200 RPM and 30° a peak in HRR occurs at 30°BTDC. Combustion is occurring consistently before the spark is lit. This peak indicates an abnormal

combustion process is occurring. Uncontrolled ignition could be responsible for the high amount of backfires that are present. At 2200 RPM and 30° this peak is shifted forward to 40°BTDC. This peak explains the significant drop in brake efficiency at this operating point. With the major combustion event occurring a substantial amount of time before TDC more energy must be expended, working against the rapid pressure rise during the final part of the compression stroke.

This theory is supported by significant metallic deposits found on the spark plugs after testing. These deposits are welded onto the exposed face of the spark plug (Figure 86). The most likely source of these aluminum fragments is the pistons. Pre-ignition causes hot spots, and rapid pressure rises in the cylinder, causing piston failure.

Figure 86: Cylinder 1 through 3 Spark Plug Deposits

CHAPTER 5: MODEL AND EXPERIMENTAL COMPARISON

To gauge how accurate the GT-Power model is, a comparison to the obtained data is necessary. The GT-Power model must be rerun since the experimental conditions are not the same as the initial modeling run. To run these conditions, the model had to be modified. A throttle controller had to be added downstream of the compressor outlet but before the intake manifold. The throttle overrides the turbocharger controller if to much boost is being produced at a given condition. The end environments were reduced from one bar to 0.85 bar to match the atmospheric conditions. The brake power, engine speed, and ignition timing are used as the initial conditions for the updated model. The controllers match the brake power and speed at the ignition timing; the same critical metrics used to validate the diesel model are compared between the model and the experimental data.

5.1: ALL METRICS OVERVIEW

Tables 25 to 30 provides an overview of all critical metrics compared between the model and experimental. It can be seen from these tables that the model matches well at 1600 RPM and 1800 RPM but starts to deviate at higher engine speeds. It can also be seen that the model matches better at more advanced ignition timings. This mismatch is most likely due to the poor modeling of ignition delays. Ignition delay is the most challenging part of the combustion process to model [23]. By allowing more time for the ignition process to occur BTDC, the model can predict performance more accurately. The best model/experimental agreement occurs at 1600 RPM and 26° timing—all critical metrics except exhaust pressure matched within 10%. The worst model/experimental agreement is 2200 RPM and 18° timing, where none of the critical metrics except the initial conditions matched within 10%.

Table 25: Comparison at 1600 RPM and 16° BTDC Timing

	GT-Power	Experimental	Percent Difference	Absolute Difference
Engine Speed [RPM]	1600	1600	0	0
Combustion Start [°BTDC]	16	16	0	0
Brake Torque [N*m]	34.4	34.4	0.05	0.02
Brake Power [kW]	5.76	5.77	0.08	0.01
Brake Efficiency [%]	27.8	27.3	-1.67	0.46
Average of Maximum Cylinder Pressures [Bar]	49.1	61.1	19.7	12.0
Maximum Cylinder Pressure [Bar]	50.2	62.2	19.2	12.0
Crank Angle at Maximum Cylinder Pressure [°ATDC]	6.68	0.92	-622	5.75
Average Intake Pressure [Bar]	0.87	0.92	4.87	0.04
Average Intake Temperature [°C]	47.6	52.8	9.88	5.22
Average Exhaust Pressure [Bar]	1.15	0.92	-25.8	0.24
Average Exhaust Temperature [°C]	550	430	-27.9	120

Table 26: Comparison at 1600 RPM and 23° BTDC Timing

	GT-Power	Experimental	Percent Difference	Absolute Difference
Engine Speed [RPM]	1600	1600	0	0
Combustion Start [°BTDC]	23	23	0	0
Brake Torque [N*m]	34.1	34.0	-0.19	0.07
Brake Power [kW]	5.71	5.70	-0.19	0.01
Brake Efficiency [%]	26.7	27.0	1.02	0.28
Average of Maximum Cylinder Pressures [Bar]	58.9	61.6	4.45	2.74
Maximum Cylinder Pressure [Bar]	60.1	62.4	3.67	2.29
Crank Angle at Maximum Cylinder Pressure [°ATDC]	5.32	1.05	-409	4.28
Average Intake Pressure [Bar]	0.90	0.92	1.89	0.02
Average Intake Temperature [°C]	47.5	50.7	6.16	3.12
Average Exhaust Pressure [Bar]	1.16	0.99	-16.20	0.16
Average Exhaust Temperature [°C]	517	475	-8.90	42

Table 27: Comparison at 1800 RPM and 17° BTDC Timing

	GT-Power	Experimental	Percent Difference	Absolute Difference
Engine Speed [RPM]	1800	1800	0	0
Combustion Start [°BTDC]	17	17	0	0
Brake Torque [N*m]	30.08	29.96	-0.37	0.11
Brake Power [kW]	5.67	5.65	-0.33	0.02
Brake Efficiency [%]	26.69	23.31	-14.48	3.38
Average of Maximum Cylinder Pressures [Bar]	45.6	61.2	25.5	15.6
Maximum Cylinder Pressure [Bar]	46.7	62.5	25.3	15.8
Crank Angle at Maximum Cylinder Pressure [°ATDC]	6.76	0.94	-617.61	5.82
Average Intake Pressure [Bar]	0.79	0.91	12.86	0.12
Average Intake Temperature [°C]	44.2	43.62	-0.91	0.40
Average Exhaust Pressure [Bar]	1.17	0.83	-41.14	0.34
Average Exhaust Temperature [°C]	561	531	-6	30

Table 28: Comparison at 1800 RPM and 26° BTDC Timing

	GT-Power	Experimental	Percent Difference	Absolute Difference
Engine Speed [RPM]	1800	1800	0	0
Combustion Start [°BTDC]	26	26	0	0
Brake Torque [N*m]	32.40	32.30	-0.32	0.10
Brake Power [kW]	6.11	6.09	-0.30	0.02
Brake Efficiency [%]	25.79	25.52	-1.03	0.26
Average of Maximum Cylinder Pressures [Bar]	61.5	61.7	0.2	0.1
Maximum Cylinder Pressure [Bar]	62.9	62.6	-0.5	0.3
Crank Angle at Maximum Cylinder Pressure [°ATDC]	4.78	1.02	-370.89	3.76
Average Intake Pressure [Bar]	0.89	0.95	6.33	0.06
Average Intake Temperature [°C]	46.2	41.0	-12.65	5.19
Average Exhaust Pressure [Bar]	1.21	0.82	-47.26	0.39
Average Exhaust Temperature [°C]	799	534	-50	265

Table 29: Comparison at 2200 RPM and 18° BTDC Timing

	GT-Power	Experimental	Percent Difference	Absolute Difference
Engine Speed [RPM]	2200	2200	0	0
Combustion Start [°BTDC]	18	18	0	0
Brake Torque [N*m]	32.20	32.21	0.02	0.01
Brake Power [kW]	7.42	7.42	0.05	0.00
Brake Efficiency [%]	26.14	23.73	-10.16	2.41
Average of Maximum Cylinder Pressures [Bar]	51.0	70.1	27.3	19.1
Maximum Cylinder Pressure [Bar]	52.5	71.2	26.2	18.7
Crank Angle at Maximum Cylinder Pressure [°ATDC]	6.16	1.17	-425.82	4.99
Average Intake Pressure [Bar]	0.89	1.00	10.65	0.11
Average Intake Temperature [°C]	55.7	55.6	-0.18	0.10
Average Exhaust Pressure [Bar]	1.37	0.83	-65.45	0.54
Average Exhaust Temperature [°C]	601	480	-25	122

Table 30: Comparison at 2200 RPM and 30° BTDC Timing

	GT-Power	Experimental	Percent Difference	Absolute Difference
Engine Speed [RPM]	2200	2200	0	0
Combustion Start [°BTDC]	30	30	0	0
Brake Torque [N*m]	12.98	13.15	1.33	0.17
Brake Power [kW]	2.99	3.03	1.35	0.04
Brake Efficiency [%]	17.38	8.86	-96.17	8.52
Average of Maximum Cylinder Pressures [Bar]	39.9	75.1	49.9	35.2
Maximum Cylinder Pressure [Bar]	41.1	75.8	45.8	34.7
Crank Angle at Maximum Cylinder Pressure [°ATDC]	3.75	1.14	-229.07	2.61
Average Intake Pressure [Bar]	0.53	1.04	49.52	0.52
Average Intake Temperature [°C]	40.83	60.18	32.15	19.35
Average Exhaust Pressure [Bar]	1.07	0.83	-29.38	0.24
Average Exhaust Temperature [°C]	520	497	-5	23

5.2: BRAKE EFFICIENCY COMPARISON

The primary purpose of the GT-Power model is to predict brake efficiency. Comparing the model to the experimental at the acquired points provides insight into the brake efficiency prediction at full load. Figure 87 shows the brake efficiency at every data point for the experimental and model values. It can be seen from Figure 87 that the model matches brake efficiency quite well at low engine speeds and advanced ignition timings. But at high engine speeds, the predicted brake efficiency begins to deviate from the experimental values, with an extreme deviation at 2200 RPM and 30° timing. This deviation is most likely due to the

abnormal combustion process, which was discussed in Section 4.3.3. GT-Power does not accurately capture this phenomenon and, thus, can not accurately model it. The best efficiency prediction is at 1600 RPM and 23° timing with a percent difference of 1.02%, and an absolute difference of 0.28.

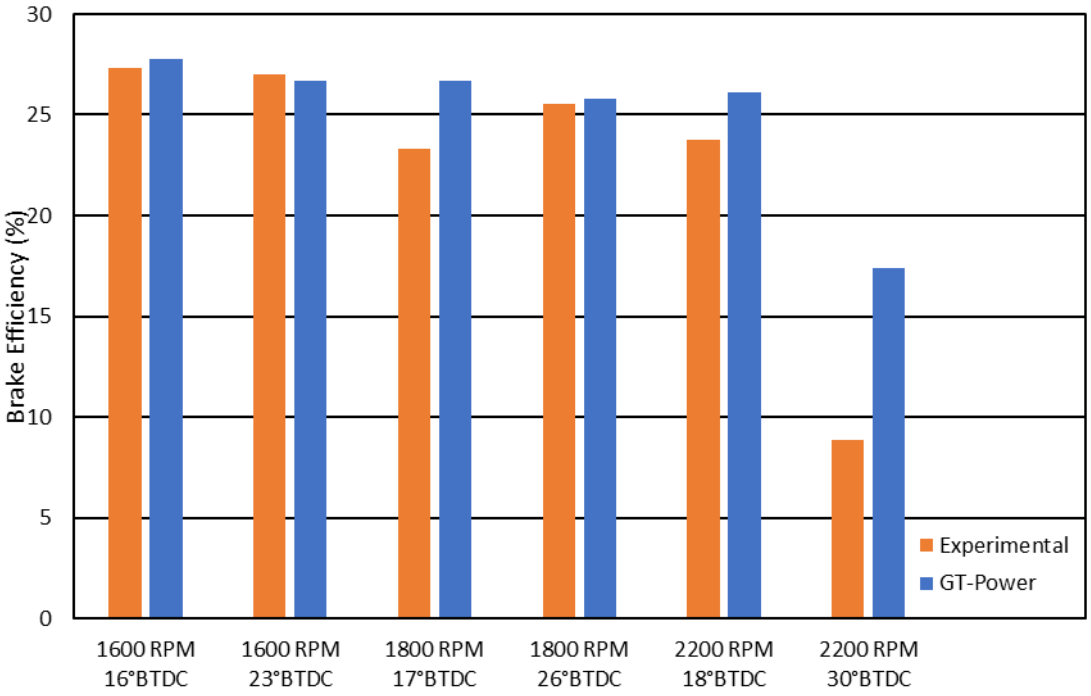

Figure 87: Brake Efficiency Comparison

5.3: CYLINDER PRESSURE COMPARISON

The cylinder pressure peak magnitude and location give a good overview of the quality of the combustion occurring in each case. Figure 88 shows the average maximum cylinder pressures for the experimental and model data. From Figure 88, it can be seen that the maximum cylinder pressures do not match well at retarded ignition timings for all speeds. This mismatch is most likely due to the model not capturing the ignition delay correctly. At the advanced timings for 1600 and 1800 RPM, the maximum cylinder pressures match well. The best match occurs at

1800 RPM and 26° timing, with a percent difference of 0.2%, and an absolute difference of 0.1 Bar. There was a large mismatch in predicted and measured pressures at 2200 RPM. The typical deviation at retarded ignition timing is present, but at the advanced timing, the deviation became worse. The deviation is most likely caused by the abnormal combustion process that was occurring, as discussed in Section 4.3.3. GT-Power does not capture this combustion phenomenon and can not model it correctly, resulting in a significant deviation.

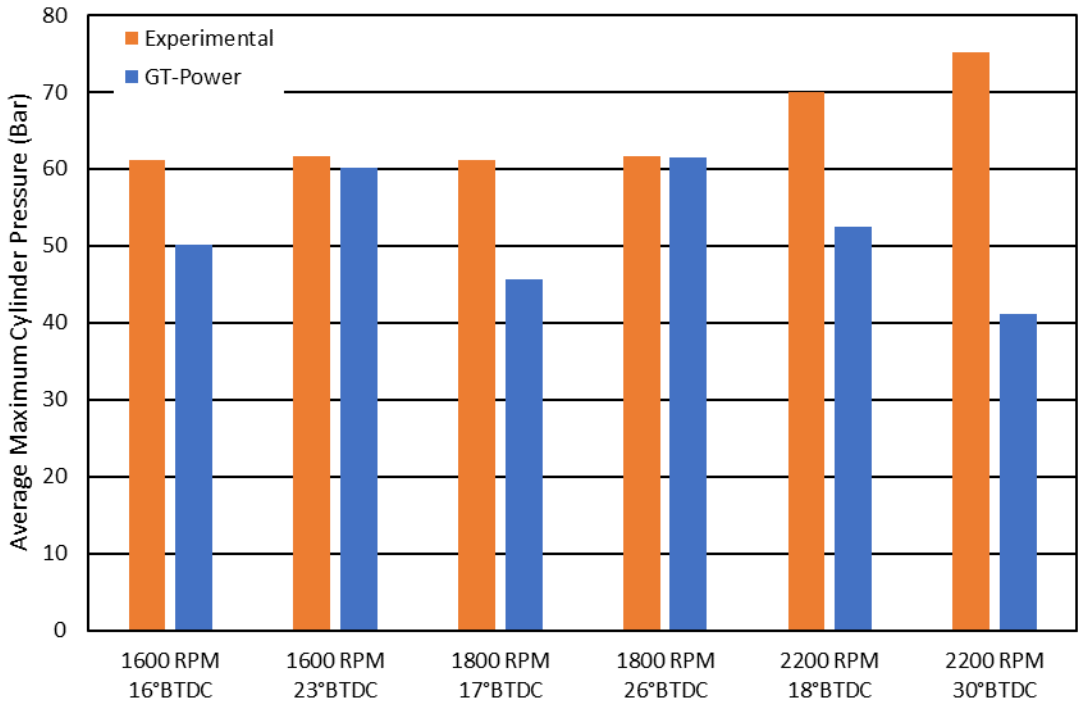

Figure 88: Average Maximum Cylinder Pressure Comparison

Figure 89 shows the location of maximum peak pressure for the experimental and model data. During experimental testing, spark timing was found to have little effect on maximum cylinder pressure location; this was discussed in Sections 4.3.1 and 4.3.3. During GT-Power modeling, the peak location was somewhat insensitive to spark timing, but it did have an influence. At all test points, the peak location did not match well. This mismatch is most likely

due to the odd combustion process described in Section 4.3.3. All points had percent differences in the 100's of %, due to the low absolute value of the peak pressure location. The absolute difference is a much better comparison for these values. The lowest absolute difference of 2.61° is at 2200 RPM and 30° timing. But this point has abnormal combustion and an extremely mismatched peak. The point with the lowest difference in a location with normal combustion is at 1800 RPM and 26° timing, with an absolute difference of 3.76°.

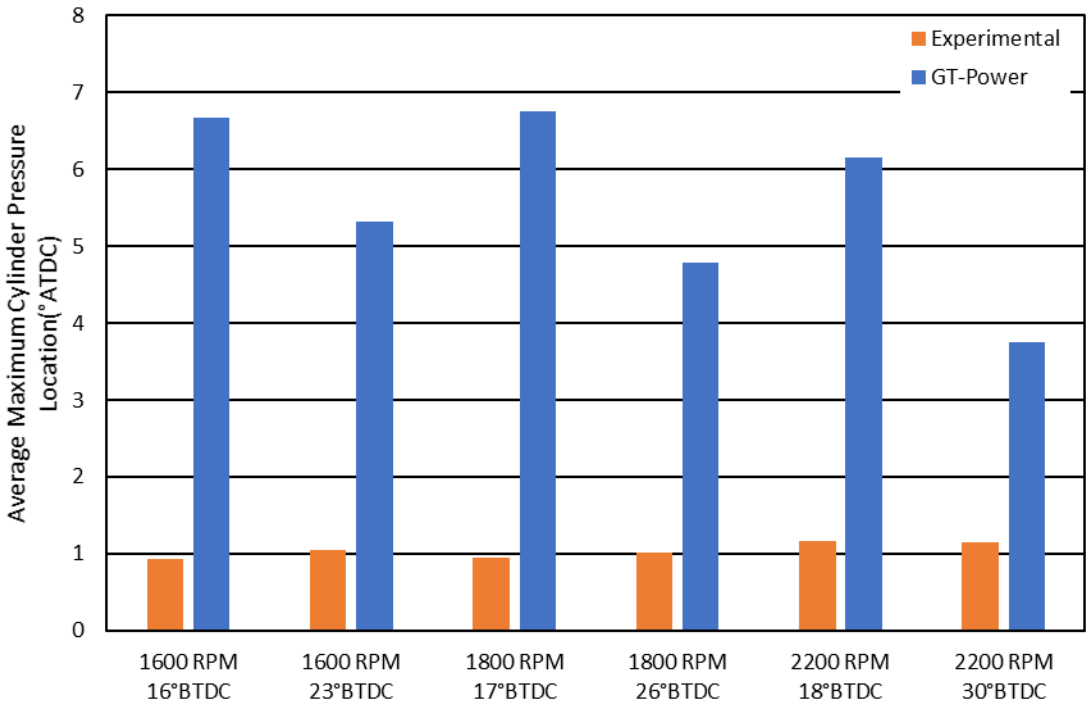

Figure 89: Average Maximum Cylinder Pressure Location Comparison

The cylinder pressure traces are an essential metric to compare. The traces identify any location where the pressures deviate. Not just the peak location and magnitude. These traces are seen in Figures 90 through 95. Figures 91 and 93 are the points where maximum peak pressure matched closest. During the compression stroke in these figures, the experimental data has a much higher rate of pressure rise than the GT-Power prediction. This early rise indicates the

combustion is occurring earlier in the experimental engine, supporting the pre-ignition theory. Most other points do not match well, the retarded timings at low speeds in Figures 91 and 93 show much higher peaks and earlier ignition than the GT-Power curves. Figure 96 shows 2200 RPM and 30° timing. GT-Power did not accurately predict this point. The predicted cylinder pressure is much lower than the experimental throughout the entire trace. This mismatch is due to GT-Power having to throttle to reach the low power level, resulting in low cylinder pressures.

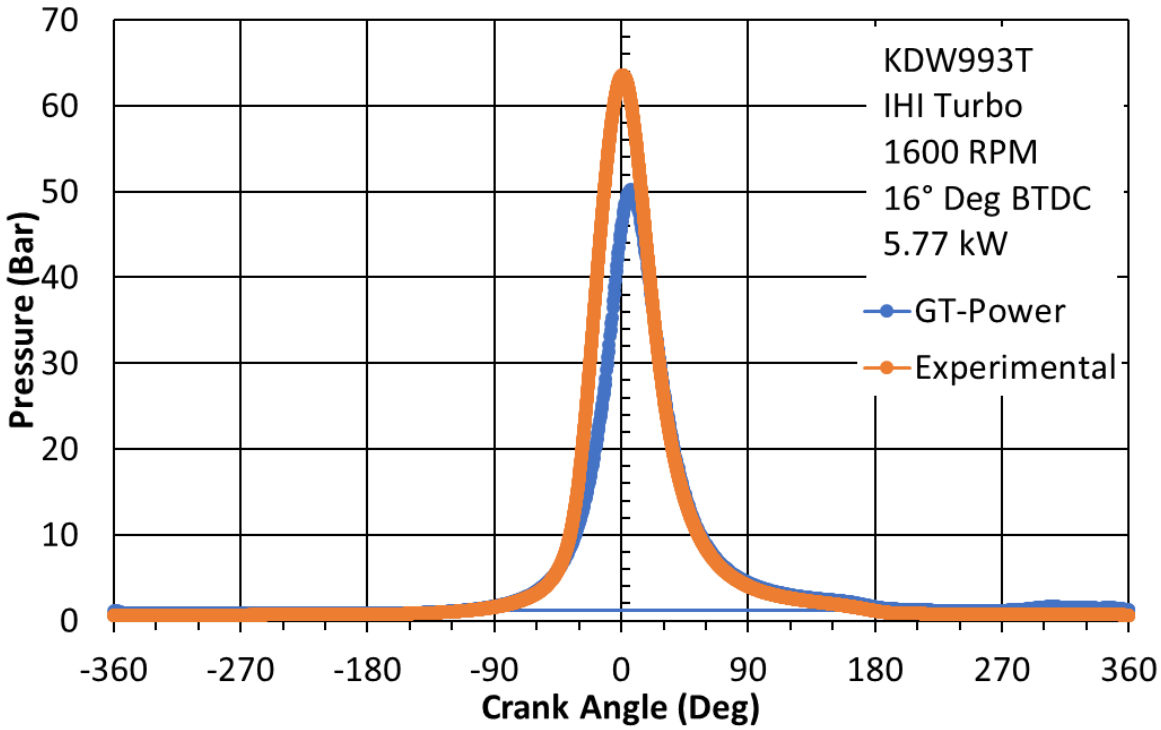

Figure 90: 1600 RPM and 16°BTDC Timing Pressure Curve Comparison

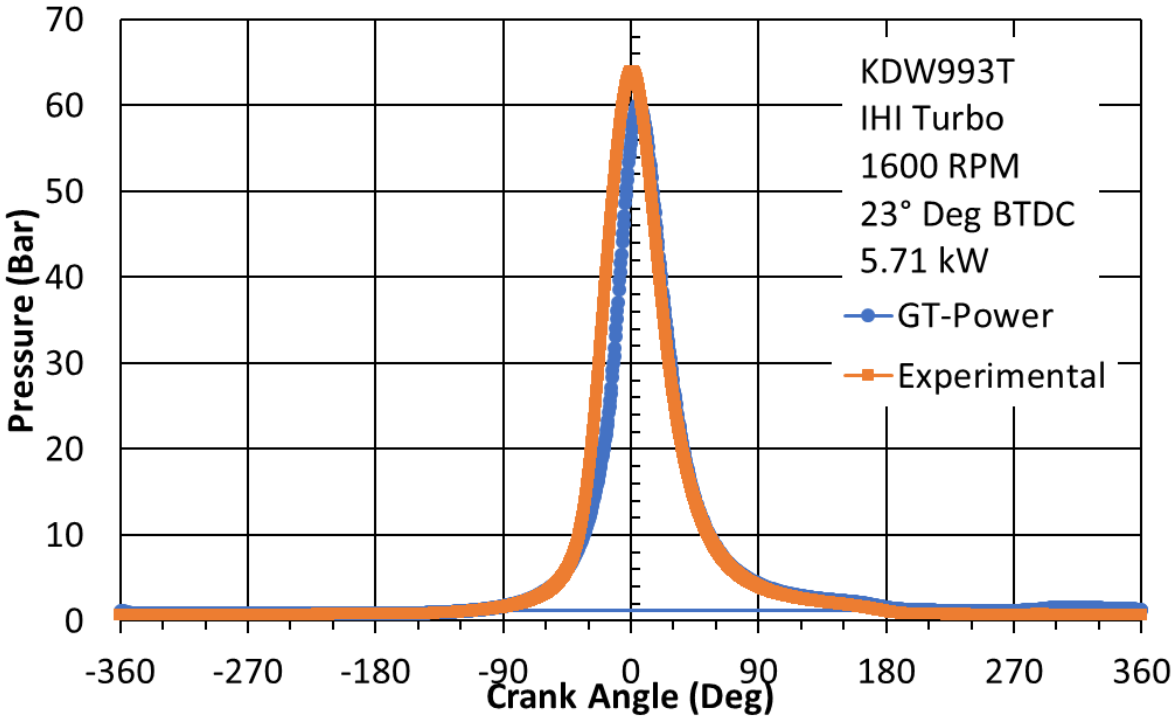

Figure 91: 1600 RPM and 23°BTDC Timing Pressure Curve Comparison

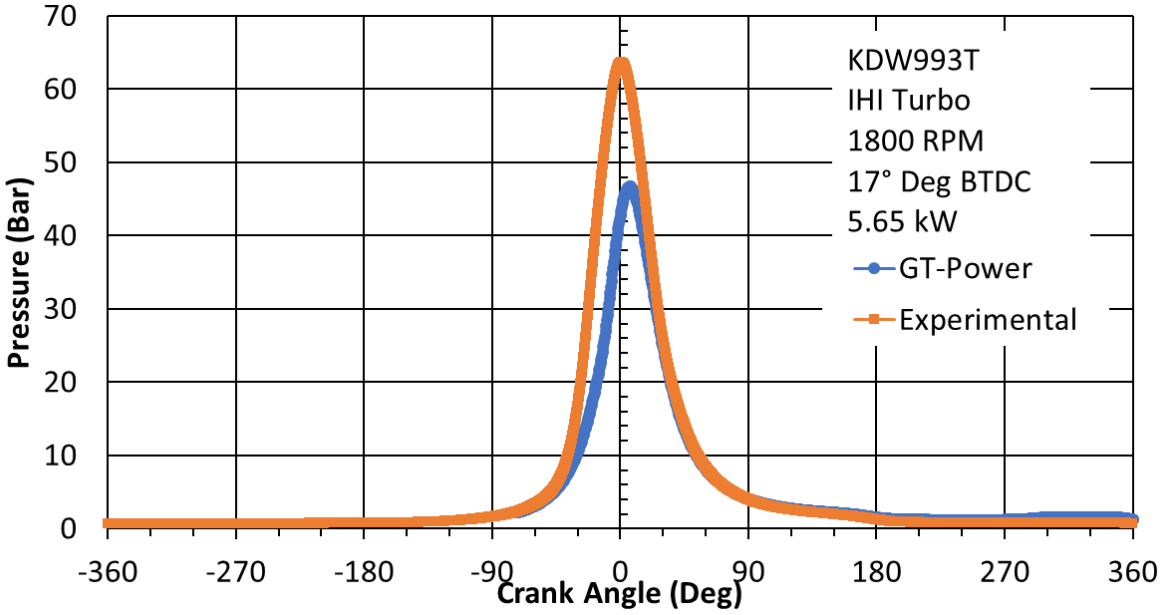

Figure 92: 1800 RPM and 17°BTDC Timing Pressure Curve Comparison

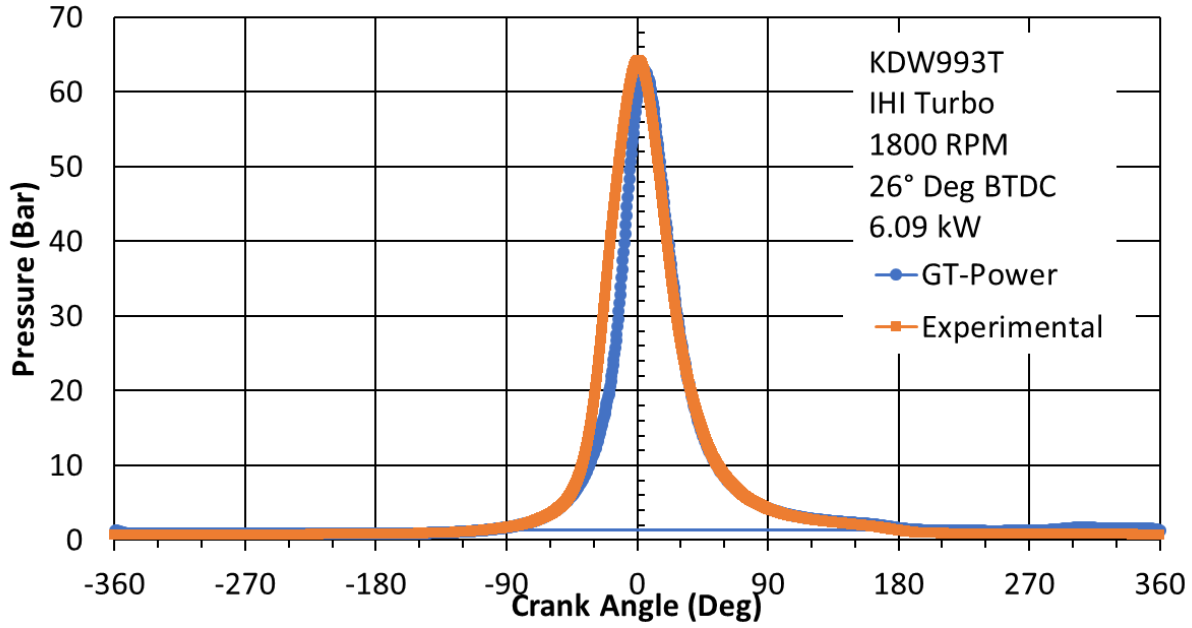

Figure 93: 1800 RPM and 26°BTDC Timing Pressure Curve Comparison

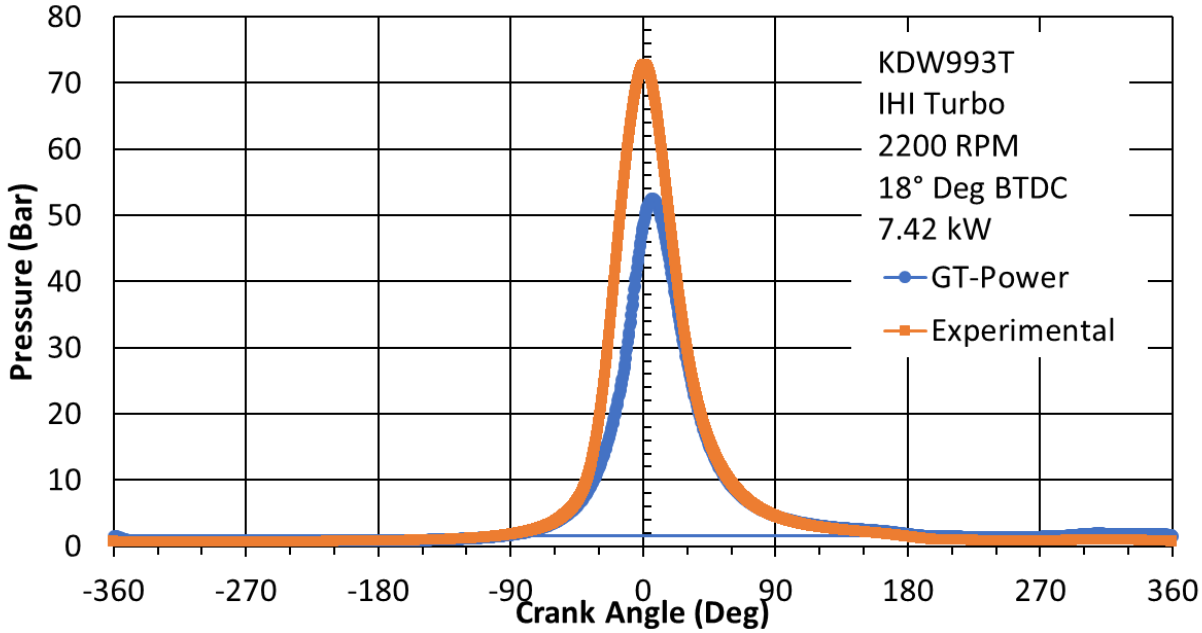

Figure 94: 2200 RPM and 18°BTDC Timing Pressure Curve Comparison

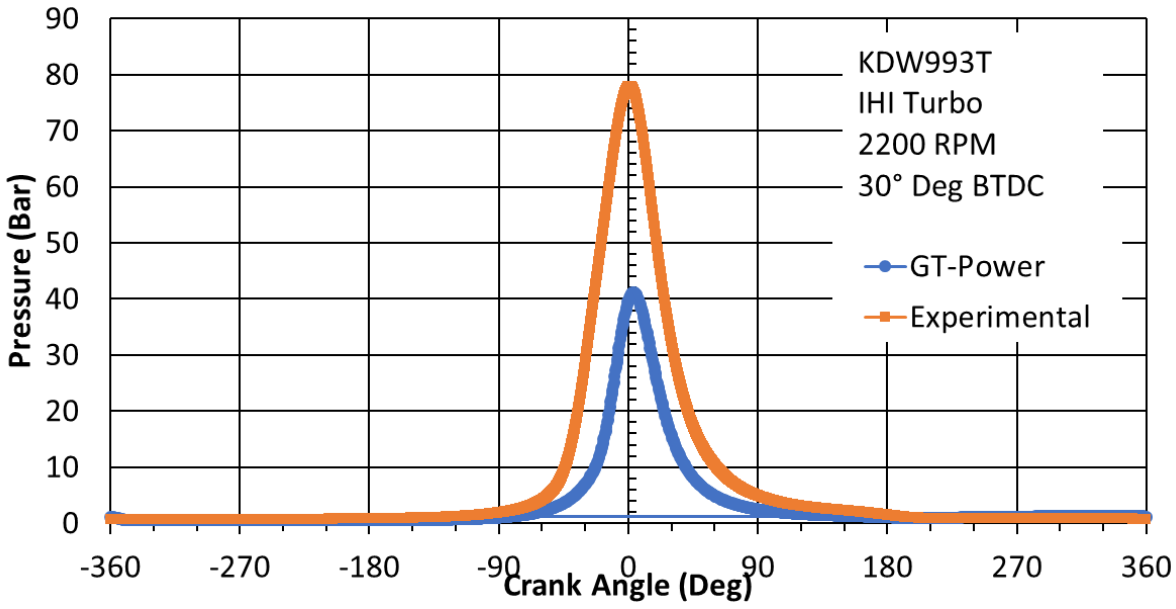

Figure 95: 2200 RPM and 30°BTDC Timing Pressure Curve Comparison

5.4 TURBOCHARGER PERFORMANCE

During modeling, the throttle controller was actuating the throttle valve to match the experimental intake pressure rather than the wastegate, meaning that GT-Power is overpredicting the performance of the turbocharger. The cause of this overprediction is the turbine. The GT-Power model predicts higher exhaust pressures than were achieved in experimental testing. The higher PR caused by these higher exhaust manifold pressures causes the turbine to produce more power, causing the compressor to produce more boost.

5.4.1 INTAKE MANIFOLD CONDITIONS

Figure 96 shows the intake manifold pressure for each condition. There is a good match at low engine speeds, but there is a significant mismatch at 2200 RPM. This mismatch is due to the deviation in the brake efficiency prediction discussed in Section 5.1. The GT-Power model over predicts efficiency at these speeds; thus, the engine requires less mass flow rate for the same brake power. The lowered mass flow rate at a constant volumetric flow rate causes a reduction in

intake manifold pressure for the GT-Power model. Small discrepancies in pressure may also be due to the reduction in density caused by the increase in temperature later. The best intake manifold pressure match was found at 1600 RPM and 16° timing with a percent difference of 1.89% and an absolute difference of 0.02 Bar.

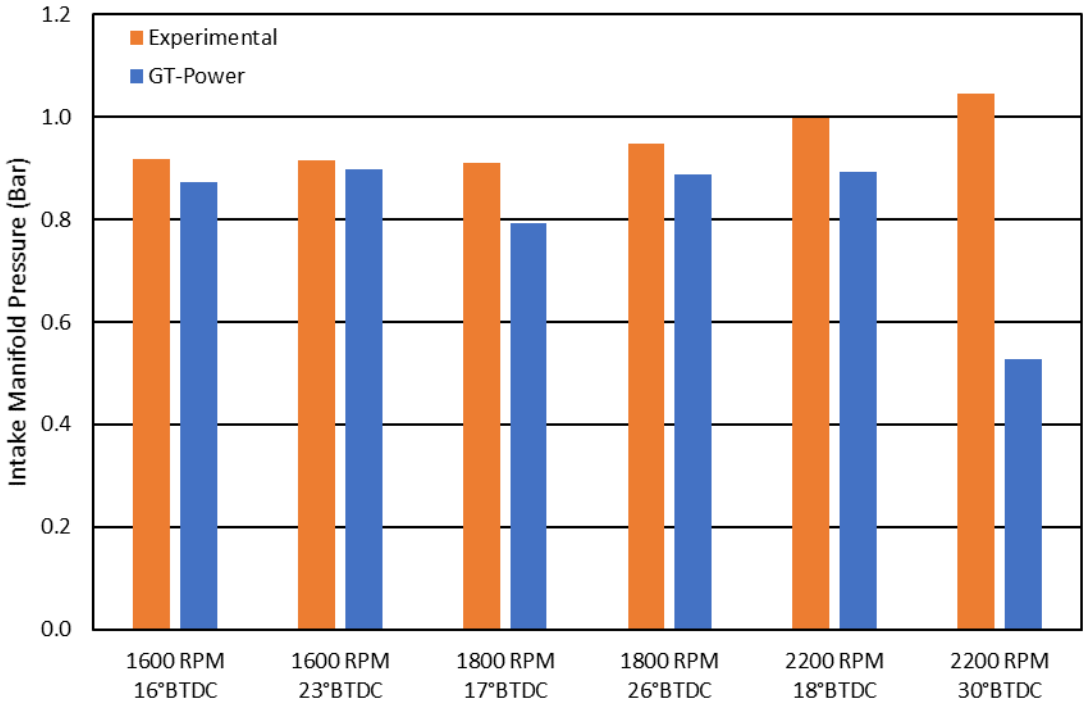

Figure 96: Intake Manifold Pressure Comparison

Figure 97 shows the intake manifold temperature for both the experimental and model. The temperature is more variable in comparison, this is due to both compressors operating at different power levels, and the intercooler playing a part in both the experimental and GT-Power comparison. Overall the temperature match was good with the low engine speeds matching well. The best match was found at 1800RPM and 17° timing, with a percent difference of 0.91%, and an absolute difference of 0.4°C. The deviations in brake efficiencies cause different mass flow

rates through the compressor and intercooler, causing temperature deviations in the model. This deviation is evident at 2200 RPM and 30° timing.

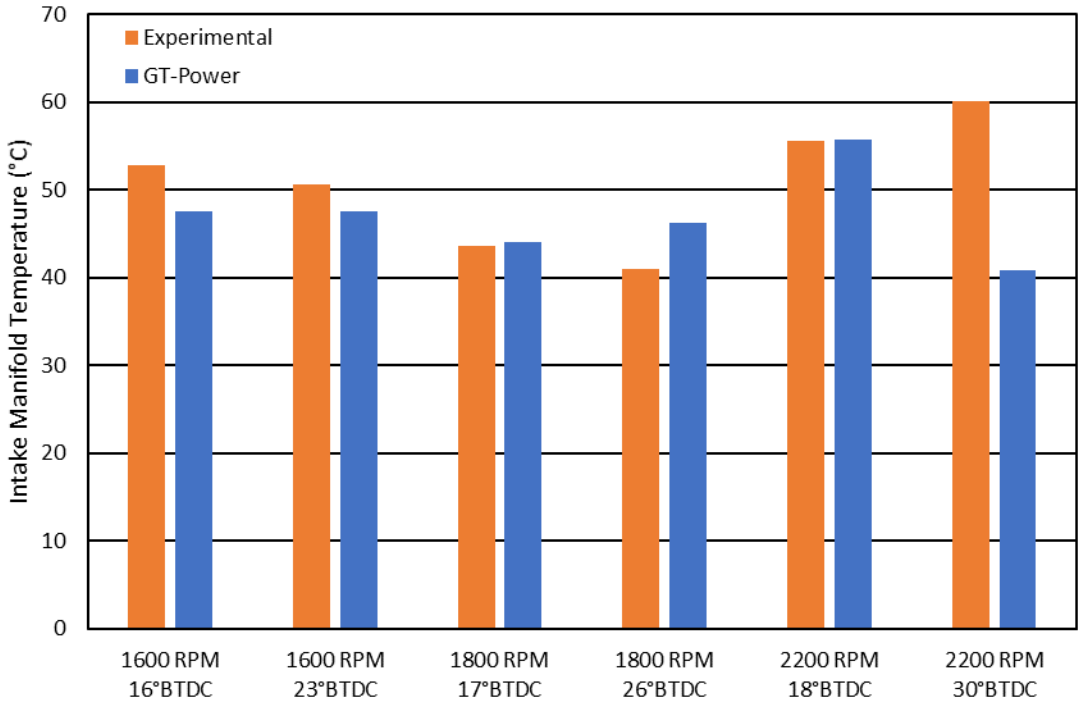

Figure 97: Intake Manifold Temperature Comparison

5.4.2: EXHAUST MANIFOLD CONDITIONS

The deviations in exhaust conditions are quite extreme compared to every other parameter. GT-Power exhaust pressure is consistently higher than experimental data. For the modeling done here, the wastegate is held closed to provide an accurate match. Figure 98 shows the exhaust pressure for the experimental and model at all test points. At every point, GT-Power predicted a higher exhaust manifold pressure. No point came within a 10% error except for 2200 RPM and 30° timing. Though this result is not trustworthy due to the major deviations in every other critical metric at this point. The best match was found at 1800 RPM and 17° timing, with a percent difference of 13.22%, and an absolute difference of 0.14 Bar. The deviations in exhaust

pressure may be due to the GT-Power model not fully capturing pressures losses. Refinement of the GEM3D exhaust model would probably solve this problem.

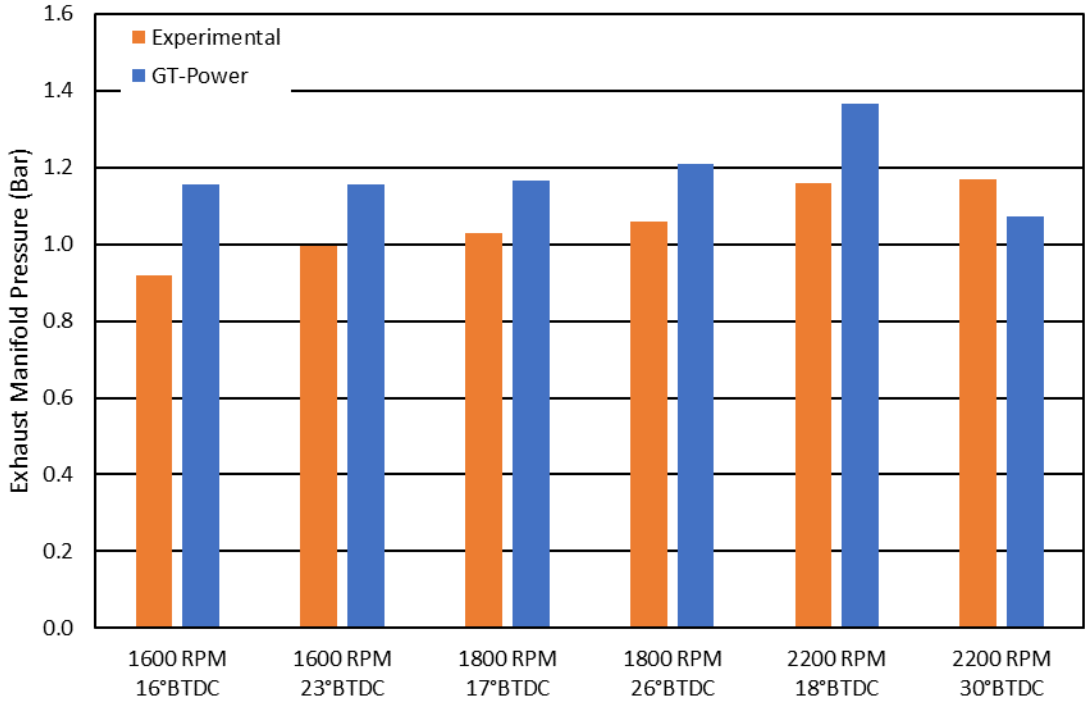

Figure 98: Exhaust Manifold Pressure Comparison

Figure 99 shows the exhaust manifold gas temperature for the model/experimental at every condition tested. The GT-Power Model exhaust gas is consistently hotter than the experimental data. The model being hotter is mostly true for the retard timings, but there is an unusal spike at 1800 RPM and 26° timing. This point is the highest brake load point; the high load could cause the high exhaust gas temperature predictions. The point with the closest match is 2200 RPM and 30° timing, but due to other factors already discussed, this point is an outlier. The closest valid point match is found at 1800 RPM and 17° timing, with a percent difference of 6%, and an absolute difference of 30°C.

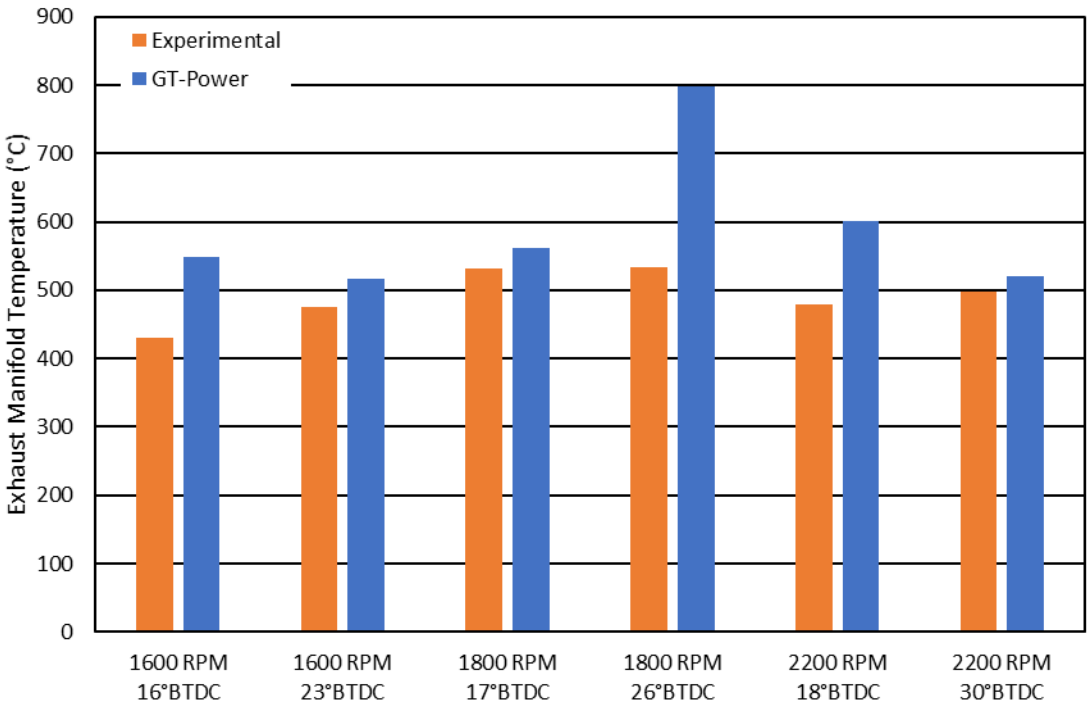

Figure 99: Exhaust Manifold Temperature Comparison

CHAPTER 6: CONCLUSIONS AND FUTURE WORK

The overall goal of this work was to develop a spark-ignited anode tailgas engine. A model of a Kohler 993T 0.993L diesel engine, was developed and validated within 1% of experimental. The resulting model was converted to anode tailgas fuel spark ignition, and vary engine parameters to optimize brake efficiency while operating on anode tailgas. The identified parameters were used to guide the construction of a physical prototype engine. The physical engine was installed at CSU and run at spark timings determined by the GT-Power model to be the most efficient, and where knock initiation occurs. The model was then rerun using the experimental data as the initial conditions. The model and experimental data were then compared to evaluate the predictive capability of the model.

The major findings of this research were as follows:

1) Anode tailgas operation of the model is possible on the KDW993T platform; however the dilute nature of the fuel causes a substantial drop in power output.
2) Changes in the IVC angle has no positive effect on the brake efficiency of the model; stock valve timing provided the maximum brake efficiency on ATG. The delayed IVC timings cause high pumping losses, which are greater than the power gained from overexpanding the cycle.
3) The compression ratio has a significant effect on the brake efficiency of the model. While the model could be operated on the stock compression ratio of 21:1, it was not the highest brake efficiency and had a small margin of controllability between MBET and knock initiation. Maximum brake efficiency of 31.25% occurs at a compression ratio of 17:1; this is most likely due to the lower surface to volume ratio, preventing heat transfer losses in-cylinder.

4) The stock turbocharger for the KDW993T does not provide the intake manifold pressures required for full power operation on ATG fuel. A new turbocharger from IHI was selected for the high PR it can provide at low flow rates.
5) A maximum brake efficiency of 27.37% on the prototype engine occurred at 1600 RPM and 16° BTDC timing and a brake power of 5.77kW.
6) A maximum brake power of 7.42 kW on the prototype engine occurred at 2200 RPM and 18° BTDC timing.
7) The spark timing has no significant effect on the location of maximum cylinder pressure or heat release rate while operating on ATG fuel. This insensitivity is most likely due to pre-ignition caused by the spark plug. The platinum spark plug acts as a catalyst for the hydrogen in the fuel, drastically lowering ignition energy and allowing the hot tip of the plug to ignite the fuel without spark. The location of the spark plug directly adjacent to the intake valve provides an optimal position for the flame to propagate back through the intake manifold, causing backfires.
8) The GT-Power model matched the critical metrics well at low engine speeds and advanced ignition timings. The best model match occurred at 1600 RPM and 23° BTDC timing.
9) GT-Power over predicted the performance of the turbocharger due to higher exhaust pressures occurring in the model, causing a higher PR across the turbine and increasing shaft power available to the compressor.
10) GT-Power combustion modeling does not accurately capture the ATG fuel combustion process occurring in the prototype engine due to autoignition happening. This abnormal combustion caused significant deviations in critical modeling metrics

beyond a 10% difference, most notably in the maximum cylinder pressure magnitude and location. The effect of combustion modeling difference is most visible at higher engine speeds and retarded ignition timings.

11) The model matching well at low engine speeds and advanced timings indicates that the results obtained for 14 kW load at 1600 and 1800 RPM are most likely valid, and a brake efficiency greater than 30% can be achieved on the existing prototype.

6.1 FUTURE WORK

Future work on the prototype at CSU should focus on eliminating backfires and identifying the definite cause of pre-ignition. The engine should then be run to the full power of 14 kW to validate the model at the original operating points. Physical modifications to the engine should also be investigated, including a different turbocharger, optimized piston bowls, and different cam timings that have IVC occur BBDC. Pumping losses would still be present with IVC BBDC but should be less than the pumping losses caused by pumping back against the full manifold pressure, which is present in delated IVC ABDC. Future work on the GT-Power model should focus on identifying the cause of excess pressure and temperature in the exhaust. A review of the GEM3D exhaust manifold model is necessary to ensure that pressure losses are modeled correctly.

Future work on ATG fuel engines should focus on lean operation. During the testing operation on an extremely lean mixture ($\Phi<0.65$) was possible. The dilute nature of the fuel and cooler combustion temperatures may reduce NO_x emissions to acceptable levels at these equivalence ratios compared to traditional fuels. Allowing for an increase in brake efficiency without dramatically increased emissions. Another area of interest is the use of port fuel injection rather than a single point venturi mixer. Port injection would reduce mixture variability between

cylinders allowing for more advanced control schemes. PFI would also enable a turbocharger only to compress air rather than an air/fuel mix, possibly allowing higher turbocharger performance. The high flow rates required by the low AFR of ATG pose a challenge when selecting injectors and ensuring proper mixing of the high quantity of gas before entering the cylinder. A possible way around this is to inject the air with injectors and use the main induction system for fuel. Preventing condensation of water in the fuel in the injection system.

REFERENCES

[1] General Electric Power 2020, Advanced Ultra-Supercritical Technology, General Electric, viewed March 2020 <https://www.ge.com/power/steam/steam-power-plants/advanced-ultra-supercritical-usc-ausc>

[2] Science Direct 2020, Diesel Generators, Science Direct, viewed March 2020, <https://www.sciencedirect.com/topics/engineering/diesel-generator>

[3] Fuel Cell Today 2020, Solid Oxide Fuel Cells, Fuel Cell Today, viewed March 2020 <http://www.fuelcelltoday.com/technologies/sofc>

[4] Braun, R., Reznicek, E., Cadigan, C., Sullivan, N.P., Danforth R., Bandhauer, T., Garland, S., Olsen, D., Windom, B., Schaffer, B., *Development of a Novel High Efficiency, Low Cost Hybrid SOFC/Internal Combustion Engine Power Generator*

[5] Devine. *Biogas comes of age*. Technical report, Caterpillar Inc, 501 SW Jefferson Ave. Peroria, IL 61630, February 2013

[6] Centers for Disease Control 2001, Landfill Gas Primer, Agency for Toxic Substances & Disease Registr, viewed March 2020 <https://www.atsdr.cdc.gov/HAC/landfill/html/ch2.html>

[7] Environmental Protection Agency 2009, Understanding Global Warming Potentials, Environmental Protection Agency, viewed March 2020 <https://www.epa.gov/ghgemissions/understanding-global-warming-potentials>

[8] Environmental Protection Agency 2009, Basic Information about Landfill Gas, Environmental Protection Agency, viewed March 2020, <https://www.epa.gov/lmop/basic-information-about-landfill-gas>

[9] Food and Agriculture Organization of the United Nations, *Wood Gas as an Engine Fuel*, United Nations, Rome Italy, 1986

[10] Gupta S., Mittal. M, *Effect of Biogas Composition Variations on Engine Characteristics Including operational Limits of a Spark-Ignition Engine,* Journal of Engineering for Gas Turbines and Power vol 141, ASME, October 2019

[11] Papagiannakis, R.G., Zannis, T.C., *Thermodyamic Analysis of Combustion and Pollutants Formation in a Wood-Gas Spark-Ignitited Heavy-Duty Engine,* International Journal of Hydrogen Energy vol 38, Science Direct, 2013

[12] Taylor, C. *The Internal Combustion Engine in Theory and Practice Revised Edition Vol. 2,* MIT Press, Cambridge MA, 1985

[13] Kirkpatrick, A., Ferguson, C., *Internal Combustion Engines Applied Thermosciences 3rd Edition,* Wiley, Chichester UK, 2016

[14] Taylor, C. *The Internal Combustion Engine in Theory and Practice Revised Edition Vol. 1,* MIT Press, Cambridge MA, 1985

[15] Padhi, G. *Modelling and Simulation of Combustion of Dilute Syngas Fuels in a CFR Engine,* Colorado State University, October 2019

[16] Sandoval, D., Heywood, J., *An Improved Friction Model for Spark Ignition Engines,* SAE International, SAE, 2003

[17] Woschni, G., *A Universally Applicable Equation for the Instantaneous Heat Transfer Coefficient in the Internal Combustion Engine,* SAE International, SAE, 1967

[18] Balu, A. *Analysis of Simulated Dilute Anode Tail-Gas Combustion Characteristics on a CFR Engine,* Colorado State University, May 2020

[19] Chitragar, P., Shivaprasad K., Kumar, G., *Use of Hydrogen in Internal Combustion Engines: A Comprehensive Study,* Journal of Mechanical Engineering and Biomechanics, 2016

[20] Engineering Toolbox, Thermal Conductivity of Metals, Meallic Elements, and Alloys, viewed April 2020 <https://www.engineeringtoolbox.com/thermal-conductivity-metals-d_858.html>

[21] Environmental Protection Agency 2020, Compliance Requirements for Sationary Engines, Environmental Protection Agency, viewed May 2020 <https://www.epa.gov/stationary-engines/compliance-requirements-stationary-engines#Compliance%20Requirements>

[22] Guan, C., Theotokatos, G., Chen, H., *Analysis of Two Stroke Marine Diesel Engine Operation Including Turbocharger Cut-Out by Using a Zero-Dimensional Model*, Energies, 2015

[23] Burke, U., et al., *An ignition delay and kinetic modeling study of methane,dimethyl ether, and their mixtures at high pressures,* Elsevier ScienceDirect, 2014

APPENDIX A – RAW EXPERIMENTAL DATA

	RPM	Ignition Timing	
		16	23
IMEP [Bar]	1600	3.971	3.923
IMEP COV	1600	5.099	5.355
Brake Efficiency [%]	1600	27.340	26.980
Torque [N*m]	1600	34.430	33.990
Power [kW]	1600	5.770	5.700
CO [ppmd]	1600	6046	4572
Average Pressure [Bar]	1600	59.904	60.366
Average Pressure COV [%]	1600	0.846	0.804
Peak Locaiton [°ATDC]	1600	0.911	0.932
Max Peak [Bar]	1600	60.913	61.205
Min Peak [Bar]	1600	57.841	58.748
Fuel Flow [g/s]	1600	5.616	5.626
BSFC [g/kWh]	1600	3614	3663
CO2 [%]	1600	35.599	35.447
O2 [%]	1600	0.412	0.471
MAP [Bar]	1600	0.918	0.915
Compressor PR	1600	1.080	1.076
IAT [°C]	1600	52.800	50.700
Exhaust Manifold Pressure [Bar]	1600	1.023	0.995
Turbine PR	1600	1.245	1.213
Exhaust Manifold Temp [°C]	1600	382.200	396.700
Exhaust Port Temp [°C]	1600	429.800	475.000
BSTHC [g/kWh]	1600	0.530	0.560
BSCO [g/kWh]	1600	45.560	65.100
BSNOx [g/kWh]	1600	6.880	6.830
BMEP [Bar]	1600	4.358	430.514
PP Std Dev	1600	0.507	0.485
Peak Loc Std Dev	1600	0.361	0.361
Peak Loc COV [%]	1600	39.864	39.551

	RPM	Ignition Timing	
		17	26
IMEP [Bar]	1800	3.923	3.956
IMEP COV	1800	5.053	4.484
Brake Efficiency [%]	1800	23.310	23.860
Torque [N*m]	1800	29.960	32.300
Power [kW]	1800	5.650	6.090
CO [ppmd]	1800	5828	4228
Average Pressure [Bar]	1800	60.602	61.311
Average Pressure COV [%]	1800	0.979	0.665
Peak Locaiton [°ATDC]	1800	0.891	1.016
Max Peak [Bar]	1800	61.601	62.048
Min Peak [Bar]	1800	58.843	59.857
Fuel Flow [g/s]	1800	6.374	6.362
BSFC [g/kWh]	1800	4168	3864
CO2 [%]	1800	33.468	36.234
O2 [%]	1800	1.846	0.005
MAP [Bar]	1800	0.911	0.947
Compressor PR	1800	1.072	1.114
IAT [°C]	1800	43.600	41.000
Exhaust Manifold Pressure [Bar]	1800	1.031	1.064
Turbine PR	1800	1.248	1.294
Exhaust Manifold Temp [°C]	1800	369.900	440.900
Exhaust Port Temp [°C]	1800	531.300	533.900
BSTHC [g/kWh]	1800	0.670	0.390
BSCO [g/kWh]	1800	51.690	41.360
BSNOx [g/kWh]	1800	11.000	8.700
BMEP [Bar]	1800	379.322	408.862
PP Std Dev	1800	0.594	0.408
Peak Loc Std Dev	1800	0.351	0.321
Peak Loc COV [%]	1800	40.822	32.045

	RPM	Ignition Timing	
		18	30
IMEP [Bar]	2200	4.749	4.224
IMEP COV	2200	4.509	5.004
Brake Efficiency [%]	2200	23.730	8.860
Torque [N*m]	2200	32.210	13.150
Power [kW]	2200	7.420	3.031
CO [ppmd]	2200		
Average Pressure [Bar]	2200	68.799	73.885
Average Pressure COV [%]	2200	0.964	0.481
Peak Locaiton [°ATDC]	2200	0.971	1.212
Max Peak [Bar]	2200	69.727	74.687
Min Peak [Bar]	2200	65.916	72.851
Fuel Flow [g/s]	2200	8.072	8.538
BSFC [g/kWh]	2200	3985	10476
CO2 [%]	2200		
O2 [%]	2200		
MAP [Bar]	2200	0.998	1.045
Compressor PR	2200	1.174	1.229
IAT [°C]	2200	55.600	60.200
Exhaust Manifold Pressure [Bar]	2200	1.158	1.173
Turbine PR	2200	1.395	1.415
Exhaust Manifold Temp [°C]	2200	431.600	473.100
Exhaust Port Temp [°C]	2200	479.800	497.500
BSTHC [g/kWh]	2200		
BSCO [g/kWh]	2200		
BSNOx [g/kWh]	2200		
BMEP [Bar]	2200		
PP Std Dev	2200	0.660	0.355
Peak Loc Std Dev	2200	0.367	0.325
Peak Loc COV [%]	2200	29.034	26.784

APPENDIX B - RAW GT-POWER EXPERIMENTAL COMPARRISON

	GT-Power	Experimental	Percent Difference	Absolute Difference
Engine Speed (cycle average)	1600	1600	0	0
Combustion Start (°BTDC)	16	16	0	0
Brake Torque (N*m)	34.4	34.4	0.05	0.02
Brake Power (kW)	5.76	5.77	0.08	0.00
Brake Efficiency, System (%)	27.8	27.3	-1.67	0.46
Average of Maximum Cylinder Pressures (Bar)	49.1	61.1	19.7	12.0
Maximum Pressure (Bar)	50.2	62.2	19.2	12.0
Crank Angle at Maximum Pressure (CAD ATDC)	6.68	0.92	-622	5.75
Average Pressure Inlet (Bar)	0.87	0.92	4.87	0.04
Average Temperature Inlet (°C)	47.6	52.8	9.88	5.22
Average Pressure Exhaust (Bar)	1.15	0.92	-25.8	0.24
Average Temperature Exhaust (°C)	550	430	-27.9	120

	GT-Power	Experimental	Percent Difference	Absolute Difference
Engine Speed (cycle average)	1800	1801	0	1
Combustion Start (°ATDC)	-17	-17	0	0
Brake Torque (N*m)	30.1	30.0	-0.37	0.11
Brake Power (kW)	5.67	5.65	-0.33	0.02
Brake Efficiency, System (%)	26.7	23.3	-14.48	3.38
Average of Maximum Cylinder Pressures (Bar)	45.6	61.2	25.5	15.6
Maximum Pressure (Bar)	46.7	62.5	25.3	15.8
Crank Angle at Maximum Pressure (CAD ATDC)	6.76	0.94	-618	5.82
Average Pressure Inlet (Bar)	0.79	0.91	12.86	0.12
Average Temperature Inlet (°C)	44.0	43.6	-0.91	0.40
Average Pressure Exhaust (Bar)	1.17	0.83	-41.14	0.34
Average Temperature Exhaust (°C)	561	531	-5.6	30

	GT-Power	Experimental	Percent Difference	Absolute Difference
Engine Speed (cycle average)	2200	2201	0	1
Combustion Start (°ATDC)	-18	-18	0	0
Brake Torque (N*m)	32.2	32.2	0.02	0.01
Brake Power (kW)	7.42	7.42	0.05	0.00
Brake Efficiency, System (%)	26.1	23.7	-10.16	2.41
Average of Maximum Cylinder Pressures (Bar)	51.0	70.1	27.26	19.10
Maximum Pressure (Bar)	52.5	71.2	26.23	18.66
Crank Angle at Maximum Pressure (CAD ATDC)	6.16	1.17	-426	4.99
Average Pressure Inlet (Bar)	0.89	1.00	10.65	0.11
Average Temperature Inlet (°C)	55.7	55.6	-0.18	0.10
Average Pressure Exhaust (Bar)	1.37	0.83	-64.45	0.54
Average Temperature Exhaust (°C)	601	480	-25.3	122

	GT-Power	Experimental	Percent Difference	Absolute Difference
Engine Speed (cycle average)	1600	1600	0	0
Combustion Start (°BTDC)	23	23	0	0
Brake Torque (N*m)	34.1	34.0	-0.19	0.07
Brake Power (kW)	5.71	5.70	-0.19	0.01
Brake Efficiency, System (%)	26.7	27.0	1.02	0.28
Average of Maximum Cylinder Pressures (Bar)	58.9	61.6	4.45	2.74
Maximum Pressure (Bar)	60.1	62.4	3.67	2.29
Crank Angle at Maximum Pressure (CAD ATDC)	5.32	1.05	-409	4.28
Average Pressure Inlet (Bar)	0.90	0.92	1.89	0.02
Average Temperature Inlet (°C)	47.5	50.7	6.16	3.12
Average Pressure Exhaust (Bar)	1.16	0.99	-16.20	0.16
Average Temperature Exhaust (°C)	517	475	-8.90	42

	GT-Power	Experimental	Percent Difference	Absolute Difference
Engine Speed (cycle average)	1800	1800	0	0
Combustion Start (°ATDC)	-26	-26	0	0
Brake Torque (N*m)	32.4	32.3	-0.32	0.10
Brake Power (kW)	6.11	6.09	-0.30	0.02
Brake Efficiency, System (%)	25.8	25.5	-1.0	0.26
Average of Maximum Cylinder Pressures (Bar)	61.5	61.7	0.2	0.1
Maximum Pressure (Bar)	62.9	62.6	-0.5	0.3
Crank Angle at Maximum Pressure (CAD ATDC)	4.78	1.02	-371	3.76
Average Pressure Inlet (Bar)	0.89	0.95	6.33	0.06
Average Temperature Inlet (°C)	46.2	41.0	-12.65	5.19
Average Pressure Exhaust (Bar)	1.21	0.82	-47.26	0.39
Average Temperature Exhaust (°C)	799	534	-49.7	265

	GT-Power	Experimental	Percent Difference	Absolute Difference
Engine Speed (cycle average)	2200	2200	0	0
Combustion Start (°ATDC)	-30	-30	0	0
Brake Torque (N*m)	13.0	13.2	1.33	0.17
Brake Power (kW)	2.99	3.03	1.35	0.04
Brake Efficiency, System (%)	17.4	8.86	-96.17	8.52
Average of Maximum Cylinder Pressures (Bar)	39.9	75.1	46.90	35.24
Maximum Pressure (Bar)	41.1	75.8	45.80	34.74
Crank Angle at Maximum Pressure (CAD ATDC)	3.75	1.14	-229	2.61
Average Pressure Inlet (Bar)	0.53	1.04	49.52	0.52
Average Temperature Inlet (°C)	40.8	60.2	32.15	19.35
Average Pressure Exhaust (Bar)	1.07	0.83	-29.38	0.24
Average Temperature Exhaust (°C)	520	497	-4.6	23